

AD-A267 688 ENTATION PAGE

Form Approved
OMB No. 0704-0188

mailing to: (a) the user response including the time for review and instructions; searching existing data sources; reviewing the collection of information; Send comments regarding this burden estimate or any other aspect of this burden to: Washington Headquarters Services, Directorate for Information Operations and Reports, 1215 Jefferson Avenue, Washington, DC 20540-6001; (b) the Office of Management and Budget, Paperwork Reduction Project (0704-0188), Washington, DC 20503

1. AGENCY USE ONLY (Leave blank)		2. REPORT DATE 1993		3. REPORT TYPE AND DATES COVERED THESIS/DISSERTATION	
4. TITLE AND SUBTITLE Study of Uranium Oxide Insertion Compunds				5. FUNDING NUMBERS	
6. AUTHOR(S) Ross E. Dueber				DTIC ELECTE AUG 11 1993	
7. PERFORMING ORGANIZATION NAME(S) AND ADDRESS(ES) AFIT Student Attending: Merton College				8. PERFORMING ORGANIZATION REPORT NUMBER AFIT/CI/CIA- 93-009D	
9. SPONSORING / MONITORING AGENCY NAME(S) AND ADDRESS(ES) DEPARTMENT OF THE AIR FORCE AFIT/CI 2950 P STREET WRIGHT-PATTERSON AFB OH 45433-7755				10. SPONSORING / MONITORING AGENCY REPORT NUMBER	
11. SUPPLEMENTARY NOTES					
12a. DISTRIBUTION / AVAILABILITY STATEMENT Approved for Public Release IAW 190-1 Distribution Unlimited MICHAEL M. BRICKER, SMSgt, USAF Chief Administration				12b. DISTRIBUTION CODE	
13. ABSTRACT (Maximum 200 words)					
93-18065 					
14. SUBJECT TERMS				15. NUMBER OF PAGES 144	
				16. PRICE CODE	
17. SECURITY CLASSIFICATION OF REPORT		18. SECURITY CLASSIFICATION OF THIS PAGE		19. SECURITY CLASSIFICATION OF ABSTRACT	
				20. LIMITATION OF ABSTRACT	

STUDY OF URANIUM OXIDE INSERTION COMPOUNDS

A Thesis Submitted for the Degree

of

Doctor of Philosophy

to

The Board of the Faculty of Physical Sciences

at

The University of Oxford

Accession For	
NTIS CRA&I	<input checked="checked" type="checkbox"/>
DTIC TAB	<input type="checkbox"/>
Unannounced	<input type="checkbox"/>
Justification	
By	
Distribution /	
Availability Codes	
Dist	Avail and/or Special
A-1	

DTIC QUALITY INSPECTED 3

Ross E. Dueber

Merton College

Hilary Term

1993

Study of Uranium Oxide Insertion Compounds

Ross E. Dueber

D.Phil. Thesis

Merton College

Hilary Term 1993

ABSTRACT

Sodium, magnesium, and zinc insertion compounds formed by α - UO_2 , U_3O_8 , γ - UO_3 , and δ - UO_3 at room-temperature were prepared. The products were characterized by powder X-ray diffraction, infrared spectroscopy, atomic absorption spectroscopy, titrimetry, and elemental analysis. These studies led to the general conclusion that although the host metal oxide structure is maintained; sodium, magnesium, and zinc insert to only a small extent.

Insertion compounds were also made by coulometric titration using non-aqueous cells of the type $\text{A(s)} | \text{A}^+(\text{sol}) | \text{UO}_n(\text{s})$. Open-circuit measurements of the cells at various x -values enabled the free energies of insertion to be calculated, which were then used in a simple model to estimate site binding energies for A. The chemical diffusion coefficients for sodium, magnesium, and zinc determined by the pulse-current method were found to be much lower than those reported for lithium.

Cyclic voltammetry in aqueous electrolyte of uranium oxides mechanically transferred to a graphite electrode enabled the reduction of these solids to be studied over a wide time domain. The results support a mechanism of a U(VI) to U(V) electron transfer coupled to cation diffusion to form a topochemical insertion compound at the solid electrode-electrolyte interface. Data are consistent with available knowledge and the work suggests that voltammetric studies on mechanically transferred solids may provide a convenient method for studying the mechanism of formation of insertion compounds.

The magnetic properties of the uranium oxides and their insertion compounds were studied in order to obtain information about their electronic structure. Magnetic susceptometry was found to be a suitable diagnostic tool for analyzing electron transfer in insertion compounds. Measurements of χ_{mol} over a wide temperature range were fitted with the Langevin-Debye relation ($\chi_{\text{mol}} = C/T + A$) and the parameters C and A used in two theoretical models based upon the U(V) crystal-field to predict electronic properties.

ACKNOWLEDGEMENTS

I would like to thank my advisor, Dr. Peter G. Dickens, for his wonderful guidance and friendship during my stay at Oxford University. I certainly will miss our Friday afternoon matches at Southfield with Lesley, Simon, and George.

I owe a large debt of gratitude to the technical and support staff of the Inorganic Chemistry Laboratory for their expertise and hard work. Were it not for them much of my work would not have been possible.

To members of the Dickens group, Dr. Saban Patat and Garry Studdard, I wish to thank you for our many meaningful discussions. And to my friend and office mate Dr. Ann Chippindale, thank you for helping me to keep it all in perspective.

I would like to thank Dr. Alan M. Bond of LaTrobe University for his help with the cyclic voltammetry experiments and the United States Air Force Academy for its sponsorship of my work these past three years.

For their love and support, I dedicate this work to my wife Sandee, my son, and my parents.

TABLE OF CONTENTS

CHAPTER 1 INTRODUCTION	1
1.1 BATTERY RESEARCH	1
1.2 INSERTION ELECTRODES	2
1.3 URANIUM-OXYGEN SYSTEM	4
1.3.1 γ - UO_3	7
1.3.2 δ - UO_3	9
1.3.3 α - U_3O_8	11
1.3.4 α - UO_{3-x}	13
1.3.5 UTiO_5	15
1.4 PURPOSE OF THIS WORK	16
 CHAPTER 2 PREPARATION AND CHARACTERIZATION OF COMPOUNDS	19
2.1 ANALYTICAL METHODS USED FOR CHARACTERIZATION	19
2.1.1 POWDER X-RAY DIFFRACTION	19
2.1.2 ATOMIC ABSORPTION SPECTROSCOPY	19
2.1.3 TITROMETRY	19
2.1.4 INFRARED SPECTROSCOPY	20
2.1.5 ELEMENTAL ANALYSIS	20
2.2 PREPARATION OF COMPOUNDS	20
2.2.1 γ - UO_3	20
2.2.2 δ - UO_3	21
2.2.3 α - UO_{3-x} and α - U_3O_8	21
2.2.4 UTiO_5	22
2.3 PREPARATION OF INSERTION COMPOUNDS	23
2.4 CHARACTERIZATION OF INSERTION COMPOUNDS	24

CHAPTER 3 ELECTROCHEMICAL CELLS	33
3.1 AMBIENT-TEMPERATURE CELLS	33
3.1.1 SODIUM AND ZINC INSERTION	33
3.1.2 MAGNESIUM INSERTION	33
3.2 ELEVATED TEMPERATURE CELL	37
 CHAPTER 4 CHRONOPOTENTIOMETRIC STUDY OF CATION INSERTION	42
4.1 THEORY	42
4.1.1 THERMODYNAMIC STUDIES	42
4.1.2 KINETIC STUDIES	43
4.1.2.1 Kinetic Properties of Solids	43
4.1.2.2 Electrochemical Techniques for Determining Kinetic Properties of Solids	46
4.2 APPARATUS	47
4.3 GALVANOMETRIC MEASUREMENTS	48
4.3.1 AMBIENT-TEMPERATURE INSERTION	48
4.3.1.1 Sodium	48
4.3.1.2 Magnesium	51
4.3.1.3 Zinc	52
4.3.2 ELEVATED TEMPERATURE	56
4.4 THERMODYNAMIC MEASUREMENTS	56
4.5 KINETIC MEASUREMENTS	63
 CHAPTER 5 CYCLIC VOLTAMMETRIC STUDY OF CATION INSERTION	70
5.1 THEORY	70
5.1.1 CLASSICAL SOLUTION VOLTAMMETRY	70
5.1.2 SOLID-STATE VOLTAMMETRY	73
5.2 CYCLIC VOLTAMMETRY OF INSERTION COMPOUNDS	74
5.3 DESCRIPTION OF TEST SET-UP	75
5.4 VOLTAMMETRY OF U_3O_8	76

5.4.1 SHORT TIME DOMAIN EXPERIMENTS IN ELECTROLYTE CONTAINING Mg^{2+} . . .	76
5.4.2 LONG TIME DOMAIN EXPERIMENTS IN ELECTROLYTE CONTAINING Mg^{2+} . . .	82
5.4.3 SHORT TIME DOMAIN EXPERIMENTS WITH MIXED CATION ELECTROLYTES . . .	84
5.5 VOLTAMMETRY OF $UO_{2.90}$, $\delta-UO_3$, and $\gamma-UO_3$	87
5.5.1 SHORT TIME DOMAIN EXPERIMENTS IN ELECTROLYTE CONTAINING Mg^{2+} . . .	87
5.5.2 LONG TIME DOMAIN EXPERIMENTS IN ELECTROLYTE CONTAINING Mg^{2+} . . .	89
5.6 DISCUSSION	89
 CHAPTER 6 MAGNETIC PROPERTIES	 96
6.1 MACROSCOPIC QUANTITIES	96
6.2 MEASUREMENT OF MAGNETIZATION	97
6.2.1 PRINCIPLES OF OPERATION - SQUID	97
6.2.2 THE SQUID SUSCEPTOMETER	99
6.2.3 EXPERIMENTAL	101
6.3 THEORETICAL BACKGROUND AND MODEL SYSTEMS	101
6.3.1 MAGNETICALLY DILUTE SYSTEM	102
6.3.1.1 $D_{\infty h}$ ($UO_{2.9}$ and U_3O_8)	103
6.3.1.2 O_h ($\delta-Li_xUO_3$)	107
6.3.2 MAGNETICALLY CONCENTRATED SYSTEMS - EXCHANGE COUPLING	109
6.4 RESULTS	111
6.5 DISCUSSION	123
 CHAPTER 7 CONCLUSIONS	 129
 APPENDIX	 131

CHAPTER 1 INTRODUCTION

1.1 BATTERY RESEARCH

Electrochemical energy systems have numerous applications in both the commercial and military sectors of society. They have permeated our lifestyles to the point where we can no longer function without them. Batteries can be found inside the human body (pacemakers), in the depths of the oceans (submarines), at the edge of the solar system (Voyager), and under the hood of a car to name just a few examples of their applications. Electrical power without the need for fossil fuels, falling water, fission or fusion is what batteries represent. Power available at the flip of a switch for the portable society of today.

Given the vital role batteries play, one can appreciate the importance of research into understanding and improving them. Unfortunately, the trend by manufacturers has been not to seek an in-depth understanding of the chemical behavior of these systems. Rather they have focused upon engineering solutions to problems of a fundamental chemical nature. Their approach has been quite successful, but the lack of a fundamental understanding of the chemistry has made improvements in the technology slow and difficult. It is a goal of this research project to provide some of this necessary, fundamental understanding.

The direction of battery technology over the years has been towards the development of higher energy density couples possessing longer lifetimes. Manufacturers of systems utilizing batteries have demanded greater energy capacity for longer periods of time in smaller packages. A primary example of this is the spacecraft industry where batteries are used as energy storage devices. Early satellites required power outputs of less than 100 watts. Compare this value with the 1 to 2 kilowatts for current satellites and the 10 to 100 kilowatts for future satellites and one begins to understand the magnitude of the power output hurdle. This increased power requirement is coupled to minimal increases in battery weight which can currently comprise 10 - 15% of the satellite's total weight. This number could easily grow to 50% at the higher power levels. And to complicate matters, battery lifetime must be extended to prolong the useful life of spacecraft costing upwards of \$1 billion! The task facing battery scientists and engineers is truly formidable.

1.2 INSERTION ELECTRODES

Batteries can be divided into classes along a number of lines with chemical reversibility being the most common. Primary batteries, like Zn-MnO₂, Zn-HgO, and Li-SO₂ undergo a single discharge and are disposable. The chemical reactions occurring in these batteries are irreversible, making regeneration of the initial reactants impossible. Secondary batteries differ from primaries in that they are capable of being recharged to nearly 100% of their initial capacity. This charge-discharge process, referred to as cycling, can be carried out in the range of tens to thousands of cycles depending upon the system (1). Some common batteries in this category include Pb-PbO₂, Ni-Cd, and Ag-Zn.

Batteries can also be categorized by the types of chemical reactions that occur at the cathode (2). In the reaction in equation 1.1, the crystalline structure of copper (II) chloride is irreversibly altered during cell discharge to form two new compounds.



Topochemical insertion reactions, on the other hand, result in the product possessing a close structural resemblance to its parent (3). A molecule or ion can enter the structure of the host material with little distortion of the crystal lattice. The general reaction for insertion of a mobile guest species (A) into a crystalline host lattice (Host) is



A number of transition-metal sulfides and oxides, in which the metal occurs in a high oxidation state, have open covalent structures and are capable of incorporating alkali and other electropositive metals under mild conditions. In 1959 Rudorff and Sick (4,5) first reported the formation of intercalation compounds between alkali-metals and layered metal dichalcogenides. Early work focused upon TiS₂ which has the characteristic arrangement of the transition-metal atoms sandwiched between two hexagonal close-packed chalcogen layers. Available sites for guest atoms are of the same symmetry as those of the host transition metal - octahedral or tetrahedral. Titanium disulfide has served as an excellent test vehicle, but it has been superseded by compounds with higher energy densities and flatter discharge profiles (6). Gabano (7) has surveyed the technology and summarized the

primary candidates for a high energy rechargeable battery utilizing lithium as the anode.

Transition-metal oxides, like V_2O_5 , are at the top of the list.

Transition-metal oxides were initially thought to undergo oxygen abstraction, yielding lithium oxide and reducing the oxidation state of the metal, as in the following two examples (2):



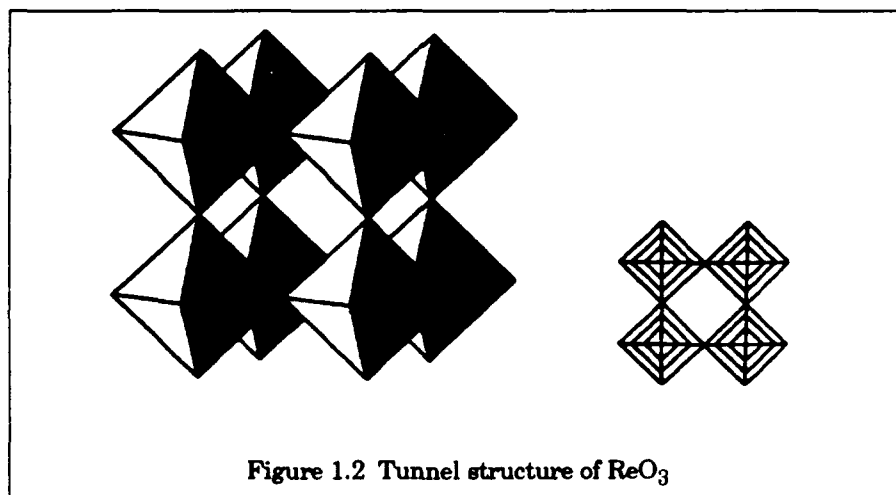
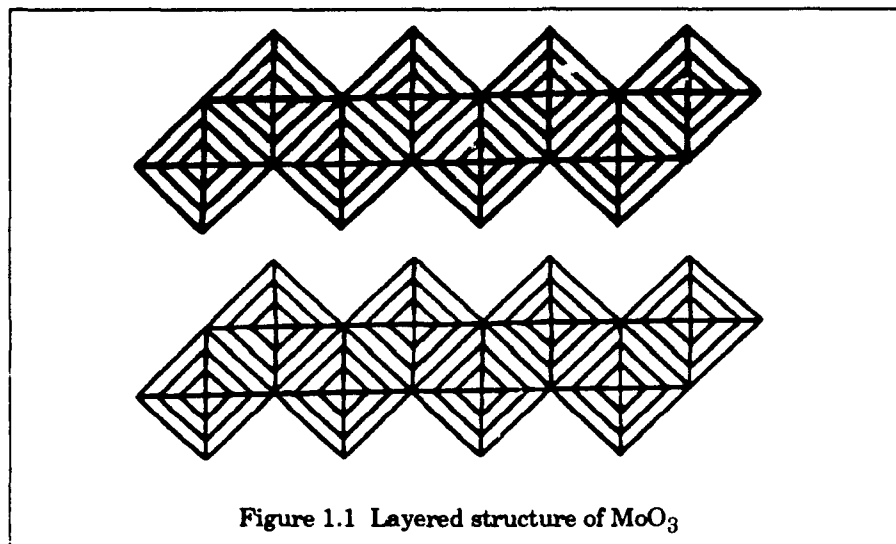
Measured potentials, however, are 3.5 V and 2.8 V respectively for these two cells. Once it was recognized that many transition-metal oxides had layers between which intercalation could occur (8), then the idea of ternary-phase formation by topochemical reaction became plausible. Now it is accepted that the reactions which occur in the previous examples are



where x -values refer to a single phase of variable composition or to two-phase mixtures of fixed composition (9).

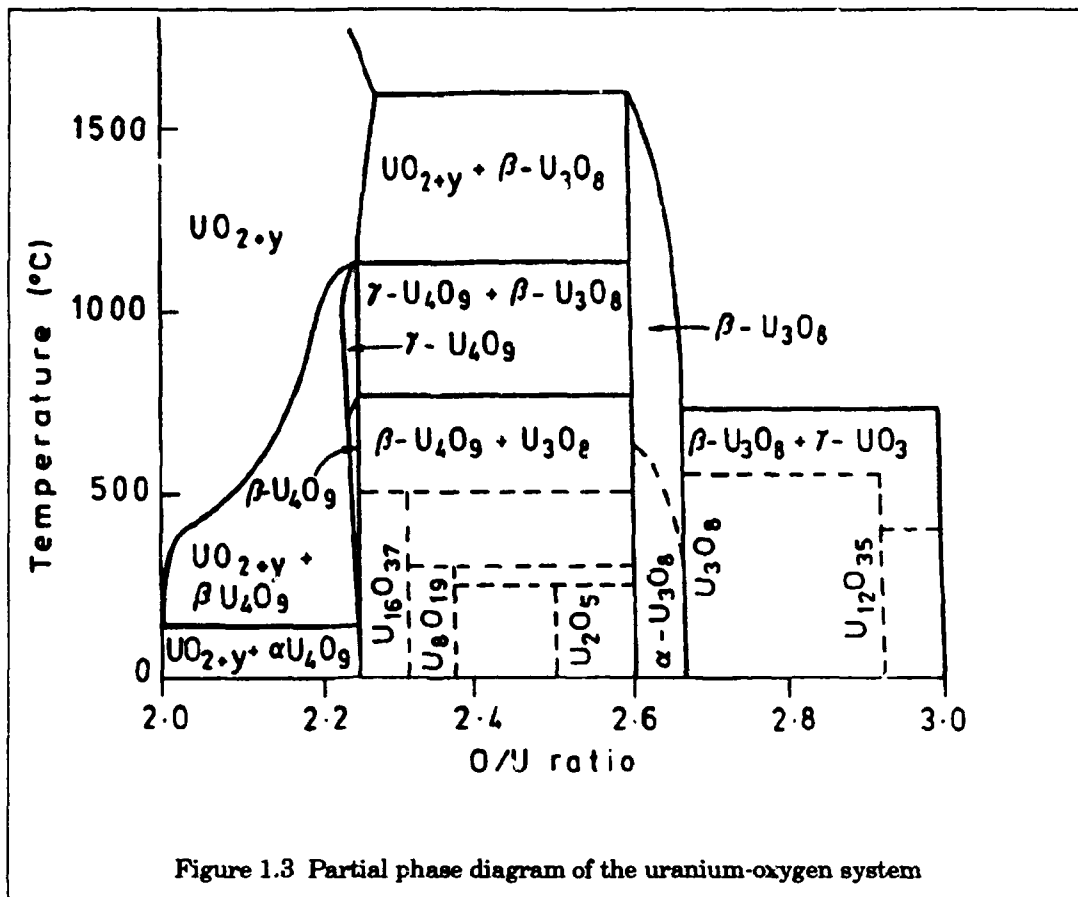
The metal oxides examined in this project fall into two broad categories: those with a two-dimensional layered structure and those with the three-dimensional tunnel network (10). A good example of a pure layered structure is MoO_3 , shown in Figure 1.1. The layers consist of vertex sharing chains of MoO_6 octahedra sharing two adjacent edges. Layers are stacked in a staggered arrangement and are bonded to one another through weak van der Waals forces. These weak forces give the structure great flexibility in accommodating even large polyatomic ions like cobaltocene.

In contrast to the flexible layered structure is the rigid tunnel network represented in Figure 1.2 by ReO_3 . Vertex sharing chains of ReO_6 octahedra are linked at their corners to form a three-dimensional array of square tunnels. These structures are fairly rigid and can generally accommodate only small atoms such as Li and H.



1.3 URANIUM-OXYGEN SYSTEM

Although they are not considered as feasible insertion cathode materials due to their high cost and high molecular weight, the uranium oxides do possess a considerable variety of structures and oxidation states which make their study useful. The partial, binary phase diagram in Figure 1.3 shows that the uranium-oxygen system is quite complex. There exists between UO_2 and UO_3 a number of different phases including UO_{2+y} , U_4O_9 , U_3O_7 , U_3O_8 , and $\text{UO}_{2.9}$. The phases of most interest in this work, UO_3 and U_3O_8 , are both polymorphic and exhibit narrow ranges of non-stoichiometry. The existence of such a wide range of oxidation states from U(VI) to U(IV) identifies these compounds as potential candidates for insertion electrodes.



Work performed by Hawke (11) demonstrated the capability of all the UO_3 polymorphs to react with H_2 in the presence of a noble-metal catalyst to form H_xUO_3 . This success with hydrogen was extended by Lawrence (12) to the U_3O_8 phase. Alkali-metal insertion has also been accomplished using lithium and sodium. Lithium ternary phases of U_3O_8 , $\alpha\text{-UO}_3$, $\delta\text{-UO}_3$, and $\gamma\text{-UO}_3$ were made by both chemical and electrochemical means (13,14,15). Sodium insertion into these same phases was performed by chemical means (12,16). Attempts at inserting magnesium have been less successful. Fleetwood (17) was able to insert magnesium into $\alpha\text{-U}_3\text{O}_8$ to an apparent x -value of 0.44 by chemical means and 0.05 by electrochemical means. Kiang (18) reached an apparent x -value of 0.4 for $\delta\text{-UO}_3$ using a Grignard reagent. However, significant amounts of organic matter were also co-inserted with magnesium into the crystal structure.

Six polymorphs of uranium trioxide, with designations α , β , γ , δ , high pressure, and amorphous are known to exist. Pure individual phases are difficult to synthesize due to the proximity of their heats of formation (19). Another phase of interest which contains U(VI)

and U(V) is α - U_3O_8 . Structural comparisons of the U(VI) compounds with their W, Mo, and Re counterparts show the uranium oxides to be more complex generally. Reasons for this greater complexity stem from the larger size of the U(VI) cation which can attain coordination numbers greater than six. These compounds also are under the influence of the strong uranyl group, UO_2^{2+} , present in all but one of the UO_3 allotropes as a distinctive linear $[\text{O}=\text{U}=\text{O}]^{2+}$ moiety.

The electronic structure of the uranium oxides is based largely upon the 5f, 6d, 7s, and 7p orbitals of uranium and the oxygen 2s and 2p orbitals. A tentative energy level scheme for an isolated uranyl ion (20) is shown in Figure 1.4. The relative energies of the 5f and 6d orbitals shown in Figure 1.4 were deduced from electronic spectra and magnetic measurements of U(IV) compounds. Separation between the two levels increases with uranium's oxidation state, and therefore reduction of U(VI) to U(V) results in the filling of a 5f orbital.

It is well known that the 5f electrons which characterize the optical and magnetic properties of the actinides extend much further beyond the core than the 4f electrons in the lanthanides. As a consequence the crystal-field perturbation is of comparable magnitude to spin-orbit coupling and electronic repulsion interactions. Theoretical treatments of a single 5f electron in both axial (21-23) and octahedral (24-26) crystal fields show λ , the spin-orbit coupling constant, is roughly $2,000 \text{ cm}^{-1}$ in magnitude and Δ , the crystal field energy, is in the range $2,000 - 45,000 \text{ cm}^{-1}$. These studies are discussed in more detail in Chapter 6.

Studies of the electrical properties (27,28) suggest the uranium oxides are n-type semi-conductors with electrical conductivities of about $10^{-8} \Omega^{-1} \text{ cm}^{-1}$ at room temperature. The intrinsic band gap (ΔE) for UO_3 polymorphs is in the range $2.52 - 2.68 \text{ eV}$ ($20,325 - 21,616 \text{ cm}^{-1}$) and the activation energy (E_a) for U_3O_8 is 1.10 eV ($8,872 \text{ cm}^{-1}$). A theoretical model developed by Singh and Karkhanavala (29) for U_3O_8 proposes the 5f electrons exist as small polarons i.e. closely associated with uranium ions and move by a phonon-activated hopping mechanism. Electrons introduced into the uranium oxide during insertion



(1.7)

should behave similarly.

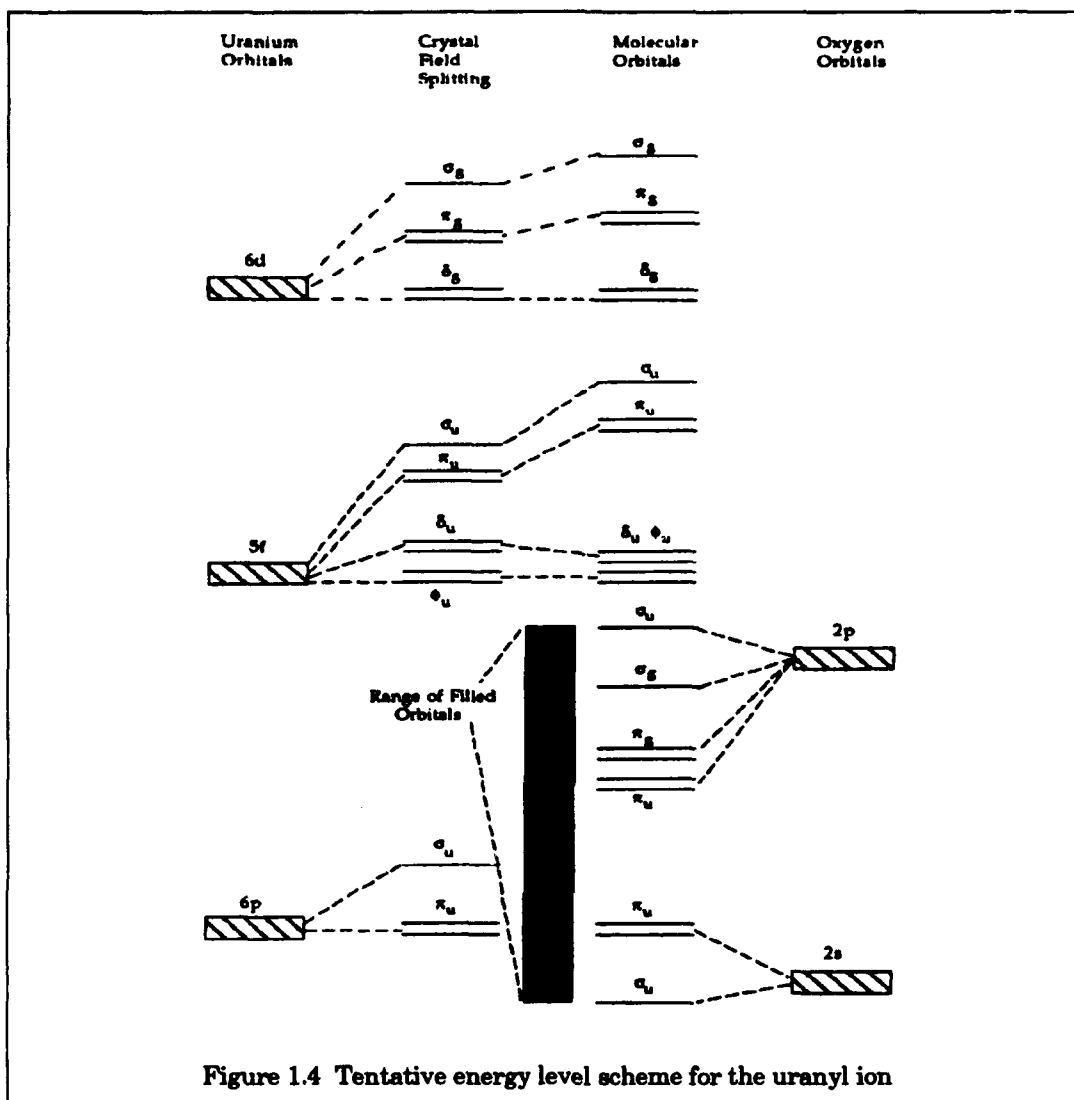


Figure 1.4 Tentative energy level scheme for the uranyl ion

1.3.1 $\gamma\text{-UO}_3$

One of the most complex structures of the uranium-oxygen system belongs to that of $\gamma\text{-UO}_3$, shown in Figure 1.5. There are two crystallographically distinct uranium atoms designated U(1) and U(2). U(2) atoms lie within octahedra which are canted in a staggered arrangement. These octahedra share edges to form chains running parallel to the a- and c-axes and perpendicular to one another at varying displacements along the b-axis. Linking these chains together into a three-dimensional network are the eight-coordinated U(1) atoms. Eight oxygens are arranged about U(1) atoms in a distorted dodecahedral geometry (30).

Alkali-metal insertion into $\gamma\text{-UO}_3$ has been limited to the lithium ion using both chemical and electrochemical methods (31). Four narrow, single-phase regions exist for values of $x < 1$ (Figure 1.6). Chemical lithiation has produced the $\gamma\text{-Li}_{0.33}\text{UO}_3$ and $\gamma\text{-Li}_{0.55}\text{UO}_3$ while $\gamma\text{-Li}_{0.67}\text{UO}_3$ was made electrochemically. Unit-cell dimensions for each of these compounds are listed in Table 1.1. Locations of the lithium ions are probably at the two tetrahedral interstitial sites denoted in Figure 1.5.

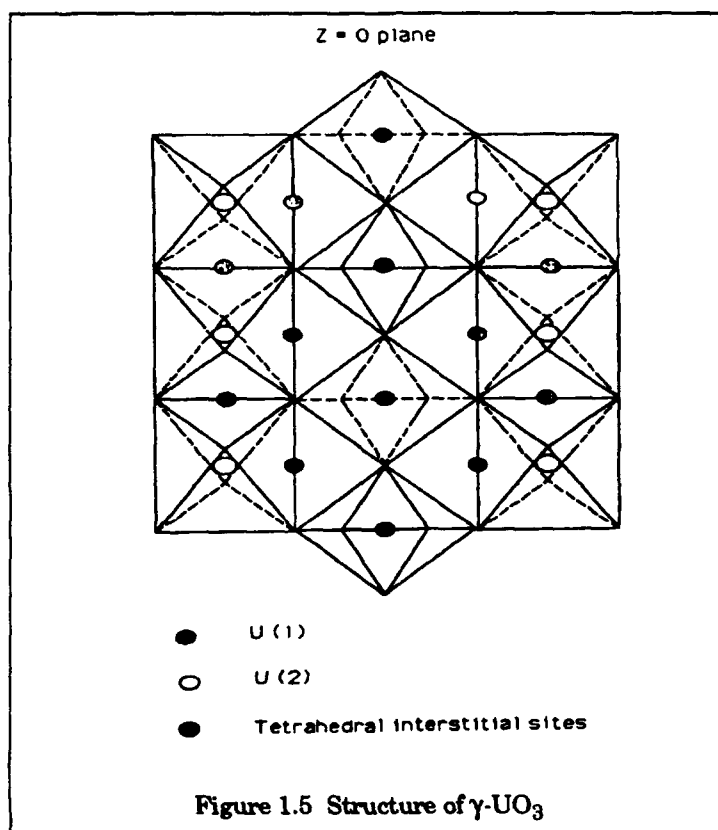
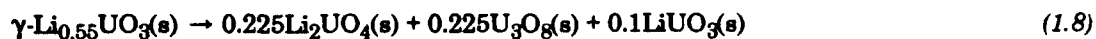


Table 1.1 Unit-cell dimensions of insertion compounds of $\gamma\text{-UO}_3$ (32)

Compound	a(Å)	b(Å)	c(Å)	Reference
$\gamma\text{-UO}_3$	6.890(2)	19.942(12)	6.985(12)	30
$\gamma\text{-Li}_{0.33}\text{UO}_3$	6.895(3)	19.949(14)	6.885(12)	14
$\gamma\text{-Li}_{0.55}\text{UO}_3$	6.902(5)	19.918(27)	6.971(17)	13
$\gamma\text{-Li}_{0.67}\text{UO}_3$	6.961(24)	19.857(66)	6.595(62)	31

The enthalpy of insertion for $\gamma\text{-Li}_{0.55}\text{UO}_3$ was measured by solution calorimetry and found to be -310 kJ mol^{-1} per mole of Li at 298.15K (13). This compound appears to be metastable as the enthalpy for disproportionation according to the reaction:



is -5 kJ mol^{-1} .

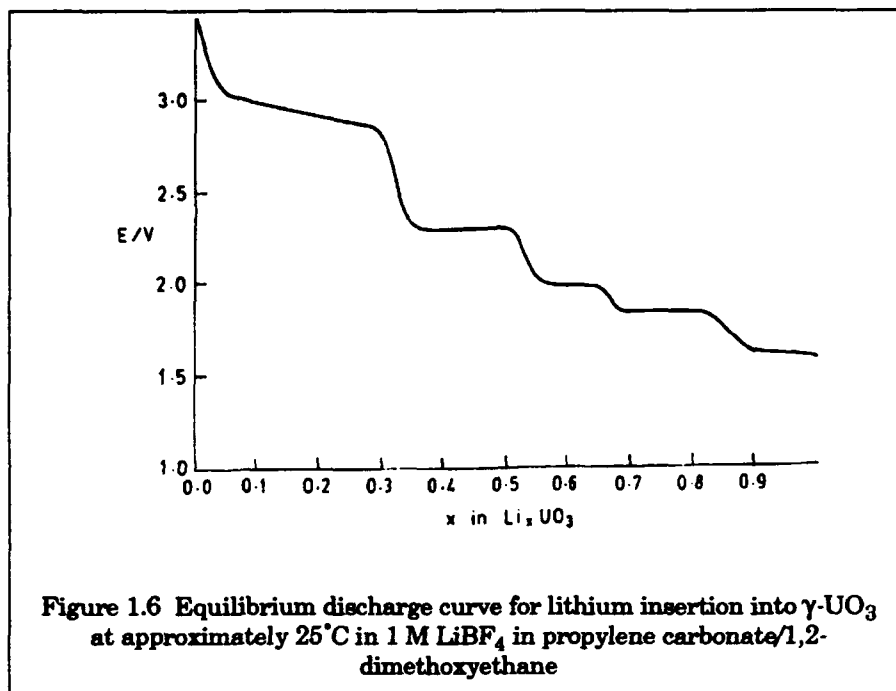
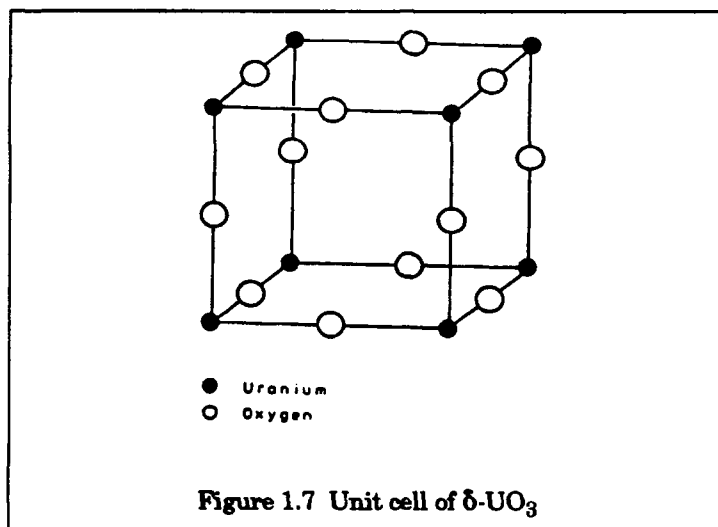


Figure 1.6 Equilibrium discharge curve for lithium insertion into $\gamma\text{-UO}_3$ at approximately 25°C in 1 M LiBF_4 in propylene carbonate/1,2-dimethoxyethane

1.3.2 $\delta\text{-UO}_3$

In contrast to $\gamma\text{-UO}_3$, the structure of $\delta\text{-UO}_3$ is quite simple (Figure 1.7) and assumes the classic ReO_3 structure consisting of vertex sharing UO_6 octahedra (33). The uranyl group is absent. The three-dimensional network contains numerous four-sided channels available as insertion sites.

Lithium, sodium, and magnesium have been inserted into $\delta\text{-UO}_3$ with the unit-cell dimensions given in Table 1.2. Dickens et al. (14,16) found that lithium forms a solid solution $\delta\text{-Li}_x\text{UO}_3$ for x -values less than 1.0. The compound $\delta\text{-Li}_{0.69}\text{UO}_3$ was prepared using LiI and its unit-cell dimension shows a contraction upon insertion. Ball (32) concludes this contraction is due to a distortion of the oxygen sublattice which provides lithium with square-planar coordination (Figure 1.8).

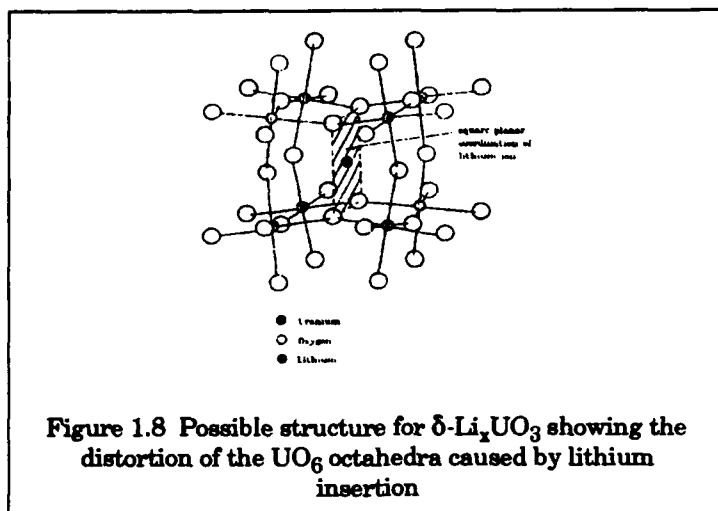
Table 1.2 Unit-cell dimensions of insertion compounds of δ - UO_3 (32)

Compound	$a(\text{\AA})$	Reference
δ - UO_3	4.145(5)	33
δ - $\text{Li}_{0.69}\text{UO}_3$	3.904(20)	13
δ - $\text{Na}_{0.31}\text{UO}_3$	4.165(3)	31
δ - $\text{Na}_{0.54}\text{UO}_3$	4.179(16)	15
δ - $\text{Mg}_{0.05}\text{UO}_3$	4.144	18
δ - $\text{Mg}_{0.07}\text{UO}_3$	4.152	18
δ - $\text{Mg}_{0.30}\text{UO}_3$	4.147	18
δ - $\text{Mg}_{0.40}\text{UO}_3$	4.150	18

The enthalpy change for the disproportionation of δ - $\text{Li}_{0.69}\text{UO}_3$ at ambient temperature is -3 kJ mol^{-1} , indicating metastability. An insertion enthalpy of -320 kJ mol^{-1} per mole of Li is approximately the same as the free energy of insertion, thus providing more evidence for small entropy changes occurring during topochemical reactions (13).

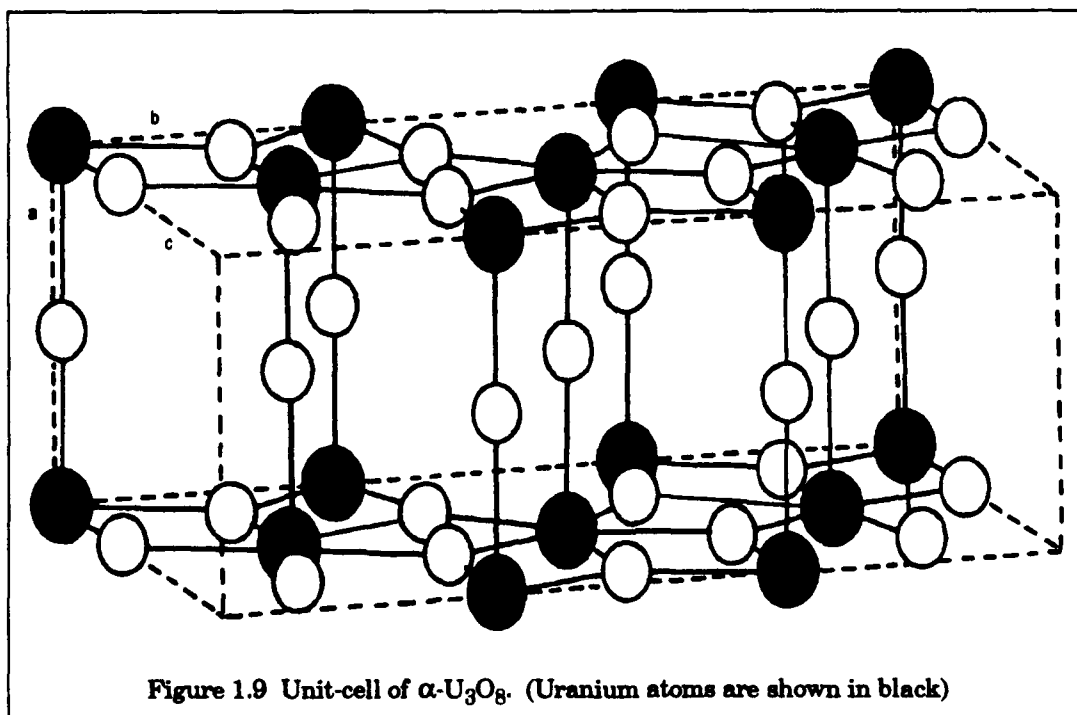
Sodium insertion into δ - UO_3 results in the cubic host in NaUO_3 assuming a distorted perovskite-like structure with the UO_6 octahedra canted (34). Unlike lithium, sodium expands the unit-cell as it occupies the center sites. Unit-cell dimensions for δ - $\text{Na}_{0.31}\text{UO}_3$ and δ - $\text{Na}_{0.54}\text{UO}_3$ are listed in Table 1.2.

Kiang (18) used both EtMgBr and $\text{MgI}_2 \cdot \text{Et}_2\text{O}$ to synthesize δ - Mg_xUO_3 ($x = 0.05, 0.07, 0.30, 0.40$). A significant amount of organic matter is also inserted using the Grignard reagent while the ether complex renders a maximum x -value of only 0.07.

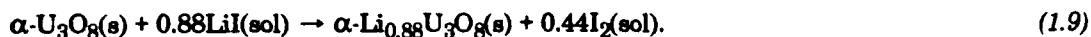


1.3.3 $\alpha\text{-U}_3\text{O}_8$

Figure 1.9 shows the unit-cell of $\alpha\text{-U}_3\text{O}_8$ with its layers of edge sharing UO_5 pentagons interconnected through O-U-O linkages. The basic unit-cell is orthorhombic (pseudo-hexagonal) (35). A phase transition occurs at 210°C resulting in $\alpha'\text{-U}_3\text{O}_8$ (36).



Ambient-temperature studies of lithium and sodium insertion into $\alpha\text{-U}_3\text{O}_8$ have been performed by Dickens et al. (15,37). Chemical insertion using LiI yields the pure phase $\alpha\text{-Li}_{0.88}\text{U}_3\text{O}_8$ according to the reaction



Electrochemical measurements show four single phase regions for $\alpha\text{-Li}_x\text{U}_3\text{O}_8$ with the following values for x :

Phase I: $0.78 < x < 0.87$

Phase II: $1.20 < x < 1.26$

Phase III: $1.56 < x < 1.65$

Phase IV: $1.95 < x < 2.07$.

These four phases correspond to the sloping regions of the discharge curve in Figure 1.10.

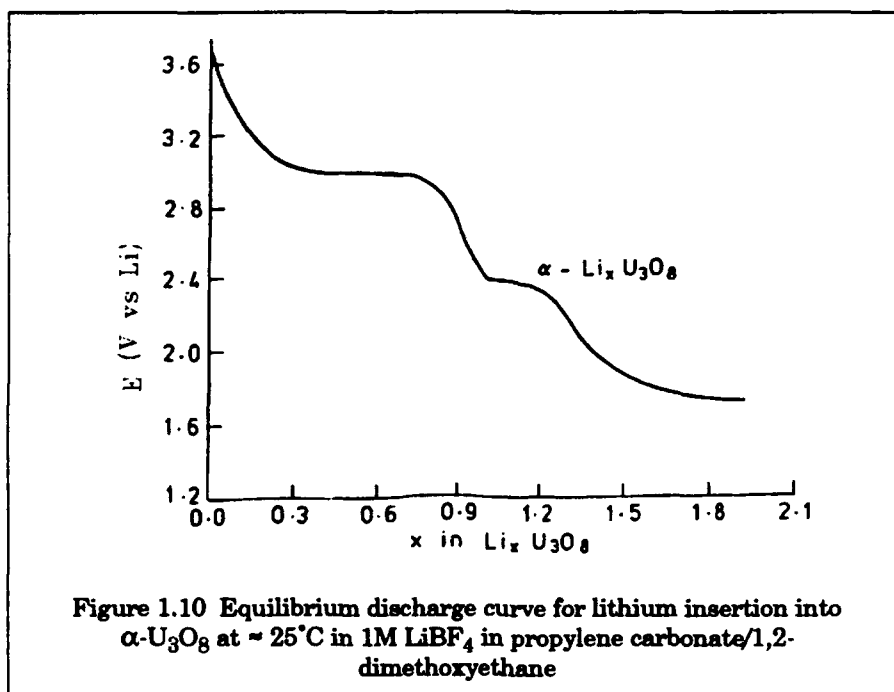


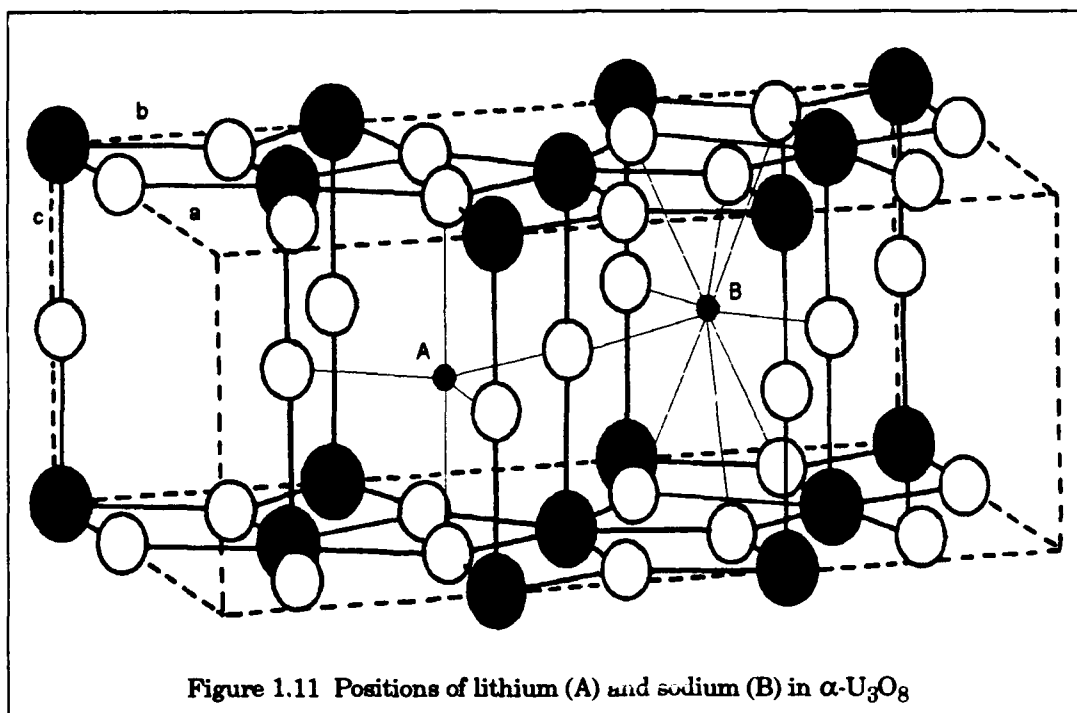
Figure 1.10 Equilibrium discharge curve for lithium insertion into $\alpha\text{-U}_3\text{O}_8$ at $\approx 25^\circ\text{C}$ in 1M LiBF_4 in propylene carbonate/1,2-dimethoxyethane

Lithium insertion into $\alpha\text{-U}_3\text{O}_8$ causes very little change in the parent oxide crystal structure according to powder X-ray diffraction. As evident from the refined lattice parameters given in Table 1.3, insertion must occur between the pentagonal layers, causing a slight increase in the c -parameter. Sodium inserts in the same manner, but its larger ionic radius causes a greater increase in the unit-cell dimensions. Neutron diffraction studies by Dickens and Powell (38) show that in $\text{Li}_{0.88}\text{U}_3\text{O}_8$ lithium occupies interstitial sites surrounded by oxygens in a distorted, trigonal bipyramidal geometry (Figure 1.11). Computer simulation studies by Ball and Dickens (39) for lithium agree with the neutron diffraction data. Sodium, on the other hand, is predicted to reside in larger, interstitial sites with a nine-coordinate arrangement of oxygen atoms (Figure 1.11).

Table 1.3 Unit-cell dimensions of insertion compounds of α - U_3O_8 (32)

Compound	a(Å)	b(Å)	c(Å)	Reference
α - U_3O_8	6.715(2)	11.968(4)	4.143(1)	13
α - $\text{Li}_{0.88}\text{U}_3\text{O}_8$	6.727(5)	11.953(3)	4.188(2)	13
α - $\text{Na}_{1.29}\text{U}_3\text{O}_8$	6.875(4)	12.630(9)	4.267(7)	15

Good agreement for the heat of lithium insertion into α - U_3O_8 exists between solution calorimetry measurements ($\Delta H = -298 \text{ kJ mol}^{-1}$ per mole Li) and electrochemical measurements of voltage versus composition. The closeness of ΔH and ΔG values is again compatible with the small entropy change associated with many solid-state reactions (13).

Figure 1.11 Positions of lithium (A) and sodium (B) in α - U_3O_8

1.3.4 α - UO_{3-x}

The structure of α - UO_{3-x} , ($0 \leq x \leq 0.11$) is very similar to that of α - U_3O_8 with approximately 12% of the uranium atoms removed (41). Consequently, as shown in Figure 1.12, about 25% of the oxygen atoms within the pillars are doubly bound to a uranium atom. Hawke (11) observed in the infrared spectrum of α - UO_3 the characteristic stretching frequencies associated with the uranyl grouping. Zachariasen (42) had reported previously the unit-cell of α - UO_3 as hexagonal with the dimensions given in Table 1.4.

Lithium, sodium, and hydrogen have all been inserted into α - UO_3 (Table 1.4) at both ambient and elevated temperatures by chemical and/or electrochemical means (11-16,43) with little structural change. The vacant uranium sites appear to be the most favorable for initial alkali-metal insertion with a capacity equivalent to $x \approx 0.15$. These sites are exclusively occupied by Na in the high-temperature compound α - $\text{Na}_{0.15}\text{UO}_3$ as is evident from the absence of the uranyl peaks in the infrared spectrum (16,44). However, the uranyl absorption band is present in α - $\text{Na}_{0.24}\text{UO}_3$ prepared at ambient temperature, suggesting that not all uranium vacancies are filled under the conditions of preparation (16). Hydrogen insertion results in a disappearance of uranyl stretching bands at 931 cm^{-1} and 890 cm^{-1} (44) which indicates the reduction in oxygen bond order from two to one upon the formation of hydroxyl groups or $\cdot\text{OH}_2$ groups. Hawke's (11) powder X-ray diffraction study of α - $\text{D}_{1.17}\text{UO}_3$ further supports this mode of hydrogen attachment.

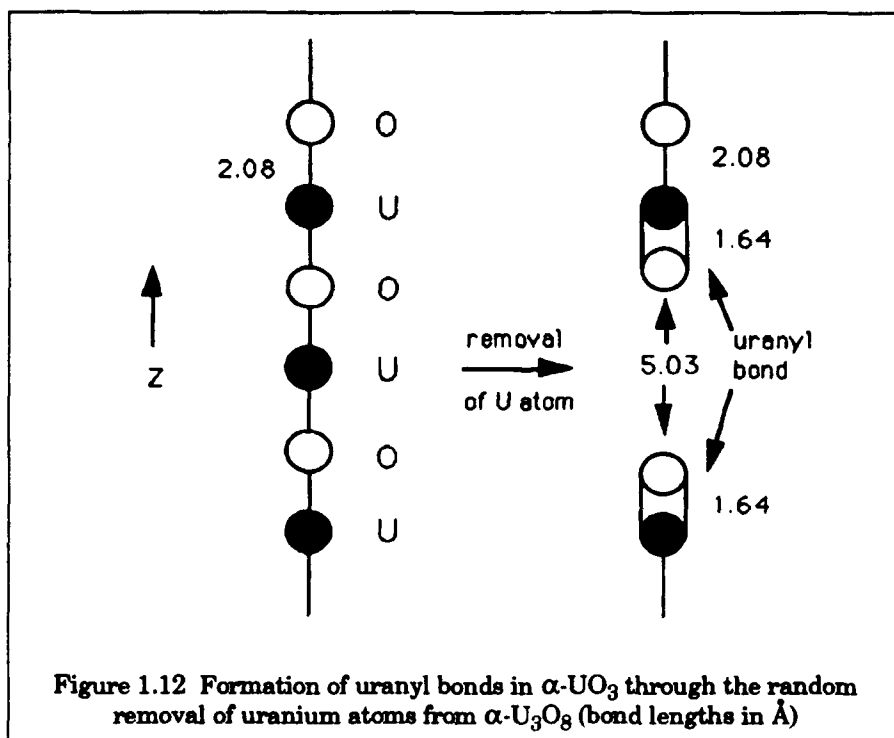
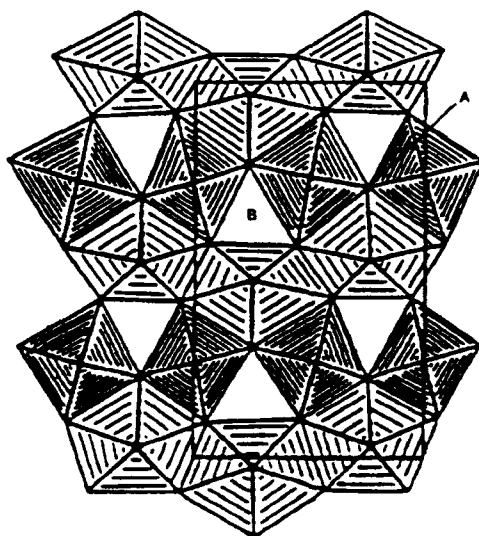


Table 1.4 Unit-cell dimensions of insertion compounds of α - UO_3 (32)

Compound	a(Å)	b(Å)	c(Å)	Reference
α - UO_3	3.971	3.971	4.170	42
α - $\text{Li}_{0.91}\text{UO}_3$	3.965(4)	3.965(4)	4.185(4)	14
α - $\text{Na}_{0.15}\text{UO}_3$	3.962(2)	3.962(2)	4.170(2)	44
α - $\text{Na}_{0.24}\text{UO}_3$	3.961	3.961	4.150	16
α - $\text{Na}_{0.59}\text{UO}_3$	3.997(6)	3.997(6)	4.223(8)	15
α - $\text{H}_{0.35}\text{UO}_3$	3.948	3.948	4.127	11
α - $\text{H}_{1.17}\text{UO}_3$	3.944	3.944	4.127	43

1.3.5 UTiO_5

U_3O_8 is the structural archetype for a number of mixed uranium/transition-metal oxides (UMO_5) such as UVO_5 , UTiO_5 , and USbO_5 which have in common pillared-layer structures consisting of planes of edge-sharing UO_n and MO_m polyhedra connected by metal-oxygen chains. Figure 1.13 shows the arrangement of the UO_5 pentagons and MO_6 octahedra within a single layer. Layers can stack in either registry to form monometallic M-O-M-O and U-O-U-O chains (e.g. UVO_5) or be displaced to form a heterometallic M-O-U-O-M chain (e.g. USbO_5 and UTiO_5). The unit cell in all cases is orthorhombic or pseudo-orthorhombic (45,46).

Figure 1.13 The structure of UTiO_5

Chemical insertion into UTiO_5 includes the ions Li^+ , Na^+ , H^+ , Mg^{2+} , and Zn^{2+} with U(VI) , and not Ti(IV) , being reduced upon insertion (45,47). Table 1.5 lists the lattice parameters of the unit-cells.

Table 1.5 Unit-cell dimensions of insertion compounds of UTiO_5 (45)

Compound	a(Å)	b(Å)	c(Å)
UTiO_5	7.35	6.29	15.56
$\text{Li}_{0.69}\text{UTiO}_5$	7.43	6.41	16.00
$\text{Mg}_{0.14}\text{UTiO}_5$	7.383	6.35	15.71
$\text{Na}_{0.60}\text{UTiO}_5$	7.49	6.38	18.25
$\text{Zn}_{0.08}\text{UTiO}_5$	7.38	6.31	15.67
$\text{H}_{0.98}\text{UTiO}_5$	7.46	6.48	15.74

1.4 PURPOSE OF THIS WORK

The purposes of this work are:

1. To identify reagents suitable for the chemical insertion of Na^+ , Mg^{2+} , and Zn^{2+} into various polymorphs of uranium oxides at ambient temperature and to characterize the insertion compounds formed using standard analytical methods;
2. To develop and use non-aqueous electrochemical systems for the chronopotentiometric insertion of monovalent (e.g. Na^+) and divalent (e.g. Mg^{2+} and Zn^{2+}) metal cations into uranium oxides and mixed uranium oxides, and with these systems measure thermodynamic and kinetic properties of the insertion process;
3. To investigate mechanistic aspects of the insertion process for uranium oxides using cyclic voltammetry; and
4. To examine the magnetic properties of uranium oxides and their insertion compounds in the temperature range 6 K - 300 K in order to obtain information about their electronic structure and the changes associated with insertion.

REFERENCES

1. Handbook of Batteries and Fuel Cells, (D. Linden ed.), McGraw Hill, New York, (1984).
2. M. S. Whittingham, *J. Electrochem. Soc.*, **123**, 325, (1976).
3. A. M. Chippindale, P. G. Dickens, and A. V. Powell, *Prog. Sol. State Chem.*, **21**, 133, (1991).
4. W. Rudorff, *Agnew. Chem.*, **71**, 438, (1959).
5. W. Rudorff, and H. H. Sick, *Agnew. Chem.*, **71**, 127, (1959).
6. I. Faul and J. Knight, *Chem. Ind.*, 820, (18 Dec 1989).
7. J. P. Gabano, *GS News Tech. Rpt.*, **47**, 1, (1988).
8. M. S. Whittingham, Paper 160, 145th Meeting of the Electrochemical Society, San Francisco, California, 398, (May 74).
9. M. S. Whittingham, *J. Electrochem. Soc.*, **122**, 713, (1975).
10. P. G. Dickens and M. F. Pye, in Intercalation Chemistry, (M. S. Whittingham and A. J. Jacobson eds.), Academic Press, NY, (1982).
11. S. V. Hawke, *Chemistry Part II Thesis*, Oxford, (1983).
12. S. D. Lawrence, *Chemistry Part II Thesis*, Oxford, (1984).
13. P. G. Dickens, S. D. Lawrence, D. J. Penny, and A. V. Powell, *Sol. State Ionics*, **32/33**, 77, (1989).
14. P. G. Dickens, D. J. Penny, and M. T. Weller, *Sol. State Ionics*, **5**, 778, (1986).
15. P. G. Dickens, A. V. Powell, and A. M. Chippindale, *Sol. State Ionics*, **28-30**, 1123, (1988).
16. A. V. Powell, *Chemistry Part II Thesis*, Oxford, (1986).
17. J. M. Fleetwood, *Chemistry Part II Thesis*, Oxford, (1989).
18. W. Kiang, *Chemistry Part II Thesis*, Oxford, (1987).
19. E. H. P. Cordfunke, *J. Phys Chem.*, **68**, 3463, (1964).
20. R. G. Denning, *Structure and Bonding*, **79**, 215, (1992).
21. J. C. Eisenstein and M. H. L. Pryce, *Proc. Roy. Soc.*, **A229**, 20, (1955).
22. J. C. Eisenstein and M. H. L. Pryce, *Proc. Roy. Soc.*, **A255**, 181, (1960).
23. J. C. Eisenstein and M. H. L. Pryce, *J. Res. Nat. Bureau Standards-A Phys. and Chem.*, **69A**, 3, 217, (1965).
24. C. J. Ballhausen, *Theor. Chim. Acta*, **24**, 234, (1972).
25. H. G. Hecht, W. B. Lewis, and M. P. Eastman, *Adv. Chem. Phys.*, **21**, 351, (1971).
26. N. Edelstein, *Rev. Chim. Miner.*, **14**, 149, (1977).

27. A. M. George and M. D. Karkhanavala, *J. Phys. Chem. Solids*, **24**, 1207, (1963).
28. Z. M. Hanafi, F. M. Ismail, M. A. Khilla, and N. H. Rofail, *Radiochim. Acta*, **49**, 35, (1990).
29. N. Singh and M. D. Karkhanavala, *Phys. Stat. Solidi*, **17**, 501, (1966).
30. R. Engmann and P. M. de Wolff, *Acta Cryst.*, **16**, 993, (1963).
31. D. J. Penny, Chemistry Part II Thesis, Oxford, (1985).
32. R. G. J. Ball, AERE R 13506, Chemistry Division Harwell Laboratory, (1989).
33. E. Wait, *J. Inorg. Nucl. Chem.*, **1**, 319, (1955).
34. A. M. Chippindale, P. G. Dickens, and W. T. A. Harrison, *J. Sol. State Chem.*, **78**, 2, 256, (1989).
35. B. O. Loopstra, *Acta Cryst.*, **17**, 651, (1964).
36. B. O. Loopstra, *J. Appl. Cryst.*, **3**, 94, (1970).
37. P. G. Dickens, S. D. Lawrence, and M. T. Weller, *Mater. Res. Bull.*, **20**, 636, (1985).
38. P. G. Dickens and A. V. Powell, *J. Sol. State Chem.*, **92**, 159, (1991).
39. R. G. J. Ball and P. G. Dickens, *J. Mater. Chem.*, **1**, 3, 425, (1991).
40. Gmelin Handbook of Inorganic Chemistry, Sup. C2, Springer Verlag (Berlin), 1978.
41. C. Greaves and B. E. F. Fender, *Acta Cryst.*, **B28**, 3709, (1972).
42. W. H. Zachariasen, *Acta Cryst.*, **1**, 265, (1948).
43. P. G. Dickens, S. V. Hawke, and M. T. Weller, *Mater. Res. Bull.*, **19**, 544, (1984).
44. C. Greaves, A. K. Cheetham, and B. E. F. Fender, *Inorg. Chem.*, **12**, 3003, (1973).
45. M. J. Woodall, Chemistry Part II Thesis, Oxford, (1992).
46. A. Sleight and K. Aykan, *J. Am. Ceramic Soc.*, **53**, 8, 427, (1970).
47. P. G. Dickens, A. V. Powell, and G. P. Stuttard, NIST Special Pub. 804, January 1991.

CHAPTER 2 PREPARATION AND CHARACTERIZATION OF COMPOUNDS

2.1 ANALYTICAL METHODS USED FOR CHARACTERIZATION

The principal analytical techniques used to characterize compounds were powder X-ray diffraction, atomic absorption spectroscopy, titrimetry, infrared spectroscopy, and elemental analysis.

2.1.1 POWDER X-RAY DIFFRACTION

A Philips vertical diffractometer consisting of an AMR 3-202 focusing monochromator, a PW 1964/60 scintillation detector (incorporating a NaI crystal and photomultiplier) and a PW 1390 channel control unit with a CuK_α radiation source was used to obtain powder X-ray diffractograms of all materials. Patterns were used to check the purity of the parent oxides which could, in turn, be used for comparison with the corresponding insertion compounds.

Potassium chloride (BDH, AnalaR) was added to each sample as a standard. Recorded spacing values were adjusted according to a linear regression equation derived from the standard. Data were refined using a computer program (1) that uses an iterative least-squares procedure to minimize the expression:

$$M = \sum (\sin_i^2 \Theta_{\text{obs}} - \sin_i^2 \Theta_{\text{calc}})^2. \quad (2.1)$$

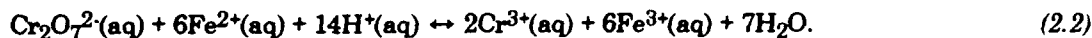
2.1.2 ATOMIC ABSORPTION SPECTROSCOPY

Atomic absorption spectroscopy was used to verify the amount of the inserted metal present in the host metal oxide. Electrodes were washed in propylene carbonate (Aldrich) and tetrahydrofuran (Aldrich) to remove any trace of the electrolyte and then dissolved in a hot solution of 34% HNO_3 . The Analytical Services Department of the ICL performed the analysis using a Perkin-Elmer Model 5000 AA Spectrophotometer.

2.1.3 TITROMETRY

Titrimetry provided another means of measuring the degree of insertion into the host uranium oxide. Samples of a known mass between 50 and 100 mg were dissolved in an aqueous solution of acidified 0.02M $\text{K}_2\text{Cr}_2\text{O}_7$. The dichromate ion oxidizes the reduced metal

to the +6 state as itself reduces to Cr^{3+} . The amount of $\text{Cr}_2\text{O}_7^{2-}$ remaining is determined by back titration with 0.05M $(\text{NH}_4)_2\text{Fe}(\text{SO}_4)_2$ which reacts according to the following equation:



The difference between the initial and final dichromate ion concentrations was used to calculate the mean oxidation state of the host metal ion.

2.1.4 INFRARED SPECTROSCOPY

Infrared absorption spectroscopy was used to compare insertion compounds with their parent metal oxides. Spectra were recorded on a Polaris Fourier transform infrared spectrophotometer ($400 - 4000 \text{ cm}^{-1}$). Samples were pressed into thin windows using cesium iodide (BDH, Spectrosol) in excess as the support.

2.1.5 ELEMENTAL ANALYSIS

Analyses for the elements carbon, hydrogen, and nitrogen were necessary to verify the solvent had not been incorporated with the insertion process. The Analytical Services Department of the ICL made these measurements using a Hewlett-Packard model 185 C-H-N Analyzer.

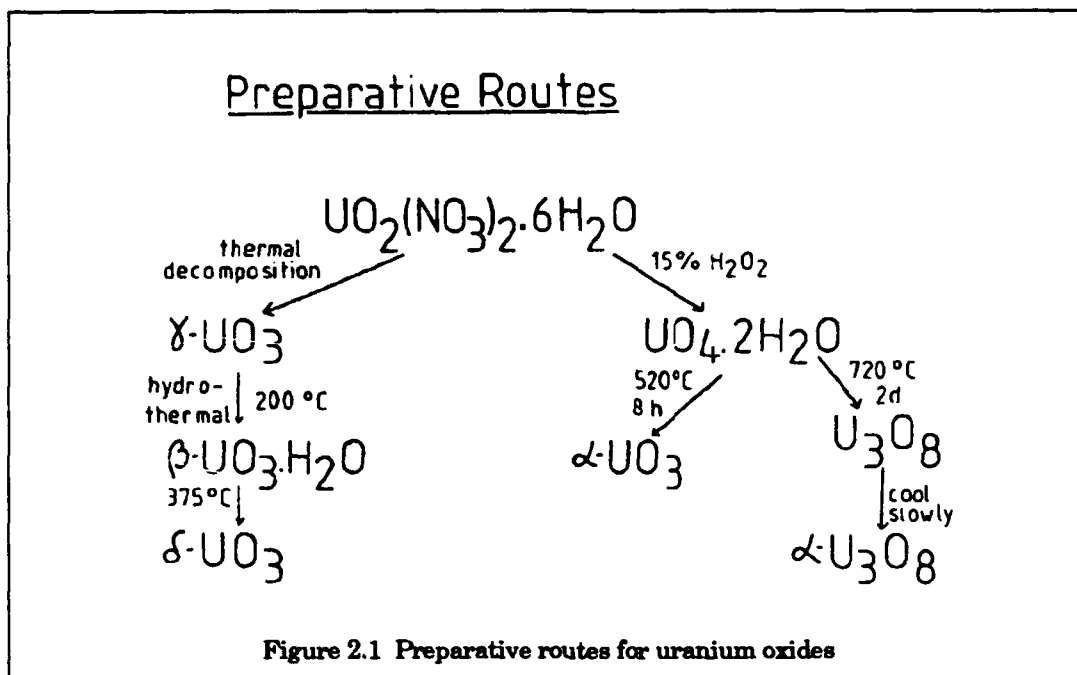
2.2 PREPARATION OF COMPOUNDS

The compounds $\gamma\text{-UO}_3$, $\delta\text{-UO}_3$, $\alpha\text{-UO}_{3-x}$, and $\alpha\text{-U}_3\text{O}_8$ were prepared from uranyl nitrate hexahydrate. Figure 3.1 summarizes the various preparative routes for the starting materials.

2.2.1 $\gamma\text{-UO}_3$

Uranyl nitrate hexahydrate (BDH, AnalaR) was placed inside an alumina boat on top of which was set, in an inverted position, a second alumina boat. This vessel was put into a tube furnace through which oxygen flowed and heated according to the temperature profile shown in Figure 2.2. The placement of the second alumina boat on top of the first was necessary to maintain the surface temperature at a level high enough to preclude the formation of $\alpha\text{-UO}_3$. Extended periods of heating at 200°C and 250°C were essential for the evolution of H_2O and NO_2 respectively. Although the reasons are not fully understood, this heating profile helps to ensure the sample does not become contaminated with other UO_3

polymorphs. The powder X-ray diffraction pattern (Appendix A) of the bright yellow solid closely matches that Loopstra et al. (2) give for $\gamma\text{-UO}_3$.



2.2.2 $\delta\text{-UO}_3$

This brick-red solid was made by first placing $\gamma\text{-UO}_3$ into a Princeton Applied Research Corporation 50 ml acid bomb with excess water and heating it at 220°C for 96 hours. The pale yellow solid recovered after repeated washing with H_2O and centrifuging was $\beta\text{-UO}_3\cdot\text{H}_2\text{O}$ (3,4). This intermediate was then heated under flowing nitrogen in an alumina boat at a temperature of 375°C for 72 hours to obtain $\delta\text{-UO}_3$. The powder X-ray diffraction pattern consisted of weak broad peaks, as was reported by Penny (5). The pattern (Appendix A) was indexed on a cubic unit cell which agreed with that of Wait (6) for $\delta\text{-UO}_3$.

2.2.3 $\alpha\text{-UO}_{3-x}$ and $\alpha\text{-U}_3\text{O}_8$

The preparation of $\alpha\text{-UO}_{3-x}$ and $\alpha\text{-U}_3\text{O}_8$ began by heating 100 ml of 0.5 M uranyl nitrate hexahydrate in 0.1 M HNO_3 to 90°C and adding dropwise 15 ml of 10% H_2O_2 while continuously stirring the solution. Upon completion of peroxide addition, the solution was maintained at 90°C for one hour. After cooling the precipitate was filtered and repeatedly washed with H_2O to remove any nitrate ion impurities. This intermediate, $\text{UO}_4\cdot 2\text{H}_2\text{O}$, was subsequently heated to 520°C in air for 2-8 hours to produce $\alpha\text{-UO}_{3-x}$ with an actual

stoichiometry in the range $\text{UO}_{2.90-2.95}$. Additional heating at 720°C in air for 16 hours produced $\alpha\text{-U}_3\text{O}_8$. The final products were tan ($\alpha\text{-UO}_3$) and dark green powder ($\alpha\text{-U}_3\text{O}_8$) which had powder X-ray diffraction patterns (Appendix A) in agreement with Greaves and Fender (7) and Loopstra (8) respectively.

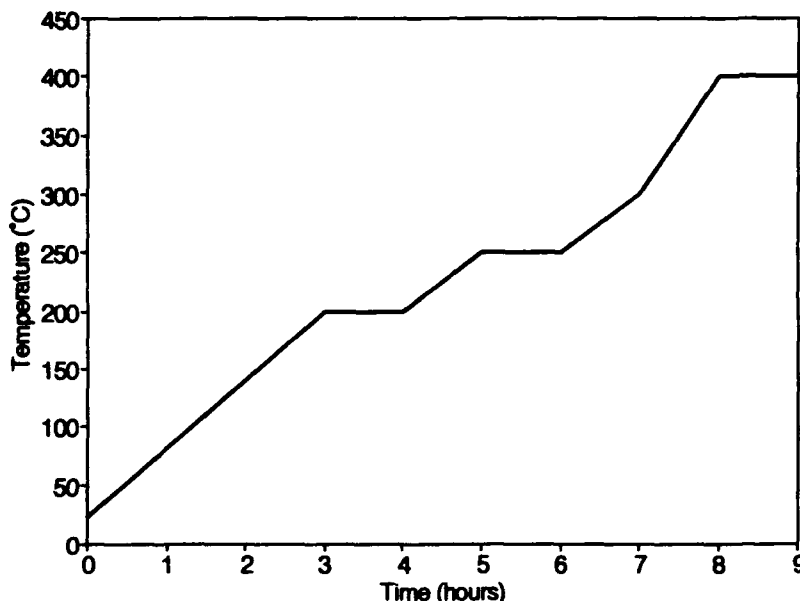


Figure 2.2 Heating profile for the preparation of $\gamma\text{-UO}_3$

2.2.4 UTiO_5

Preparation of UTiO_5 (9) begins by hydrolyzing n-propyl titanate (Aldrich) with excess water to form a white gelatinous precipitate which dissolves in 2 M H_2SO_4 to give Ti(IV) (aq). Titanium concentration was checked by atomic absorption before adding $\text{UO}_2(\text{NO}_3)_2 \cdot 6\text{H}_2\text{O}$ to bring the U:Ti ratio to 1:1. Concentrated NH_3 was added in excess to precipitate uranium and titanium hydroxides. The precipitate was filtered, washed with dilute NH_3 and H_2O , and dried for 12 hours at 120°C . The solid was ground to a fine powder and heated in air for 24 hours at each of the following temperatures: 300°C , 400°C , 500°C , 600°C , and 750°C . This stepwise heating was necessary to prevent the formation of U_3O_8 . Powder X-ray diffraction (Appendix A) confirmed the product to be that reported by Bobo (10).

2.3 PREPARATION OF INSERTION COMPOUNDS

Chemically reduced compounds containing lithium, magnesium, and zinc (see Appendix A for powder X-ray diffraction patterns) were prepared by either of the following two general methods using standard Schlenk line techniques (see Figure 2.3). In the first method, a known amount of the oxide (UO_n), approximately one gram, was placed in a nitrogen-filled Schlenk tube containing 50 ml of either hexane or heptane. The alkanes were previously dried over type 3A molecular sieve for at least 1 month. The appropriate amount of 1.6 M n-butyllithium in hexane (Aldrich), 1.07 M dibutylmagnesium in heptane (Alfa), or 1.0 M diethylzinc in hexane (Aldrich) was then added to the tube using a syringe. Under constant stirring the reactions



were allowed to proceed from 1 to 14 days. The product was washed several times with alkane, dried under dynamic vacuum, and stored in a vacuum desiccator.

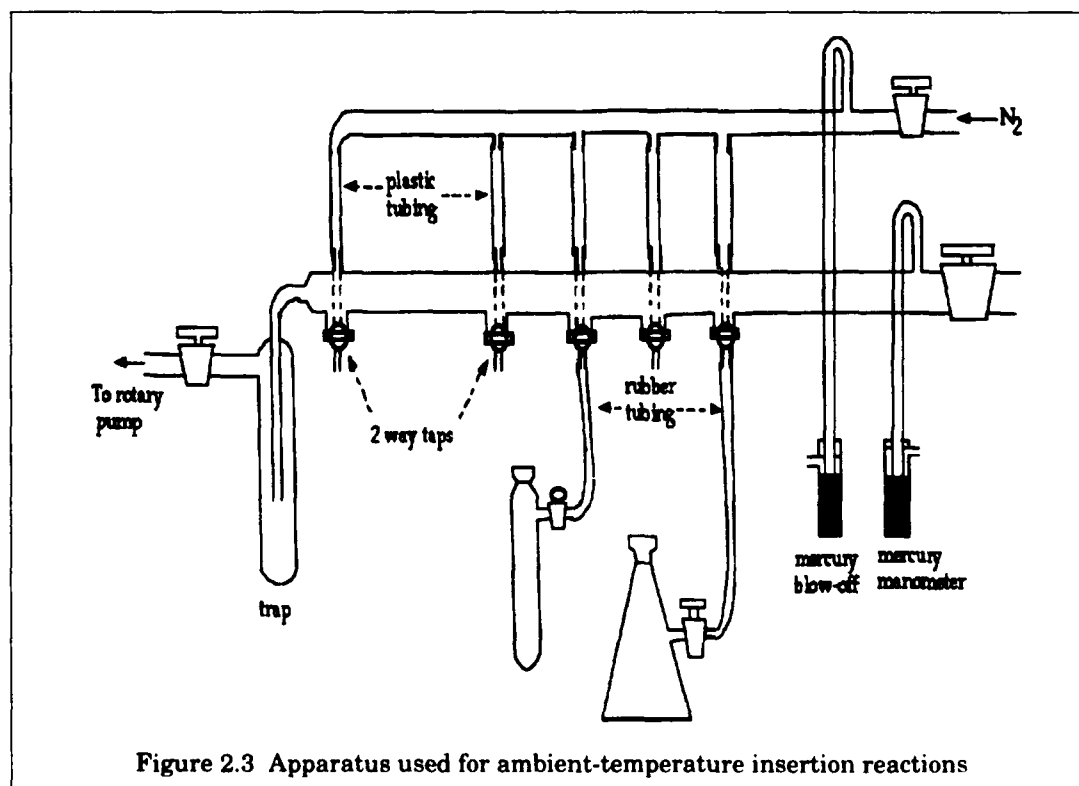


Figure 2.3 Apparatus used for ambient-temperature insertion reactions

A second method used for insertion was to grind together the appropriate amounts of lithium iodide (Aldrich), magnesium iodide ether complex (Alfa), or zinc iodide (Aldrich) and the oxide and add this mixture to a Schlenk tube containing 50 ml of carbon tetrachloride (BDH). The CCl_4 had previously been refluxed over P_2O_5 for several hours and then distilled. As the reaction progressed with continual stirring the solution became purple, indicating iodine was formed in the general reaction for metal (M) insertion



After at least 48 hours the product was then washed repeatedly with CCl_4 and diethyl ether (BDH, dried over type 3A molecular sieve) to remove the iodine and any unreacted metal iodide. The solid was dried under dynamic vacuum and stored in a vacuum desiccator.

Sodium insertion was done by reacting the oxide directly with excess sodium metal dissolved in ammonia (11) inside a Princeton Applied Research high-pressure bomb (Figure 2.4). Sodium and the metal oxide were loaded into the bomb inside a glove box and then attached to a vacuum line. The bomb was cooled to -78°C in a bath of dry ice and acetone and ammonia introduced until the pressure remained constant at 110 psi. The tap to the ammonia was closed and the vessel allowed to warm to room-temperature with continual stirring over a period of 6 hours. Upon completion of the reaction the bomb was evacuated and placed inside a glove box where the product was transferred to a Schlenk tube for washing with 2-propanol (Fisons) to remove unreacted sodium. The solid was dried under dynamic vacuum and stored in a vacuum desiccator.

2.4 CHARACTERIZATION OF INSERTION COMPOUNDS

Table 2.1 gives the refined lattice parameters of the uranium oxides and their insertion compounds. The amount of carbon and hydrogen detected by elemental analysis in the insertion compounds was less than 0.5 weight percent. Elemental analysis of sodium insertion compounds failed to identify the presence of nitrogen, which suggests ammonia does not co-insert with sodium. The x -values calculated from atomic absorption and reducing-power titrations for lithium and sodium compounds agreed, but were dissimilar for magnesium and zinc with the atomic absorption values significantly greater (see Table 2.2).

Values obtained from the reducing-power titrations were deemed more accurate and are those reported in Table 2.1.

The x -values for magnesium and zinc insertion show the maximum degree of insertion is less than that of lithium and sodium. Low x -values for magnesium insertion into a number of transition-metal oxides were also found by Gregory et al. (12) and Bruce et al. (13,14). Given the very low x -values for γ - UO_3 and δ - UO_3 , it is unlikely that insertion into these compounds occurred at all. Magnetic measurements of $\text{UO}_{2.90}$ insertion compounds, however, which will be discussed in Chapter 6, confirmed magnesium and zinc did insert to a small extent.

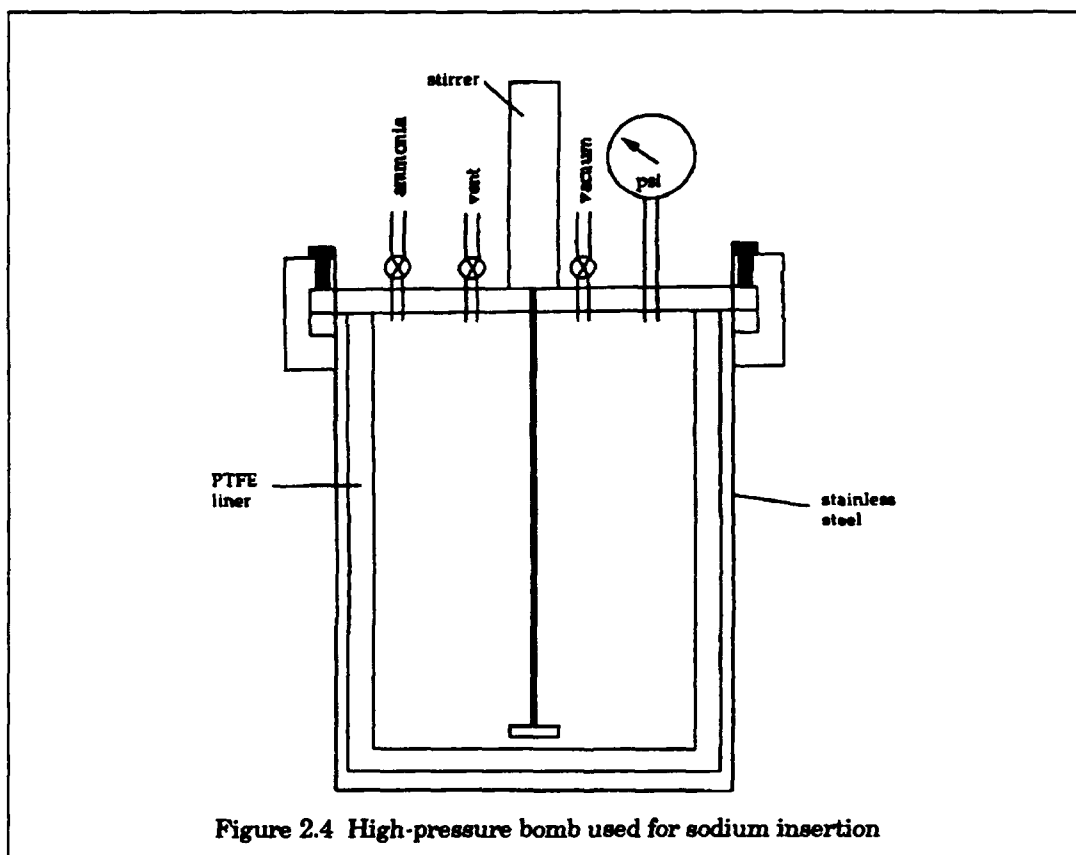


Figure 2.4 High-pressure bomb used for sodium insertion

It is probable that the low degree of magnesium and zinc insertion is due to thermodynamic and kinetic limitations of the reducing agents. In comparison to lithium, both magnesium and zinc are more electronegative, making them weaker reducing agents for the uranium oxides. The two-electron transfer further contributes to lower x -values. Reaction rates are also slower due to the relatively lower mobility of the divalent cations in

the solid host (more will be said about ionic mobility in Chapter 4). Longer reaction times and elevated reaction temperatures had little effect upon increasing x -values, although they may have indirectly contributed to the discrepancy between atomic absorption and titration x -values. Higher temperatures and longer reaction times would enable the reagents to react with contaminants (e.g. water, oxygen) to form insoluble impurities. Atomic absorption would detect these metal containing impurities to yield artificially high x -values. Since the titration only measures the change in oxidation state it is insensitive to the fully oxidized impurities, and therefore gives a more accurate x -value. Initial x -values for magnesium insertion into U_3O_8 (15) were subsequently found to be in error for this reason. It is now concluded that magnesium does not insert readily, or at all, into U_3O_8 by chemical means.

Table 2.1 Unit-cell dimensions (in Å) of uranium oxides and their insertion compounds (uncertainty values given in parentheses).

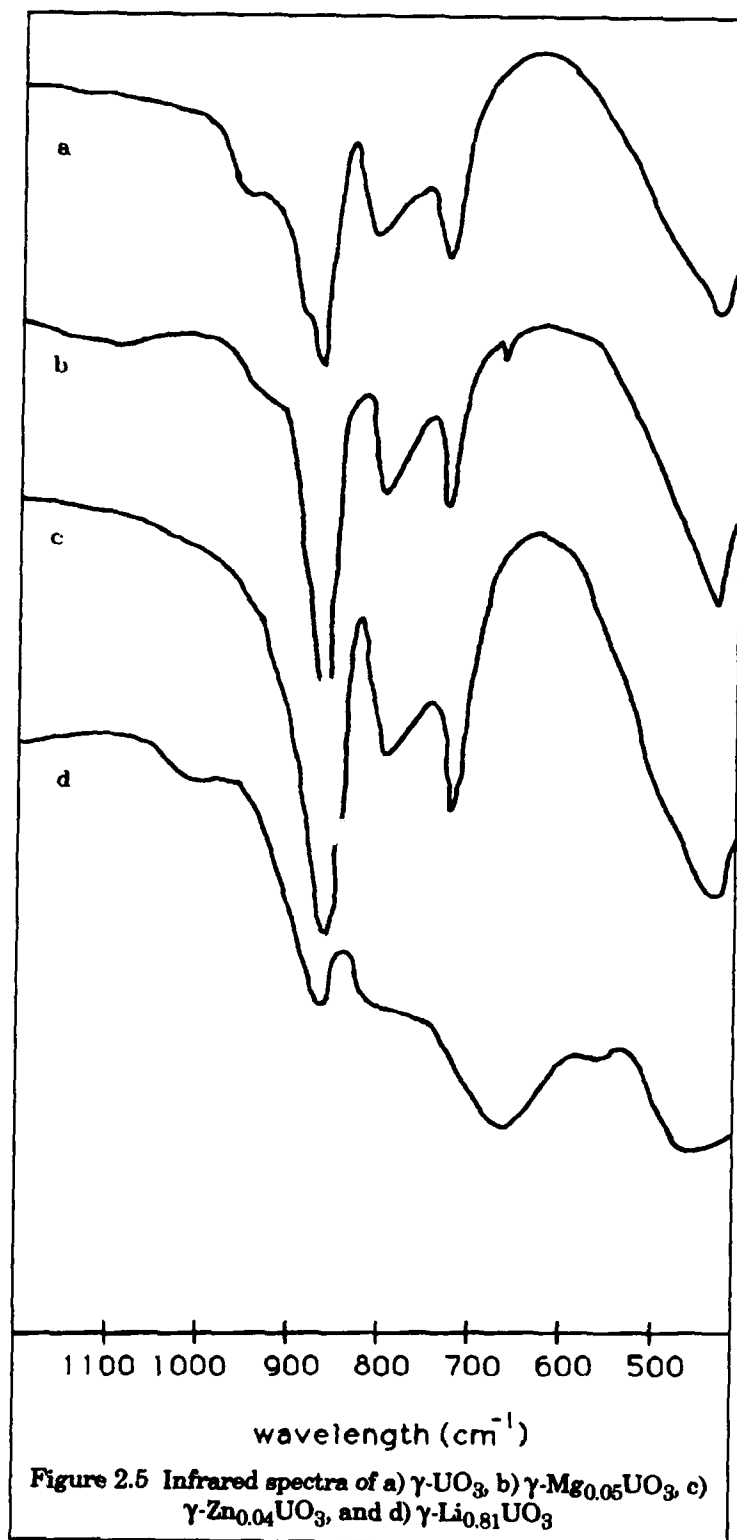
Compound	System	a	b	c
γ - UO_3	orthorhombic	6.896(5)	19.934(17)	6.877(20)
γ - $Li_{0.81}UO_3$		6.990(8)	19.856(69)	6.938(35)
γ - $Mg_{0.05}UO_3$		6.892(9)	19.982(32)	6.875(34)
γ - $Zn_{0.04}UO_3$		6.896(2)	19.929(9)	6.902(10)
δ - UO_3	cubic	4.146(7)		
δ - $Li_{0.69}UO_3$		4.110(14)		
δ - $Mg_{0.03}UO_3$		4.154(7)		
δ - $Zn_{0.02}UO_3$		4.131(6)		
$UO_{2.90}$	hexagonal	3.964(5)		4.172(9)
$Li_{0.42}UO_{2.90}$		3.953(7)		4.169(8)
$^*Na_{0.35}UO_{2.95}$		3.948(11)		4.160(15)
		4.010(38)		4.233(17)
$Mg_{0.09}UO_{2.90}$	orthorhombic	3.985(9)		4.163(13)
$Zn_{0.19}UO_{2.90}$		3.890(6)		4.170(8)
U_3O_8		6.710(3)	11.950(6)	4.138(2)
$Li_{0.85}U_3O_8$		6.788(14)	11.974(23)	4.193(5)
$Na_{0.31}U_3O_8$		6.720(2)	11.965(4)	4.150(2)
$UTiO_5$	orthorhombic	6.356(17)	7.364(10)	15.628(32)

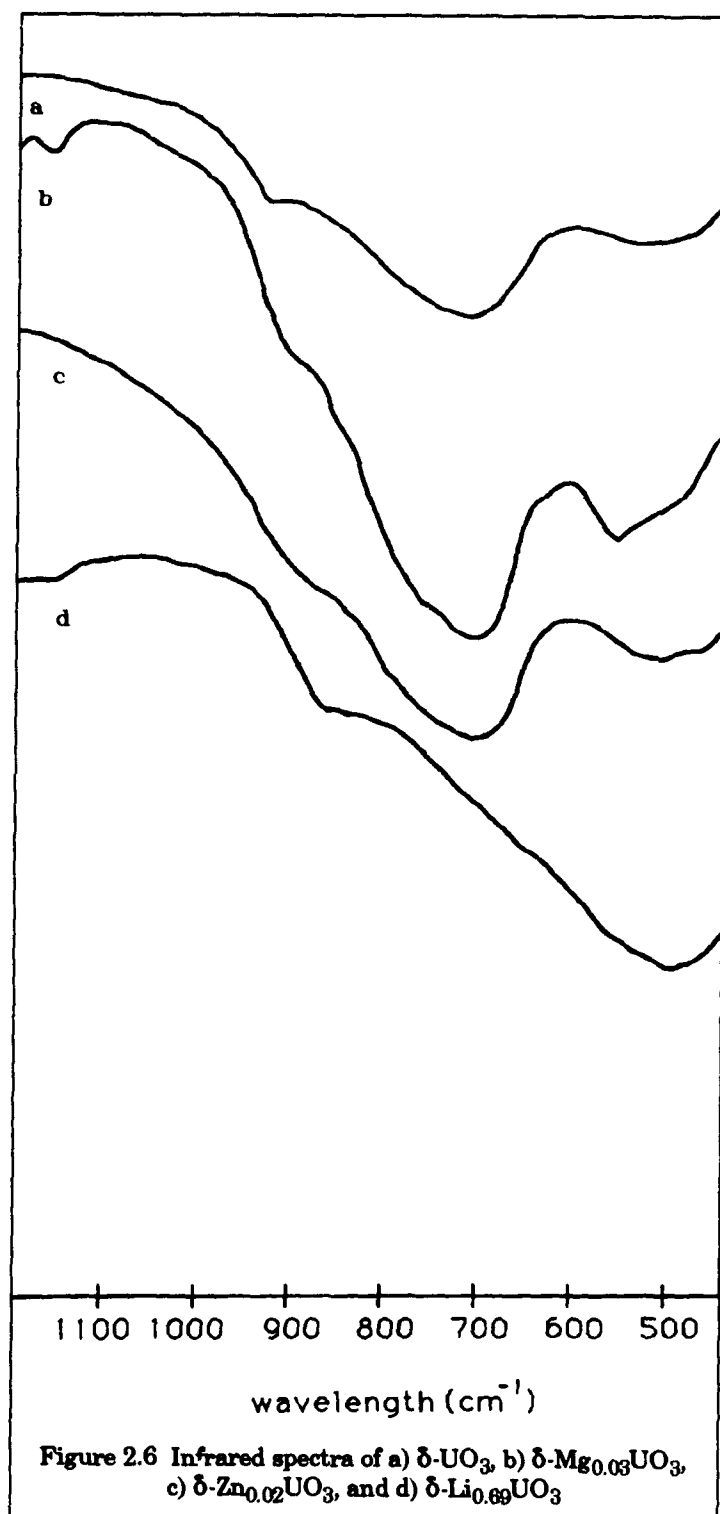
*Two phases observed in X-ray diffraction pattern

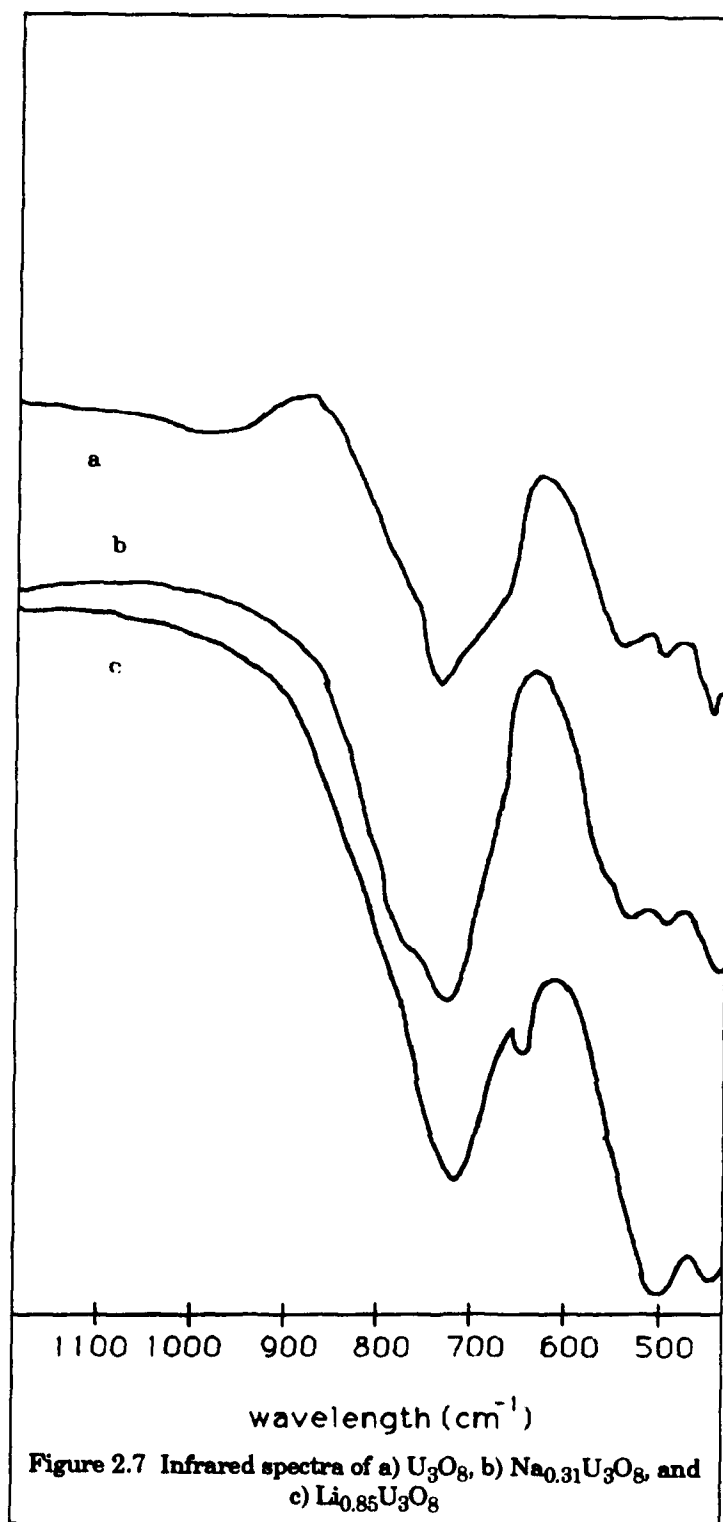
Table 2.2 Comparison of x-values for magnesium and zinc insertion as determined by atomic absorption and reducing-power titration

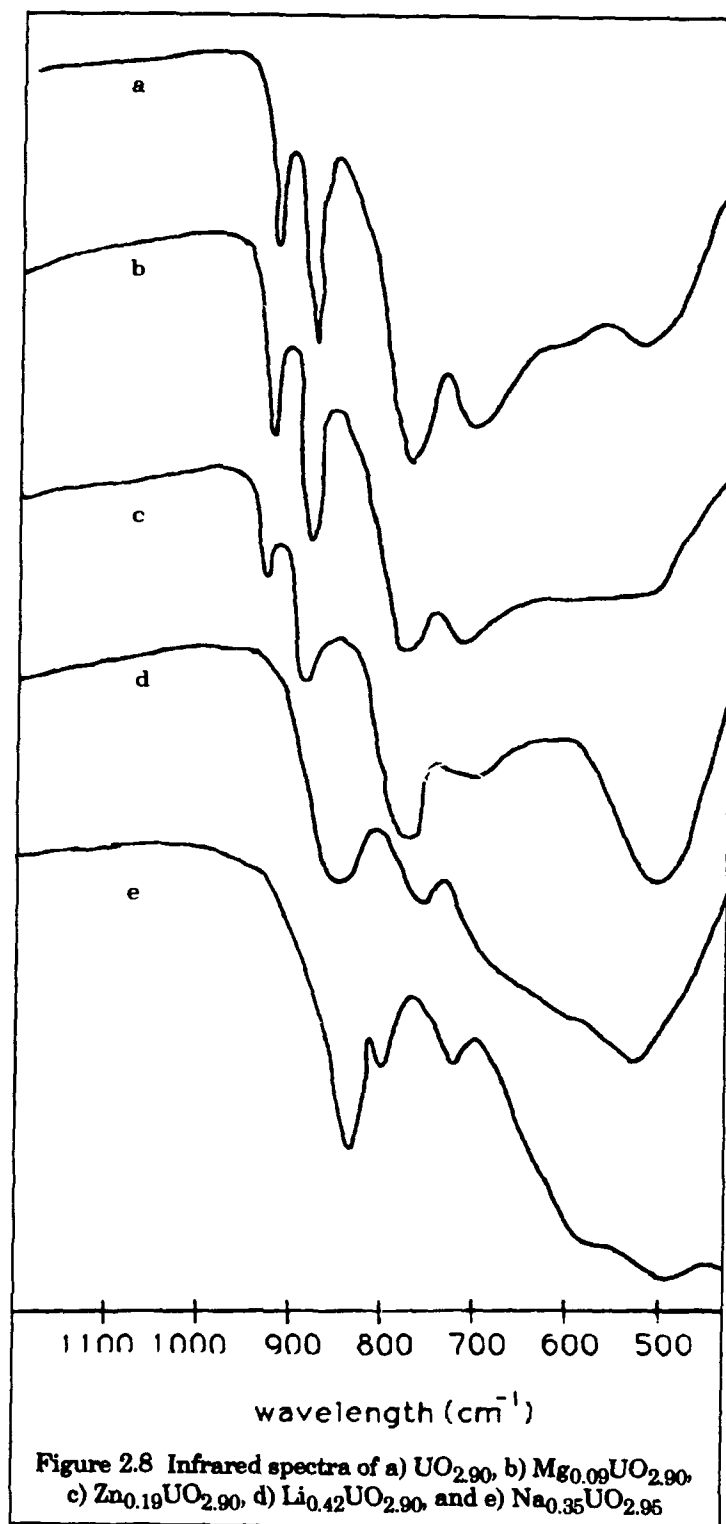
Compound	magnesium		zinc	
	AAS	titration	AAS	titration
γ - UO_3	0.15	0.05		0.04
δ - UO_3	0.08	0.03	0.16	0.02
$\text{UO}_{2.90}$	0.26	0.09	0.37	0.19
U_3O_8	0.21	0	0.09	0

Additional support for retention of the parent structures is given by the similarity of the infrared spectra (Figure 2.5 - 2.8) where peaks shifted only slightly after insertion. The presence of the two uranyl peaks at approximately 920 cm^{-1} and 860 cm^{-1} in $\text{Zn}_{0.19}\text{UO}_{2.90}$ indicates that zinc does not preferentially fill the uranium vacancies which give rise to $\text{U}=\text{O}$. Powell (16) reported this same finding for α - $\text{Na}_{0.24}\text{UO}_3$ with excess sodium occupying positions between layers. However, for $\text{Li}_{0.42}\text{UO}_{2.90}$ and $\text{Na}_{0.35}\text{UO}_{2.95}$ these peaks are replaced by a broad peak at $800 - 840\text{ cm}^{-1}$ and it is assumed the alkali-metal has occupied the uranium vacancies.









REFERENCES

1. M. F. Pye, Chemistry Part II Thesis, Oxford, (1975).
2. B. O. Loopstra, J. C. Taylor, and A. B. Waugh, *J. Sol. State Chem.*, **20**, 9, (1977).
3. S. V. Hawke, Chemistry Part II Thesis, Oxford, (1983).
4. V. J. Wheeler, R. M. Dell, and E. Wait, *J. Inorg. Nucl. Chem.*, **28**, 1829, (1964).
5. D. J. Penny, Chemistry Part II Thesis, Oxford, 1985.
6. E. Wait, *J. Inorg. Nucl. Chem.*, **1**, 309, (1955).
7. C. Greaves and B. E. F. Fender, *Acta Cryst.*, **B28**, 3609, (1972).
8. B. O. Loopstra, *Acta Cryst.*, **17**, 651, (1964).
9. G. P. Stuttard, Chemistry Part II Thesis, Oxford, (1990).
10. J. C. Bobo, *Rev. Chem. Minerale*, **1**, 3, (1964).
11. W. Rudorff, *Chemia*, **19**, 489, (1965).
12. T. D. Gregory, R. J. Hoffman, and R. C. Winterton, *J. Electrochem. Soc.*, **137**, 3, 775, (1990).
13. P. G. Bruce, F. Krok, J. Nowinski, V. Gibson, and K. Tavakkoli, *J. Mater. Chem.*, **1**, 705, (1991).
14. P. G. Bruce, F. Krok, P. Lightfoot, and J. Nowinski, *Sol. State Ion.*, **53-56**, 351, (1992).
15. R. E. Dueber, J. M. Fleetwood, and P. G. Dickens, *Sol. State Ion.*, **50**, 329, (1992).
16. A. V. Powell, Chemistry Part II Thesis, Oxford, (1986).

CHAPTER 3 ELECTROCHEMICAL CELL DEVELOPMENT

Chronopotentiometry is a very powerful technique for making insertion compounds and for obtaining structural, thermodynamic, and kinetic data. Systems studied using this technique must fulfill a number of requirements, two of which are chemical stability and reasonably rapid kinetics. This chapter discusses the development of the electrochemical cells which enabled insertion to be successfully studied using chronopotentiometry.

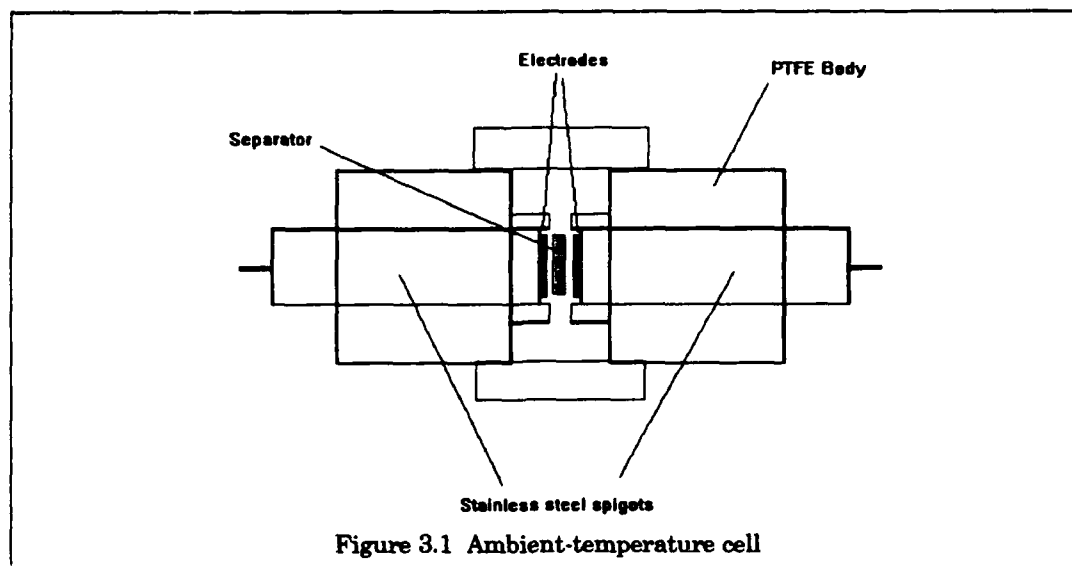
3.1 AMBIENT-TEMPERATURE CELLS

3.1.1 SODIUM AND ZINC INSERTION

The cell used for ambient-temperature insertion is shown in Figure 3.1 (1). A PTFE body houses two stainless steel spigots which maintain pressure on the electrodes as well as provide electrical contacts. Several disks of glass mat (Whatman) soaked in electrolyte separate the two electrodes. The working electrode consisted of 80 w/o metal oxide (≈ 50 mg), 10 w/o graphite (Koch), and 10 w/o PTFE (BDH) ground together and pressed at 5 tons on to stainless steel mesh 1 cm in diameter. The mesh was previously washed with 34% HNO_3 and distilled H_2O . Counter electrodes were disks of sodium (Aldrich, 99.9%) or zinc (Aldrich, 99.9%).

The electrolyte for sodium cells was 0.4 M NaClO_4 (Aldrich) dissolved in anhydrous propylene carbonate (Aldrich). Zinc triflate (Aldrich) dissolved in a 1:5 mixture of anhydrous propylene carbonate/dimethylsulfoxide (Aldrich) to a concentration of 0.2 M was used for zinc insertion. Solvents were used without further purification. Sodium perchlorate and zinc triflate were dried under vacuum at 50°C and 150°C respectively for 24 hours.

The anodic and cathodic limits of all electrolytes were measured at 25 μA on graphite and stainless steel electrodes. The results are shown in Appendix B.



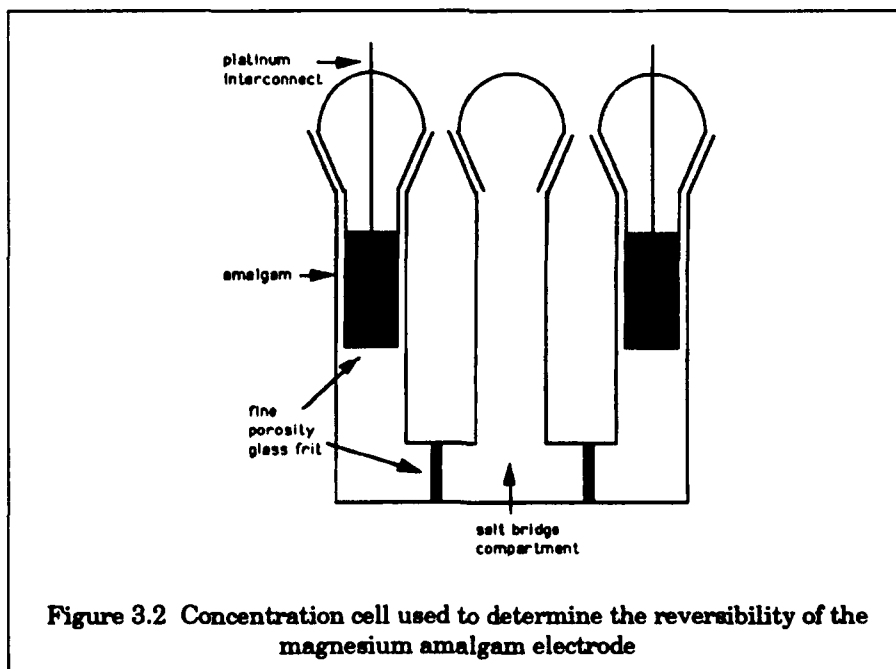
3.1.2 MAGNESIUM INSERTION

The true thermodynamic, equilibrium potential of any cell containing magnesium cannot be measured directly due to the irreversible behavior of pure magnesium in aprotic solvents (2,3). As Brown and McIntyre (4,5) point out, if the exchange current density (i_0) for magnesium is lower than that for other couples present (e.g. intrinsic impurities or magnesium-solvent reaction products) the open-circuit potential will be a mixed, nonthermodynamic value. Attempts to use pure magnesium as a reference electrode during the course of the present work failed for this reason. However, the Mg(Hg) amalgam electrode (with $x_{\text{Mg}} \approx 10^{-3}$) possesses a higher standard reduction potential in water ($E^\circ = -1.980$ V) than magnesium ($E^\circ = -2.375$ V) and is less reactive chemically. In addition, the i_0 value for Mg(Hg) should be greater than that for Mg since the amalgam is liquid at ambient-temperature. Brown and McIntyre (5) were able to measure the standard potential of Mg(Hg)/Mg²⁺ in various organic solvents. Given their success, Mg(Hg) was examined further in this work for its suitability as a reference electrode in an aprotic solvent.

Dilute magnesium amalgam was made following the method of Brown and McIntyre (4). A magnesium disk (Johnson-Matthey, 99.999%) was discharged into a pool of twice-distilled mercury (Johnson-Matthey) at a current density of 0.42 mA/cm² from a solution of 1 m MgCl₂ (Fluka) in N,N-dimethylformamide (DMF, Aldrich). The mole fraction of magnesium was determined by atomic absorption. Due to the reactivity of the amalgam with

water, exclusion of moisture was critical. The salt was dried at 190°C under dynamic vacuum for 15 hours. DMF was dried over type 4A molecular sieve for at least one month and then distilled under reduced pressure through a column containing molecular sieve. The salt, solvent, and amalgam were stored in an argon filled glove box.

Figure 3.2 is the concentration cell used to verify Nernstian behavior of the amalgam electrode. The potential of one amalgam electrode immersed in 0.105 M $\text{Mg}(\text{ClO}_4)_2$ DMF was measured against a second amalgam electrode immersed in various concentrations of $\text{Mg}(\text{ClO}_4)_2$ in DMF. The liquid junction potential was minimized by connecting the two solutions with a salt bridge containing 1 M tetraethylammonium perchlorate (TEAP) in DMF. Equilibrium potential measurements were made after the solutions and electrodes had been in contact for at least 2 hours. Magnesium perchlorate (Johnson-Matthey) was dried in the same manner as MgCl_2 . TEAP (Fluka) was dried in a vacuum desiccator at 40°C for 48 hours. All measurements were performed in an argon filled glove box at ambient-temperature ($\approx 23^\circ\text{C}$).



A good reference electrode must be reversible and provide a stable voltage. For a reversible $\text{Mg}^{2+}/\text{Mg}(\text{Hg})$ system, the equilibrium potential for a concentration cell without liquid junction is given by

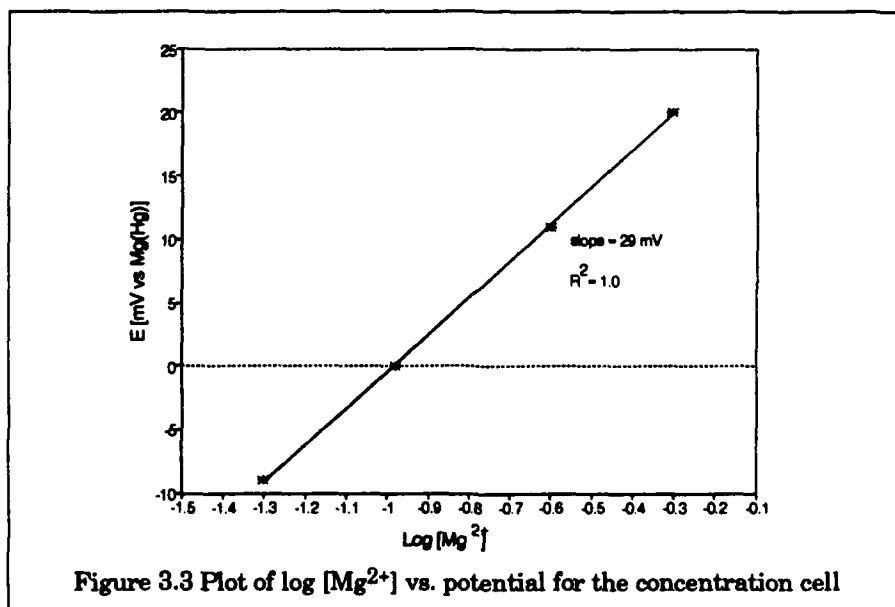
$$E = -2.303RT/(2F) \log[a_{\text{Mg}^{2+}_1} a_{\text{Mg(Hg)}_2} / a_{\text{Mg}^{2+}_2} a_{\text{Mg(Hg)}_1}] \quad (3.1)$$

where the subscripts denote the two different halves of the cell. The activity of Mg^{2+} can be approximated by its concentration assuming constant activity coefficients over the range of concentrations used. The Mg^{2+} concentration in one side of the cell is kept constant at 0.105 M while using an amalgam with the same magnesium activity in both sides of the cell cancels the remaining terms. Substituting for R and F at 296 K, equation 3.1 becomes

$$E = \text{constant} + 0.029 \log [\text{Mg}^{2+}]. \quad (3.2)$$

The expected slope for the graph E vs $\log [\text{Mg}^{2+}]$ was observed as shown in Figure 3.3.

Agreement between the empirical and theoretical values provides support for the electrode's correct thermodynamic behavior.



A second requirement for a suitable reference is chemical stability in the electrolytic medium. This requirement was particularly difficult due to the reactivity of the amalgam with many common electrolyte solvents. The amalgam reacts with water, propylene carbonate, and acetonitrile resulting in the depletion of Mg and a shift in its potential. No reaction was observed with anhydrous DMF and its choice by Brown and McIntyre (5) as a suitable solvent is confirmed in the present work. Equilibrium potential measurements of $\text{Mg(Hg)/Mg}_x\text{U}_3\text{O}_8$ and $\text{Mg(Hg)/Mg}_x\text{UO}_{2.9}$ cells at room temperature (see Chapter 4) showed a drift of only ± 2 mV over periods as long as 2 weeks. Where larger voltage drifts were

observed it was found that $\text{Mg}(\text{OH})_2$ had formed on the amalgam surface as a result of contamination with water.

In order to calculate thermodynamic quantities for magnesium insertion from cell voltages the potential of $\text{Mg}(\text{Hg})$ versus Mg must be known. The following equation derived from the work of Mussini et al. (6,7,8) on dilute magnesium amalgams in water in a system which provides for continual renewal of the electrode surface gives the potential of the cell $\text{Mg}/\text{Mg}(\text{ClO}_4)_2(\text{aq})/\text{Mg}(\text{Hg})$ as

$$E_{298\text{K}} = 0.395 - 0.668x_{\text{Mg}} - 0.0296\log x_{\text{Mg}} \quad (3.3)$$

where x_{Mg} equals the mole fraction of magnesium in the amalgam. Although measured in water, the cell potential is independent of the solvent and was calculated to be +0.460 V for the electrode used here. Therefore, to all open-circuit voltages was added +0.460 V to obtain the equilibrium potential of the cell $\text{Mg}/\text{Mg}(\text{ClO}_4)_2(\text{DMF})/\text{Mg}_x\text{UO}_n$. The error for not working at exactly 298 K is estimated to be less than 3 mV.

Figure 3.4 shows the four-compartment cell used for the electrochemical insertion of magnesium. The magnesium amalgam is contained within a Pyrex tube which is sealed at one end with a fine porosity glass frit. This reference electrode is connected to the cell through a Luggin capillary positioned approximately 3 mm from the working electrode surface. The counter electrode, consisting of 1 mm magnesium wire (Foote, 99.9%), is placed inside its own compartment separated from the working electrode by a fine porosity glass frit. Stainless steel rods provide the electrical connections to the working and counter electrodes while platinum wire is used for connection to the reference electrode. Approximately 15 ml of 0.5 M $\text{Mg}(\text{ClO}_4)_2$ in DMF were required during testing which was performed in an argon filled glove box.

3.2 ELEVATED TEMPERATURE CELL

Like magnesium, sodium is unstable in all organic solvents and is unsuitable as a reference electrode for thermodynamic measurements. Sodium amalgam was found in this work to be highly reactive as well. It was therefore necessary to isolate the sodium from the electrolyte using the sodium ion conducting ceramic β "-alumina. Beta"-alumina can be considered a substituted spinel $\text{Na}_{1-x}\text{Li}_{x(1-z)}\text{Mg}_{2xz}\text{Al}_{5-xz}\text{O}_8$ in which Mg^{2+} and/or Li^+ stabilize

the β'' -phase against decomposition to the less conductive β -phase (9). The high ionic resistance of β'' -alumina requires it be heated to about 150°C to achieve acceptable conductivity. Since typical cell solvents (e.g. tetrahydrofuran, dimethoxyethane, DMSO) can tolerate only small excursions above ambient temperature, alternative solvents had to be evaluated for their suitability.

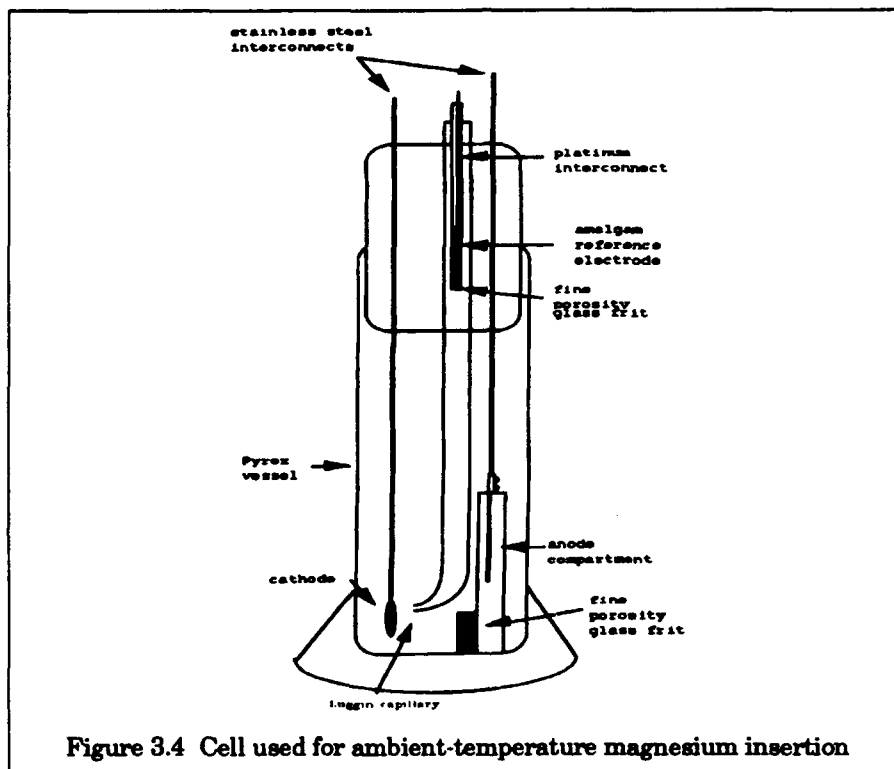


Figure 3.4 Cell used for ambient-temperature magnesium insertion

Solvent selection presented a challenge due to the relatively high operating temperature. According to Matsuda (10), a battery electrolyte must have a high relative dielectric constant, a low viscosity, a high boiling point, and a low melting point. Unfortunately, no single electrolyte solvent possesses all of these characteristics over the temperature range of study. Propylene carbonate appeared to be ideal with a liquidus range of -49.2 - 241.7°C, a low viscosity of 2.53 cP, and a relative dielectric constant of 64.4. However, it decomposes above 80°C, making it unsuitable for elevated temperature measurements.

Two organic electrolytes based on sulfur were looked at next. The first, sulfolane, looked very attractive as can be seen from its physical properties at 30°C (11):

melting point - 28.45°C
boiling and decomposition point - 285°C
density - 1.2625 g/ml
dynamic viscosity - 102.9 cP
relative dielectric constant - 43.3

The melting point is lowered below room temperature upon addition of the electrolyte salt, although the viscosity remains high and conductivity low. Sulfolane is also chemically and electrochemically stable towards lithium (10). Given that it met all the requirements for operation in the temperature range of interest, sulfolane was examined as a possible solvent for this portion of the study.

Commercial sulfolane is slightly acidic and contains the impurity 3-sulfolene. The acidity presents a problem for lithium while the 3-sulfolene thermally decomposes above 100°C. Following the purification method of Coetzee (11), 250 ml of sulfolane (Aldrich) and 3 g of crushed NaOH (BDH) were continuously stirred in a fume hood at a temperature of 170 - 180°C for 24 hours while bubbling N₂ through the mixture. Flowing nitrogen is essential in removing sulfur dioxide and butadiene, the decomposition products of 3-sulfolene. The reddish-brown liquid was then mixed with 3 g of decolorizing charcoal and stirred for 6 hours at a temperature of 30°C. The mixture was filtered through a number 3 glass frit and the filtrate vacuum distilled at 110°C over type 3A molecular sieve.

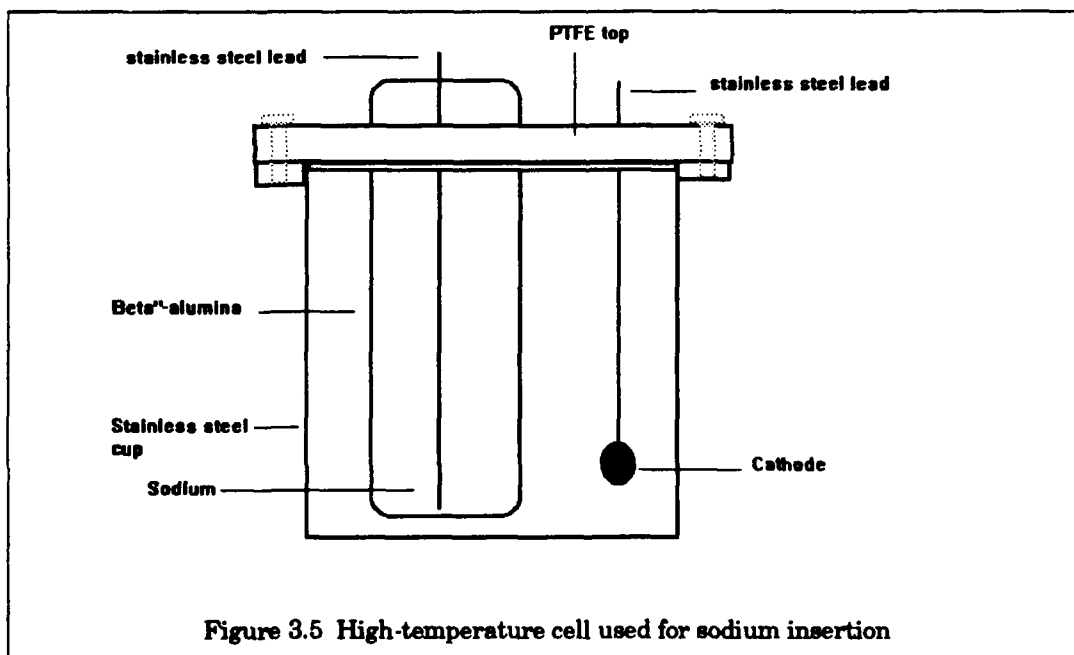
The purified sulfolane proved to be an unsuitable solvent as it decomposed and turned dark brown in color within 24 hours at 150°C. The above purification was repeated several times with the same end result. It was concluded that sulfolane is suitable as a high-temperature solvent for only short periods.

A second promising high-temperature solvent used in testing was dimethylsulfone (DMSO₂). Like sulfolane, it readily dissolves inorganic salts, is chemically unreactive, and has good high-temperature stability. Being a solid at room-temperature, it is easily purified by recrystallization. It melts at 109°C and boils at 240°C (12). Tremillon and co-workers (13,14) and Pereira-Ramos (12,15-20) have done extensive testing of alkali- and alkaline-earth metal insertion into transition-metal oxides using DMSO₂ at 150°C. They have found it has excellent thermal and chemical stability at elevated temperatures for extended periods. DMSO₂ also has a weak solvation effect upon ions, and cations in particular. The

absence of a large solvation sphere around the guest ion enables insertion to occur unencumbered. In terms of conductivity, the value for 1 m LiClO_4 in DMSO_2 at 150°C is about 10 times greater than a propylene carbonate solution of the same concentration at ambient temperature.

Dimethylsulfone (Aldrich) was purified following the method of Pereira-Ramos (12) by recrystallizing it once from water and twice from anhydrous methanol (Aldrich). The white crystals were air dried at 90°C for at least 48 hours and then dried in a vacuum desiccator at 30°C for at least 12 hours. Water concentration under these conditions did not exceed 0.005 mole/kg (21). Purified DMSO_2 remained stable indefinitely at 150°C and was therefore chosen as the solvent for elevated temperature use.

The cell developed for sodium insertion at elevated temperatures appears in Figure 3.5. The β "-alumina is manufactured by Chloride Silent Power Limited. The ceramic tube serves a secondary purpose in keeping the liquid sodium (Aldrich, 99.9%) anode from reacting with the 0.1 m $\text{DMSO}_2/\text{NaClO}_4$ electrolyte. The lower portion of the cell was placed in a vertical tube furnace which was controlled by a Fuji model PYZ microcontroller with solid-state relay to within $\pm 1^\circ\text{C}$. The entire apparatus was contained within an argon filled glove box.



REFERENCES

1. G. J. Reynolds, D.Phil. Thesis, Oxford University, (1981).
2. J. Farrer, R. Keller, and M. M. Nicholson, Rocketdyne North American Aviation Inc., High Energy Battery Systems, Final Report, DA-28-043 AM (3-01394E), 1963.
3. W. E. Elliott, J. R. Huff, R. W. Adler, and W. L. Towle, *Proc. 20th Annual Power Sources Conf.*, p. 67 (1966).
4. O. R. Brown and R. McIntyre, *Electrochim. Acta*, **30**, 627, (1985).
5. O. R. Brown and R. McIntyre, *Electrochim. Acta*, **29**, 995, (1984).
6. P. Longhi, T. Mussini, and C. Osmani, *Chim. Ind.*, **55**, 11, 88, (1973).
7. S. Ardizzone, P. Longhi, T. Mussini, and S. Rondinini, *Ann. Chim.*, **65**, 753, (1975).
8. T. Mussini, P. Longhi, and S. Rondinini, *Ann. Chim.*, **73**, 357, (1983).
9. S. N. Heavens, *British Ceramic Proceedings*, **38**, 119, (1986).
10. Y. Matsuda, *J. Power Sources*, **20**, 19, (1987).
11. J. F. Coetzee, J. M. Simon, and R. J. Bertozzi, *Anal. Chem.*, **41**, 6, 766, (1969).
12. J. P. Pereira-Ramos, R. Messina, and J. Perichon, *J. App. Electrochem.*, **16**, 379, (1986).
13. B. Bry and B. Tremillon, *J. Electroanal. Chem.*, **30**, 457, (1971).
14. M. Machtinger, M. J. Vuaille, and B. Tremillon, *J. Electroanal. Chem.*, **83**, 273, (1977).
15. J. P. Pereira-Ramos, R. Messina, and J. Perichon, *J. Electroanal. Chem.*, **218**, 241, (1987).
16. J. P. Pereira-Ramos, R. Messina, C. Piolet, and J. Devynck, *J. Power Sources*, **20**, 221, (1987).
17. J. P. Pereira-Ramos, R. Messina, and J. Perichon, *J. Electrochem. Soc.*, **135**, 12, 3050, (1988).
18. J. P. Pereira-Ramos, R. Messina, and J. Perichon, *Sol. State Ion.*, **40/41**, 974, (1990).
19. J. P. Pereira-Ramos, R. Messina, and J. Perichon, *J. Power Sources*, **16**, 193, (1985).
20. J. P. Pereira-Ramos, R. Messina, C. Piolet, and J. Devynck, *Electrochim. Acta*, **33**, 7, 1003, (1988).
21. C. Auerbach and D. K. McGuire, *J. Inorg. Nucl. Chem.*, **28**, 2659, (1966).

CHAPTER 4 CHRONOPOTENTIOMETRIC STUDY OF CATION INSERTION

This chapter discusses the use of chronopotentiometry to obtain phase, thermodynamic, and kinetic information pertaining to the insertion of sodium, magnesium, and zinc into polymorphs of uranium oxide.

4.1 THEORY

Chronopotentiometry is a convenient electrochemical technique for making and studying insertion compounds. In a chronopotentiometry experiment the current flowing in a cell is instantaneously stepped from zero to some value, thereby fixing the reaction rate. Potential is monitored with time which can be equated to the extent of insertion, termed the x -value, using Faraday's law (1,2). Figures 1.6 and 1.10 in Chapter 1 are two examples of chronopotentiometric discharge curves. Analysis of these curves provides valuable information about the phases present as insertion occurs. Interruption of current flow at various x -values allows the cell potential to relax to its equilibrium value which can be used to calculate thermodynamic quantities. Departure from equilibrium under constant or pulsed current flow provides the opportunity to gather kinetic data about the insertion process using several available models.

4.1.1 THERMODYNAMIC STUDIES

The energies of formation of oxide insertion compounds can be determined by two principal and complementary methods; calorimetric and electrochemical. In the calorimetric approach, the enthalpy change ΔH_{ins} for the reaction



is indirectly measured using a thermochemical cycle of intermediate reactions. This quantity, combined with standard enthalpy data, enables $\Delta H_f^\circ[A_xMO_n(s)]$ to be determined.

In the electrochemical method, open-circuit voltages $E(x)$ are measured for cells of the type $A(s)/A^+(soln)/MO_n(s)$, x -values being obtained by coulometric titration. In a single phase region of solid-solution formation, $A \leftrightarrow A(soln \text{ in } A_xMO_n)$ and the thermodynamic

Chapter 4 Chronopotentiometric Study

quantity measured, $\Delta\bar{G}_A$, is the partial molar free energy of solution, which is related to $E(x)$ by $\Delta\bar{G}_A = -zEF$. For a range of x -values where two solid phases of fixed compositions A_xMO_n and A_yMO_n co-exist and are in equilibrium by the reaction



E is constant and $\Delta\bar{G}_A = -zFE$.

For the reaction



the corresponding integral free energy change is given by the Gibbs-Duhem equation

$$\Delta G_x = -zF \int_0^x E(x) dx \quad (4.4)$$

The related integral entropy change ΔS_x is given by

$$\Delta S_x = zF \int_0^x \partial E(x) / \partial T dx \quad (4.5)$$

and its evaluation by electrochemical means alone requires accurate measurement of the cell's EMF temperature coefficient. Alternatively, ΔS_x can be derived from a combination of electrochemical and calorimetric measurements through the relation (3,4,5)

$$\Delta G_x = \Delta H_x - T\Delta S_x \quad (4.6)$$

4.1.2 KINETIC STUDIES

4.1.2.1 Kinetic Properties of Solids

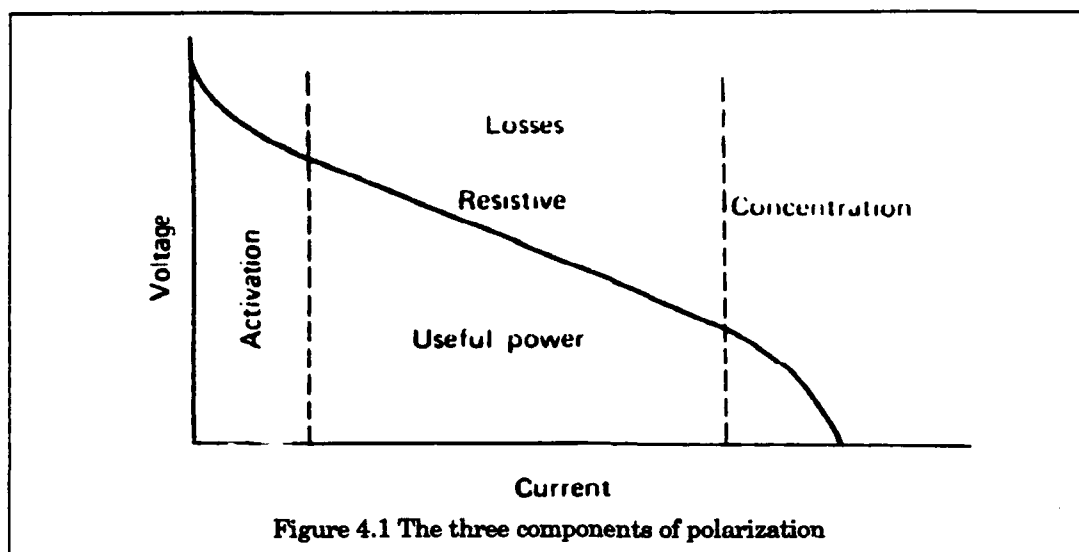
Thermodynamic laws govern the behavior of electrochemical cells during equilibrium, but it is kinetics which dictate their behavior when current is passed. Movement of charged species determines the amount of current a cell is capable of sustaining at a particular voltage. Regretfully, a cell is never able to maintain its equilibrium potential due to the generation of forces opposing the passage of current. These forces manifest themselves in what is referred to as polarization or overpotential. This voltage loss, as seen in Figure 4.1, is a function of current density and consists of three separate terms:

η_a = activation overpotential (charge-transfer limiting)

η_c = concentration overpotential (mass-transfer limiting)

η_o = Ohmic overpotential.

In this study, only η_a and η_c are of interest.



Activation polarization is a measure of the ease of charge transfer between different phases (6). In classic, solution electrochemistry, the transfer is between metal ions (M^{n+}) in the solid and solution phases.



The rates at which the forward (f) and reverse (r) reactions occur can be described using transition-state theory, with the appropriate equations being:

$$\text{rate}_f = k_1 a_1 \exp[-\Delta G_f/RT] \quad (4.8)$$

$$\text{rate}_r = k_2 a_2 \exp[-\Delta G_r/RT] \quad (4.9)$$

As expected, the rate of charge transfer is directly proportional to the value of the rate constant (k) and the activation free energy (ΔG).

A different case exists for charge transfer within the insertion electrode itself where it is assumed that only two mobile species, one ionic and one electronic, exist. Electrons must travel through the solid, active material in order for reduction to occur. The concern now is not with the ionic conductivity of the electrolyte, but with the electrical and ionic conductivity of the electrode.

Concentration polarization is due to the mass transport limitations of the ions. Ionic movement is caused by any of a combination of electrical, gravitational, and concentration gradients present in the system. Given that convective transport within a phase is minimal, the total current density (i) for a given species (designated n) is given by (7):

$$i_n = i_{\text{migr}} + i_{\text{diff}} = -\sigma_n(\partial\phi/\partial x) - z_n q D_n (\partial \ln a_n / \partial \ln c_n) (\partial c_n / \partial x) \quad (4.10)$$

where i_{migr} = contribution to current from migration
 i_{diff} = contribution to current from diffusion
 σ_n = specific electrical conductivity of species n
 ϕ = electrostatic potential
 x = directional component
 z_n = charge number
 q = elementary charge
 D_n = self diffusion coefficient
 a_n = activity
 c_n = concentration

The first term on the right hand side is the same as Ohm's law for the migration of species n in the presence of an internal electrostatic field. The second term is related to Ficks' first law of diffusion

$$J_n = -D(\partial C_n / \partial x) \quad (4.11)$$

where J_n is the flux for species n under a concentration gradient and D is the chemical diffusion coefficient.

In battery electrolytes, the solution phase is characterized by a very large concentration of mobile ions; thus, concentration gradients must be small and ion transport occurs predominantly through migration. Equation 4.10 can then be simplified to

$$i_n = -\sigma_n(\partial\phi/\partial x). \quad (4.12)$$

The situation is reversed, however, for the electrode phase where charge transport takes place via the motion of electronic species. Internal electric fields are small, and therefore ionic flux is due mainly to a local ionic concentration gradient within the solid phase. Equation 4.10 can again be simplified by neglecting the first term on the right hand side and assuming $t_{e-} = 1$:

$$i_n = -z_n q D_n (\partial \ln a_n / \partial \ln c_n) (\partial c_n / \partial x). \quad (4.13)$$

The term $\partial \ln a_n / \partial \ln c_n$ is the thermodynamic enhancement factor (W) which relates the chemical diffusion coefficient (D) to the self diffusion coefficient (D_n) in the expression

$$D = W D_n. \quad (4.14)$$

W can be quite large (8-12) and is responsible for explaining ionic flux density values above those solely predicted by a concentration gradient. It is empirically accessible from the equation (7)

$$W = -[(z_n x F / RT) \cdot dE/dx] \quad (4.15)$$

where x is the extent of insertion (i.e. x -value) and dE/dx is the slope of the equilibrium discharge curve at the x -value. The greatest enhancement in ionic motion will therefore occur in regions where the discharge curve slopes greatly. dE/dx can also be used to calculate the partial ionic conductivity (σ_n) (13)

$$\sigma_n = -z_n F (D_n / V_m) dx/dE. \quad (4.16)$$

4.1.2.2 Electrochemical Techniques for Determining Kinetic Properties of Solids

A number of different electrochemical techniques are available for studying the kinetic properties of insertion compounds (8,14-24). As Weppner and Huggins (24) point out, an important advantage of most of these techniques is the simultaneous measurement of thermodynamic and kinetic quantities from cell voltage and current. Previous work by Reynolds (25) on the kinetics of lithium insertion into MoO_3 compared the techniques of Weppner and Huggins (8) and Basu and Worrell (17) and found them both to produce results comparable to those from NMR measurements. However, the method of Basu and Worrell is independent of IR polarization, and it therefore was selected for use in the present work.

In the technique, a negligible amount of guest ion is introduced into the host from a constant current pulse. The recovery rate of the cell voltage to its previous equilibrium value is controlled by the guest ion's diffusion rate into the bulk cathode. Crank (26) gives Fick's second law for an instantaneous source or sink of diffusing species in semi-infinite geometry as

$$c - c_0 = \{i\tau/[AF(\pi Dt)^{1/2}]\} \exp(-a^2/4Dt) \quad (4.17)$$

where c = concentration of diffusing species
 c_0 = initial uniform concentration of the species
 A = area
 i = current pulse
 τ = pulse duration
 a = distance from the planar source
 D = chemical diffusion coefficient
 t = time after conclusion of current pulse

The concentration terms may be replaced by voltage and noting that $c = x/V_m$ where V_m is the molar volume, equation 4.17 becomes when $a = 0$

$$E - E_0 = \Delta E = [V_m i \tau (dE/dx)] / [FA(\pi Dt)^{1/2}] \quad (4.18)$$

Chapter 4 Chronopotentiometric Study

where E = voltage at time t

E_0 = initial equilibrium voltage.

A plot of ΔE vs. $t^{-1/2}$, such as the one for $Mg_xU_3O_8$ shown in Figure 4.2, should be linear and

D may be calculated from the slope. The initial curvature is attributed to electrolyte effects

(17).

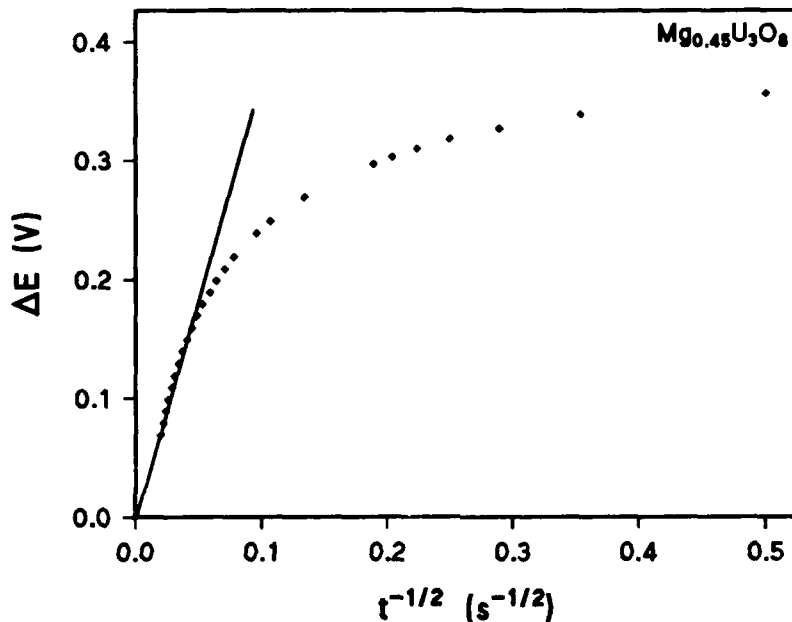


Figure 4.2 Current pulse measurement for $Mg_{0.45}U_3O_8$

4.2 APPARATUS

The cells used for insertion reactions were described in Chapter 3. Measurements were made using a microprocessor-controlled cell tester designed and built by the Electronic Services Department of the ICL. The unit consisted of a Rade Z80 microprocessor controlling 8 solid-state constant current sources. A total of 8 cells can be tested simultaneously in a Vacuum Atmospheres model DL001 glove box.

4.3 GALVANOMETRIC MEASUREMENTS

4.3.1 AMBIENT-TEMPERATURE INSERTION

4.3.1.1 Sodium

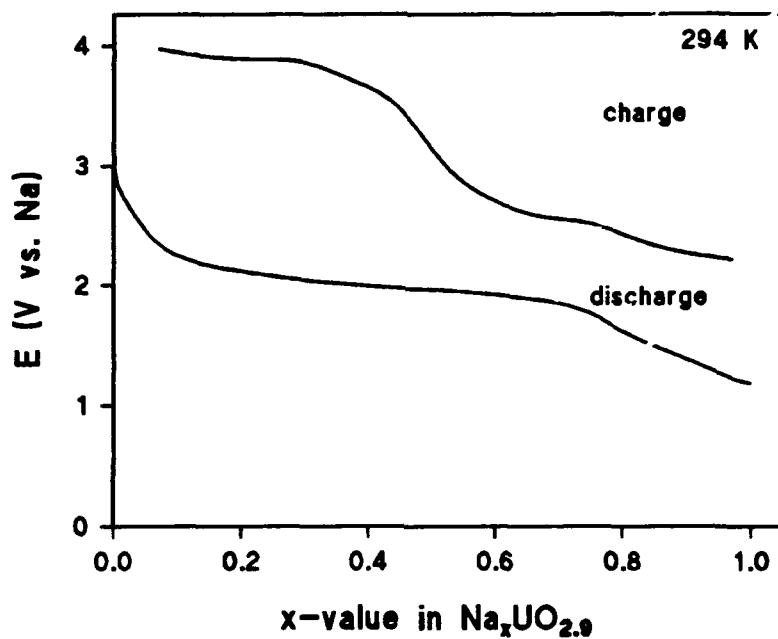
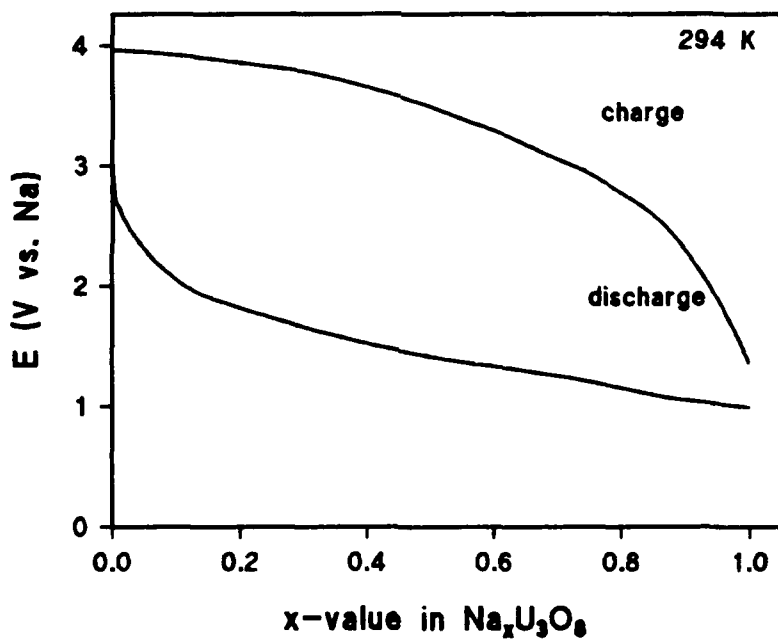
Figures 4.3 to 4.6 show the discharge and charge curves for cells containing sodium. All cells exhibit high polarization attributed to the relatively large size of Na^+ ($r = 0.95 \text{ \AA}$) which hinders its insertion (27). Differences in the shapes of the discharge and charge curves suggests sodium insertion is only partially reversible to $x = 1$.

The slope of the discharge curves of $\delta\text{-UO}_3$, $\gamma\text{-UO}_3$, and U_3O_8 indicates solid-solution formation for $x < 1$. Powder X-ray diffraction patterns of discharge products at $x \approx 1$ showed a single phase present for NaU_3O_8 , while $\delta\text{-NaUO}_3$ and $\gamma\text{-NaUO}_3$ were poorly crystalline. The results are consistent with the study of chemically prepared $\text{Na}_{1.29}\text{U}_3\text{O}_8$ which also reported a single phase (28). Two interstitial sites are available in U_3O_8 with the nine-coordinate site being favored for sodium insertion (29).

$\text{UO}_{2.9}$ displays a plateau in the range $0.15 < x < 0.75$ which suggests the existence of two phases in this region. The powder X-ray diffraction pattern of chemically prepared $\text{Na}_{0.35}\text{UO}_{2.95}$ showed two phases isostructural with the parent oxide. Possible sites for sodium occupation include the nine coordinate and those of the vacated uranium atoms.

A two-phase region exists for UTiO_5 at $0.04 < x < 0.58$ which is consistent with the single phase observed by Woodall (30) at the composition $\text{Na}_{0.6}\text{UTiO}_5$ for the chemically prepared compound.

Of the cell products discharged to $x = 1$, $\text{UO}_{2.9}$ and U_3O_8 showed a small increase in the interlayer spacing along the c-axis (Table 4.1) while X-ray diffraction patterns for $\delta\text{-UO}_3$, $\gamma\text{-UO}_3$, and UTiO_5 were too poorly crystalline for refinement. X-ray diffraction patterns of UTiO_5 , $\text{Na}_{0.6}\text{UTiO}_5$, and NaUTiO_5 in Figure 4.7 clearly show the destruction of the crystal structure as insertion progresses, which presumably is attributable to sodium's relatively large size.

Figure 4.3 $\text{UO}_{2.9}$ at 25 μA in 0.4 M NaClO_4 /propylene carbonate at 294 KFigure 4.4 U_3O_8 at 25 μA in 0.4 M NaClO_4 /propylene carbonate at 294 K

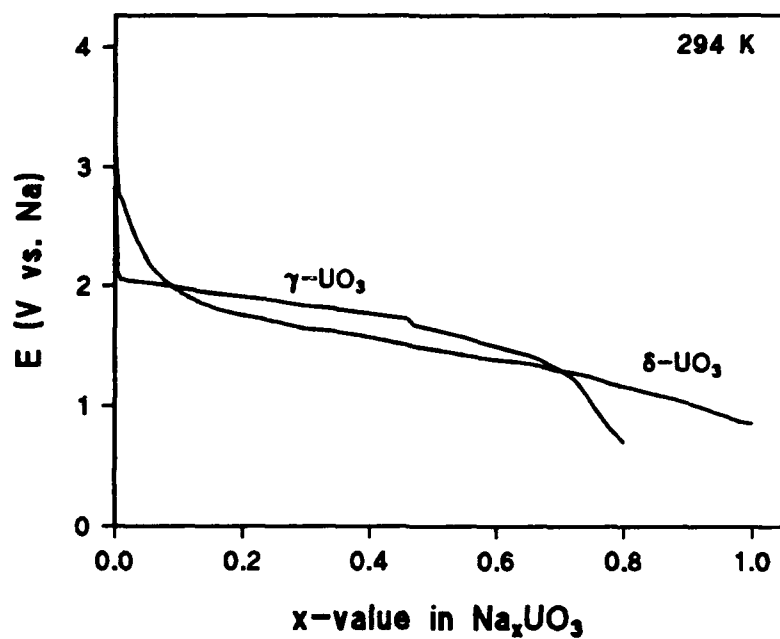


Figure 4.5 $\delta\text{-UO}_3$ and $\gamma\text{-UO}_3$ at 25 μA in 0.4 M NaClO_4 /propylene carbonate at 294 K

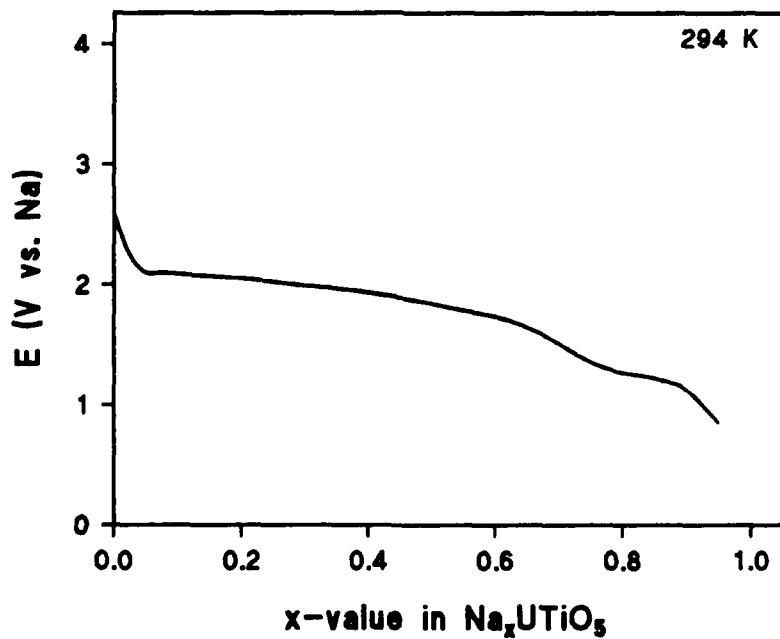


Figure 4.6 UTiO_5 at 25 μA in 0.4 M NaClO_4 /propylene carbonate at 294 K

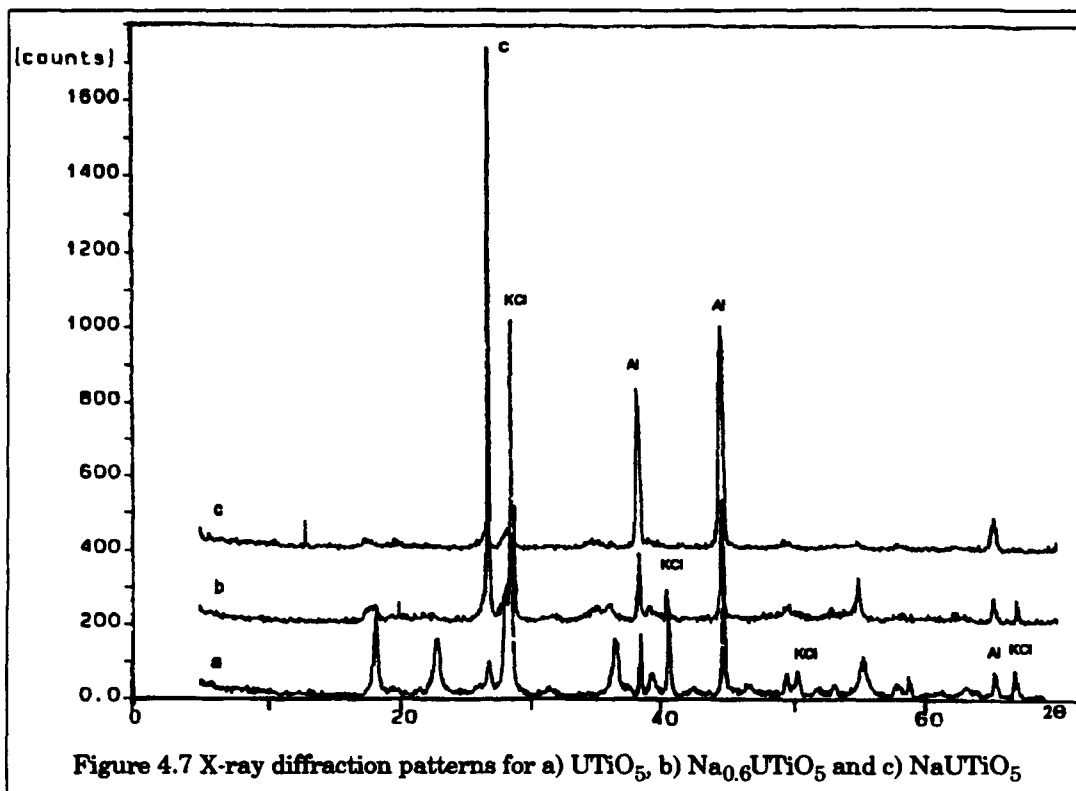


Figure 4.7 X-ray diffraction patterns for a) UTiO_5 , b) $\text{Na}_{0.6}\text{UTiO}_5$ and c) NaUTiO_5

4.3.1.2 Magnesium

Discharge-charge curves and open-circuit potentials for magnesium cells are displayed in Figures 4.8 - 4.11. High polarization is again observed; however, the +2 charge and not the size of Mg^{2+} ($r = 0.65 \text{ \AA}$) is believed to be the cause. Insertion into $\delta\text{-UO}_3$ and $\gamma\text{-UO}_3$ occurs to a minor extent while $\text{UO}_{2.9}$, U_3O_8 , and UTiO_5 form two phases in the ranges $0.07 < x < 0.27$, $0.05 < x < 0.40$, and $0.03 < x < 0.31$ respectively. Calculations performed by Ball (31) predict that magnesium occupies the same nine-coordinate sites as sodium.

The interlayer spacing showed little change upon insertion to low x -values (Table 4.1). In U_3O_8 cells discharged beyond $x \approx 0.5$ two additional peaks appeared in the X-ray pattern at $2\theta = 28.385^\circ$ and 32.888° . These peaks match those of a f.c.c unit cell with $a = 5.42 \text{ \AA}$. Kemmler-Sack and Rudorff (32) previously made a high-temperature fluorite phase with the general formula $\text{Mg}_y\text{U}_{1-y}\text{O}_2$ by reacting MgUO_4 and UO_2 . The unit-cell dimension for this phase for $0 \leq y \leq 0.33$ ranges from 5.468 \AA to 5.275 \AA . Inclusion of the unit-cell dimension of the electrochemically prepared compound within this range suggests the formation of a solid solution up to $x \approx 0.5$ with the formation of a fluorite phase of a composition $\text{Mg}_y\text{U}_{1-y}\text{O}_2$ at greater x -values.

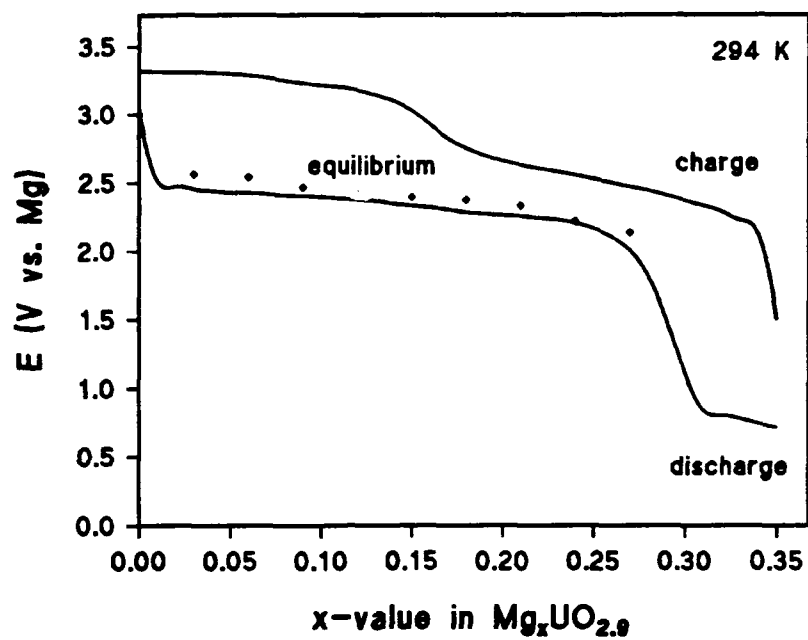
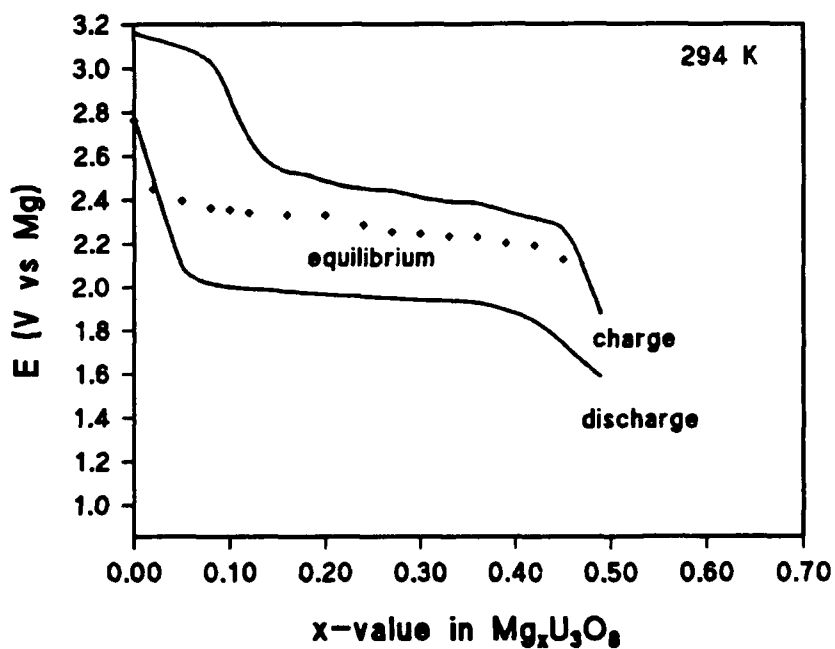
The current was reversed in cells containing $\text{UO}_{2.9}$, U_3O_8 , and UTiO_5 to determine the reversibility of magnesium insertion. From the dissimilar shapes of the charge and discharge curves, the redox process is only partially reversible. Similar behavior was observed by Pereira-Ramos et al. (33) for $\text{Mg}_x\text{V}_2\text{O}_5$.

4.3.1.3 Zinc

Given its +2 valency and proximity in size to magnesium, zinc ($r = 0.74 \text{ \AA}$) insertion was expected to mimic the alkaline-earth metals. Figures 4.12 to 4.14 show this to be the case with the characteristic high polarization, low x -value, and irreversible behavior. U_3O_8 forms a solid solution with zinc for $x < 0.2$ while $\text{UO}_{2.9}$ and UTiO_5 each form two phases with zinc in the range $0.03 < x < 0.15$. As with magnesium, little change occurred in the interlayer spacing upon insertion (Table 4.1).

Table 4.1 c-lattice parameters of electrochemically prepared insertion compounds

Compound	$c(\text{\AA})$
$\text{UO}_{2.90}$	4.172(9)
$\text{Mg}_{0.28}\text{UO}_{2.90}$	4.149(2)
$\text{Zn}_{0.20}\text{UO}_{2.90}$	4.129(2)
$^1\text{Na}_{1.00}\text{UO}_{2.90}$	4.253(5)
$^2\text{Na}_{1.00}\text{UO}_{2.90}$	4.262(2)
U_3O_8	4.138(2)
$\text{Mg}_{0.62}\text{U}_3\text{O}_8$	4.139(1)
$\text{Zn}_{0.20}\text{U}_3\text{O}_8$	4.128(7)
$^1\text{Na}_{1.00}\text{U}_3\text{O}_8$	4.186(3)
$^2\text{Na}_{1.00}\text{U}_3\text{O}_8$	4.193(6)
UTiO_5	15.628(32)
$\text{Mg}_{0.30}\text{UTiO}_5$	15.489(21)
$\text{Zn}_{0.30}\text{UTiO}_5$	15.490(35)
1294 K	
2423 K	

Figure 4.8 $\text{UO}_{2.9}$ at 25 μA in 0.5 M $\text{Mg}(\text{ClO}_4)_2/\text{DMF}$ at 294 KFigure 4.9 U_3O_8 at 25 μA in 0.5 M $\text{Mg}(\text{ClO}_4)_2/\text{DMF}$ at 294 K

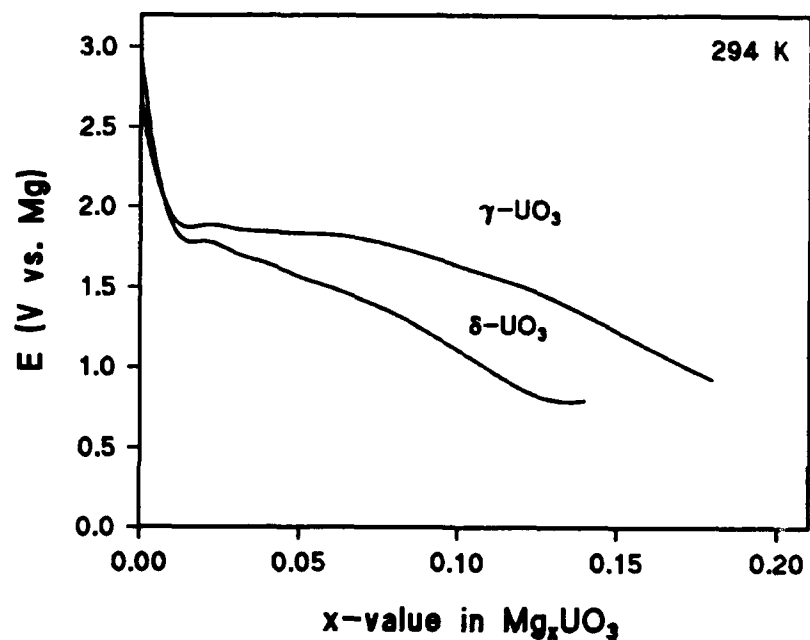


Figure 4.10 $\delta-UO_3$ and $\gamma-UO_3$ at 25 μA in 0.5 M $Mg(ClO_4)_2/DMF$ at 294 K

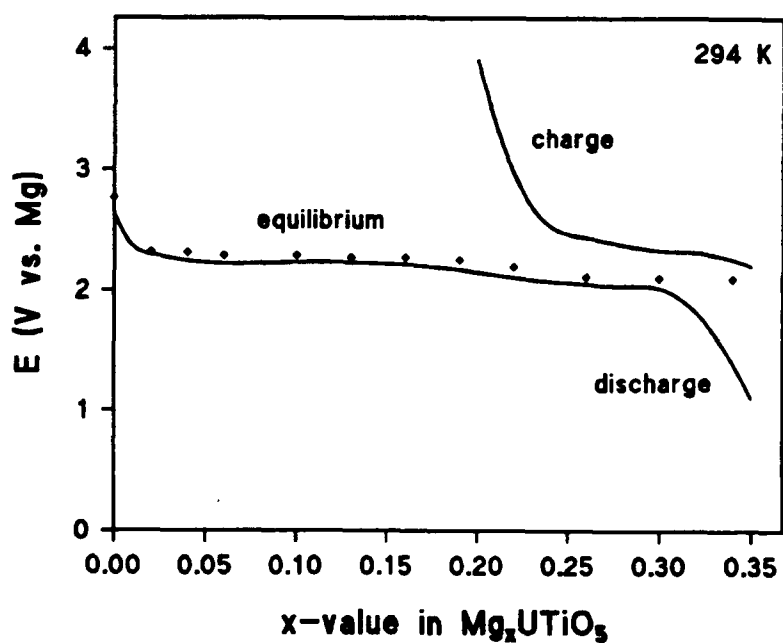


Figure 4.11 $UTiO_5$ at 25 μA in 0.5 M $Mg(ClO_4)_2/DMF$ at 294 K

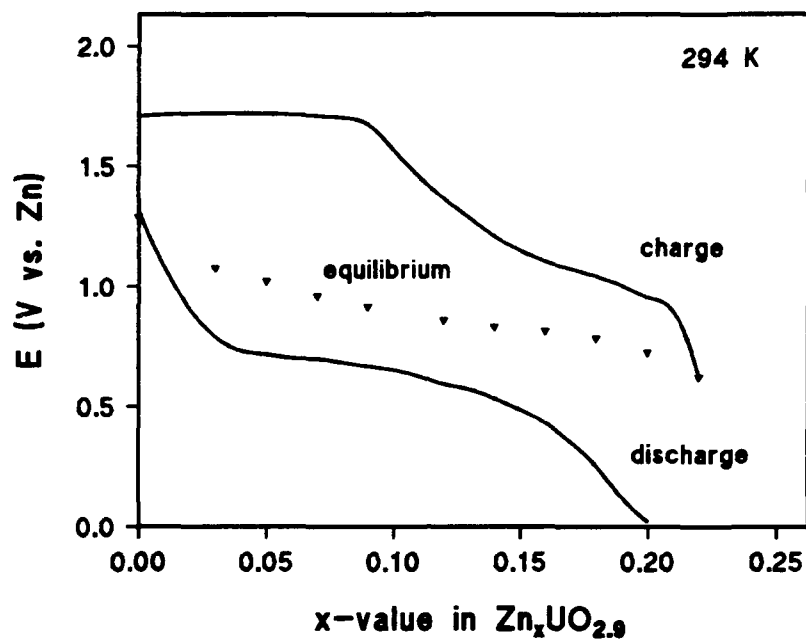


Figure 4.12 $\text{UO}_{2.9}$ at 25 μA in 0.2 M zinc triflate/propylene carbonate, DMSO at 294 K

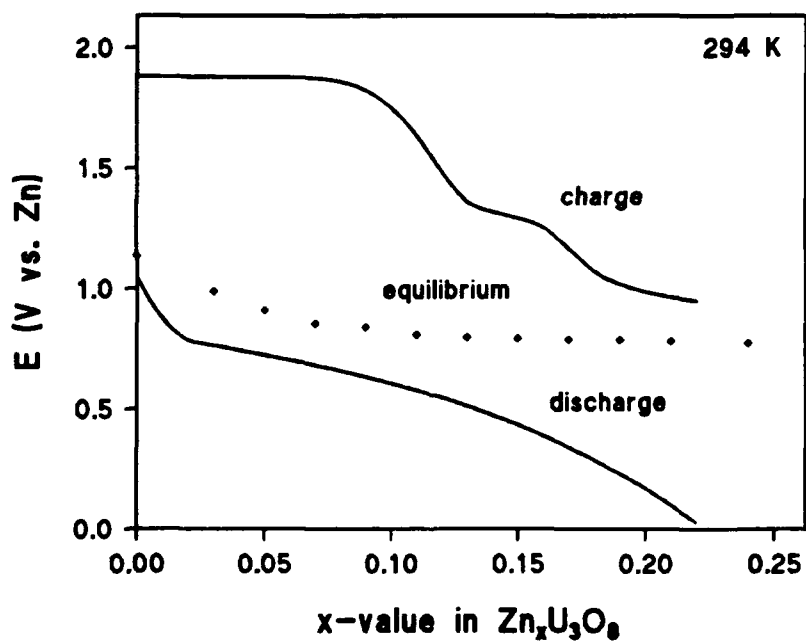


Figure 4.13 U_3O_8 at 25 μA in 0.2 M zinc triflate/propylene carbonate, DMSO at 294 K

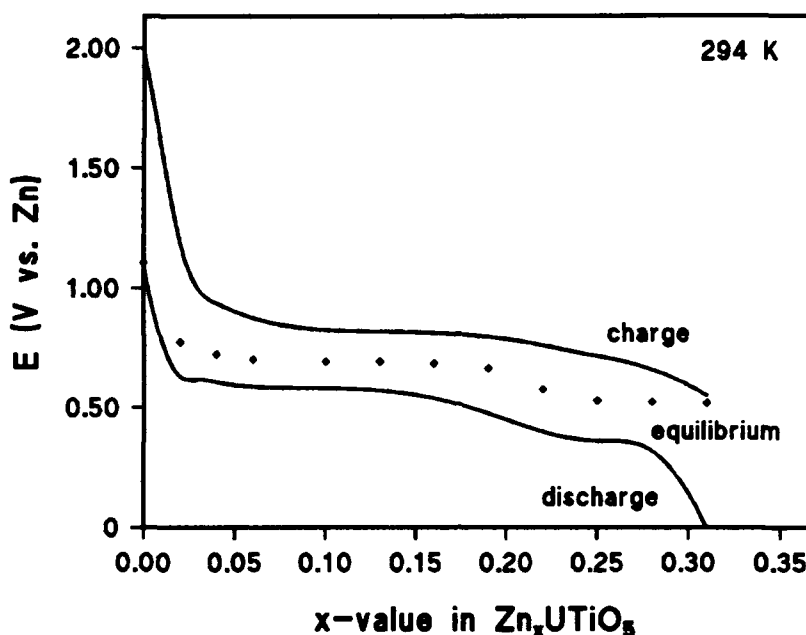


Figure 4.14 UTiO_5 at $25 \mu\text{A}$ in 0.2 M zinc triflate/propylene carbonate, DMSO at 294 K

4.3.2 ELEVATED TEMPERATURE

The discharge curves and open-circuit potentials for sodium insertion at 150°C (Figures 4.15 - 4.17) are very similar to those at ambient temperature. Polarization is again high, but less than that at ambient temperature which is attributed to better kinetics at 150°C . As before at ambient temperature, the c-lattice parameter shows a small increase with sodium insertion for $\text{UO}_{2.9}$ and U_3O_8 while UTiO_5 becomes nearly amorphous.

4.4 THERMODYNAMIC MEASUREMENTS

The integral free energy of insertion (ΔG_x) is plotted against x-value in Figures 4.18 - 4.20 and tabulated in Table 4.2 for sodium, magnesium, and zinc insertion into $\text{UO}_{2.9}$, U_3O_8 , and UTiO_5 . Calorimetric values for ΔH_x (34) are shown as separate data points for several compounds. The close agreement between ΔG_x and ΔH_x reinforces the conclusion already arrived at for other metal oxide insertion compounds (35,36) that the corresponding values of the entropies of insertion are small. Errors of measurement precluded any quantitative assessment of changes in this quantity as a function of structure.

Thermodynamic quantities for a number of metal oxide insertion compounds are listed in Table 4.3. Assuming the A-O site binding energy varies little between the host metal oxides for a given inserted element (3), the dominant factors in determining the energetics of insertion would appear to be the ease of reduction of the metal within the host and the electrostatic repulsion between the inserted ions which increases with insertion.

Table 4.2 Values for integral free energy of insertion

Compound	x-value	$-\Delta G_x$ (kJ mol ⁻¹)	Compound	x-value	$-\Delta G_x$ (kJ mol ⁻¹)
$\text{Na}_x\text{UO}_{2.9}$	0.03	9.4	$\text{Mg}_x\text{UO}_{2.9}$	0.03	14.9
	0.08	24.6		0.06	29.7
	0.15	45.3		0.09	44.2
	0.25	74.1		0.12	58.3
	0.35	102.8		0.15	72.3
	0.45	131.3		0.18	86.1
$\text{Zn}_x\text{UO}_{2.9}$	0.55	159.7	$\text{Na}_x\text{U}_3\text{O}_8$	0.21	99.7
	0.03	6.9		0.24	112.9
	0.05	10.9		0.27	125.5
	0.07	14.7		0.05	14.3
	0.09	18.4		0.20	57.0
	0.12	23.5		0.30	85.3
$\text{Zn}_x\text{U}_3\text{O}_8$	0.14	26.8	$\text{Mg}_x\text{U}_3\text{O}_8$	0.40	112.6
	0.16	29.9		0.02	10.1
	0.18	33.0		0.05	24.3
	0.20	35.9		0.08	38.0
	0.22	38.5		0.10	47.1
	0.03	6.1		0.12	56.2
Mg_xUTiO_5	0.05	9.8	Zn_xUTiO_5	0.16	74.2
	0.07	13.2		0.20	92.2
	0.09	16.5		0.24	110.0
	0.11	19.6		0.27	123.1
	0.13	22.7		0.30	136.1
	0.15	25.8		0.33	149.1
	0.17	28.8		0.36	162.0
	0.19	31.9		0.39	174.7
	0.21	34.9		0.42	187.5
	0.24	39.4		0.45	200.0
	0.27	43.8		0.60	260.4
	0.30	48.2		0.65	280.0
Mg_xUTiO_5	0.02	9.8		0.02	3.6
	0.04	18.7		0.04	6.5
	0.06	27.6		0.07	10.6
	0.10	45.2		0.10	14.7
	0.13	58.4		0.13	18.7
	0.16	71.5		0.16	22.6
	0.19	84.6		0.19	26.6
	0.22	97.4		0.22	30.1
	0.26	114.0		0.25	33.3
	0.30	130.3		0.28	36.4
	0.34	146.5		0.31	39.4

Table 4.3 Enthalpies and free energies of insertion

Compound	$-\Delta H_f/x$ (kJ mol ⁻¹)	$-\Delta G_f/x$ (kJ mol ⁻¹)	Reference
Li _{0.22} V ₂ O ₅	328±3		3
δ-Li _{0.69} UO ₃	320±3		3
γ-Li _{0.55} UO ₃	310±5		3
Li _{0.29} UO _{2.67}	298±4		3
Li _{0.40} MoO ₃	277±4		3
h-Li _{0.44} WO ₃	277±6		3
*α-Na _{0.15} UO ₃	391±8		28
*Na _{0.20} V ₂ O ₅	360±7		37
*NaMo ₆ O ₁₇	310±10		37
δ-Na _{0.54} UO ₃	303±6		28
Na _{0.25} UO _{2.9}		296	this work
Na _{0.30} U ₃ O ₈		284	this work
Na _{0.27} WO ₃		251	38
Mg _{0.21} UO _{2.9}		475	this work
Mg _{0.20} U ₃ O ₈		461	this work
Mg _{0.22} UTiO ₅		442	this work
Zn _{0.20} UO _{2.9}		180	this work
Zn _{0.21} U ₃ O ₈		166	this work
Zn _{0.22} UTiO ₅		137	this work

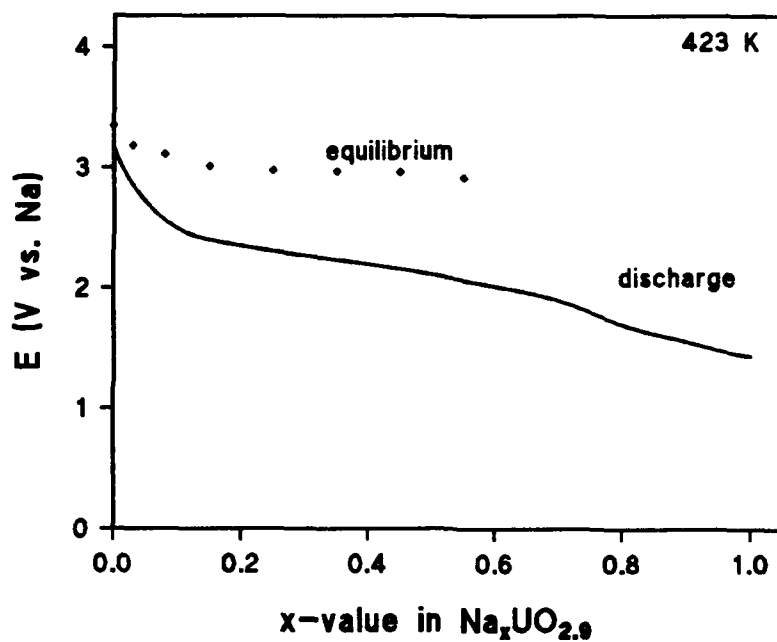
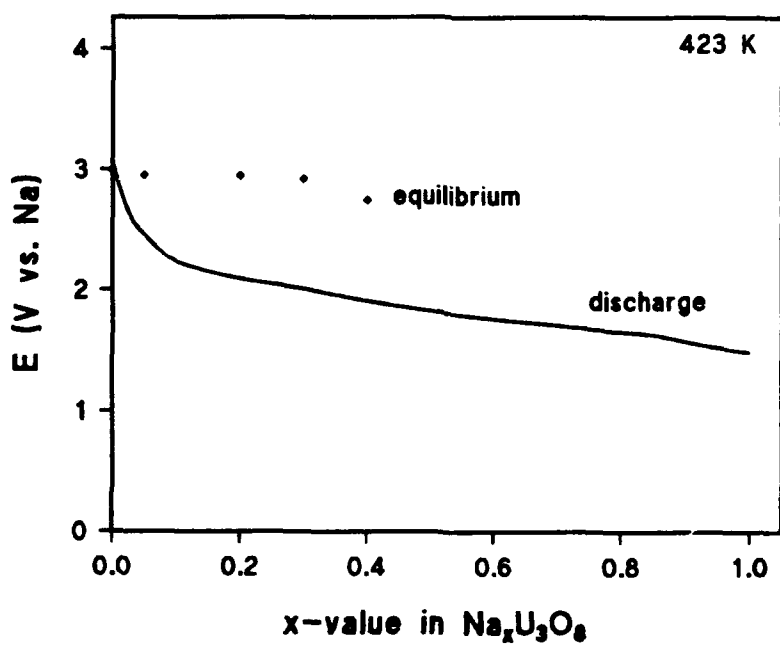
*High-temperature phase

Ambient-temperature insertion compounds are generally metastable towards either reconstitution to a stable high-temperature phase of the same composition or to decomposition into a mixture of compounds which surround that particular composition in the high-temperature ternary phase diagram (3). The compounds probably are metastable towards decomposition (Table 4.4).

Table 4.4 Free energies of decomposition

Reaction	x-value	ΔG (kJ mol ⁻¹)
$Mg_xUO_{2.9}(\alpha,s) = xMgUO_4(s) + 1.57xU_3O_8(s) + (1-5.71x)UO_{2.9}(\alpha,s)$	0.15	+0.2±2
$Na_xUO_{2.9}(\alpha,s) = x/2Na_2U_2O_7(s) + 0.86xU_3O_8(s) + (1-3.57x)UO_{2.9}(\alpha,s)$	0.15	-3.8±2
$Na_xU_3O_8(s) = x/2Na_2U_2O_7(s) + (1-x)U_3O_8(s) + x/2U_4O_9(s)$	0.20	+3.3±4

*Errors in ΔG are estimates taken from ΔH measurements

Figure 4.15 $\text{UO}_{2.9}$ at 25 μA in 0.1 M $\text{NaClO}_4/\text{DMSO}_2$ at 423 KFigure 4.16 U_3O_8 at 25 μA in 0.1 M $\text{NaClO}_4/\text{DMSO}_2$ at 423 K

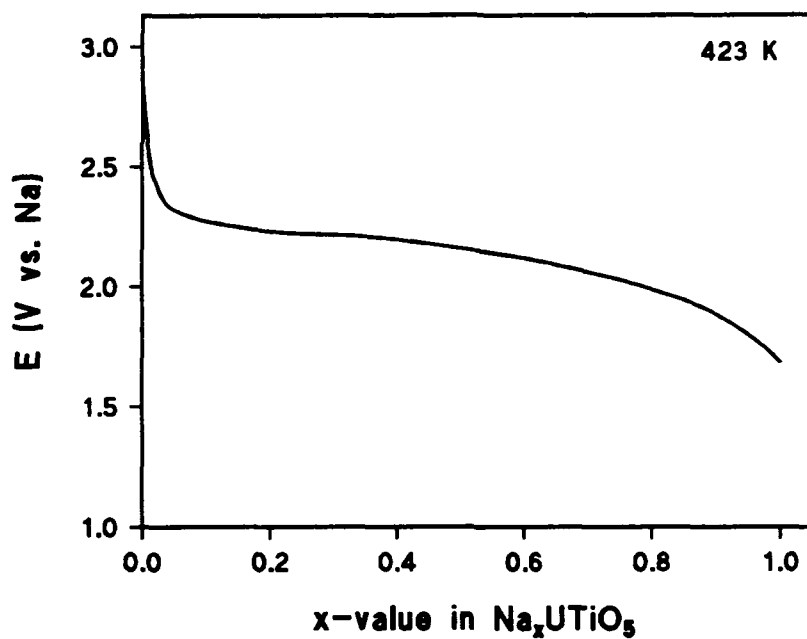


Figure 4.17 UTiO_5 at 25 μA in 0.1 M $\text{NaClO}_4/\text{DMSO}_2$ at 423 K

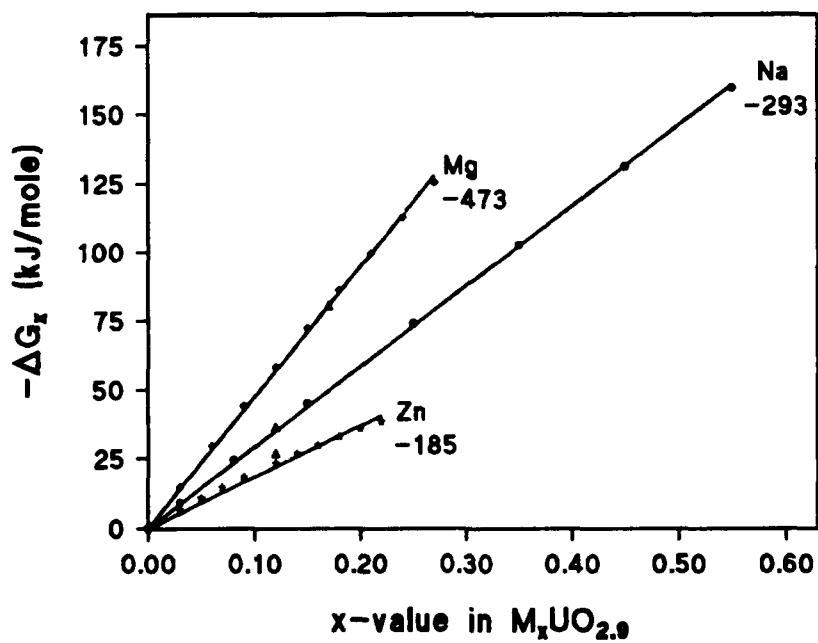


Figure 4.18 ΔG_x vs. x -value for $\text{UO}_{2.9}$. Calorimeter values for ΔH_x shown as open triangles (34)

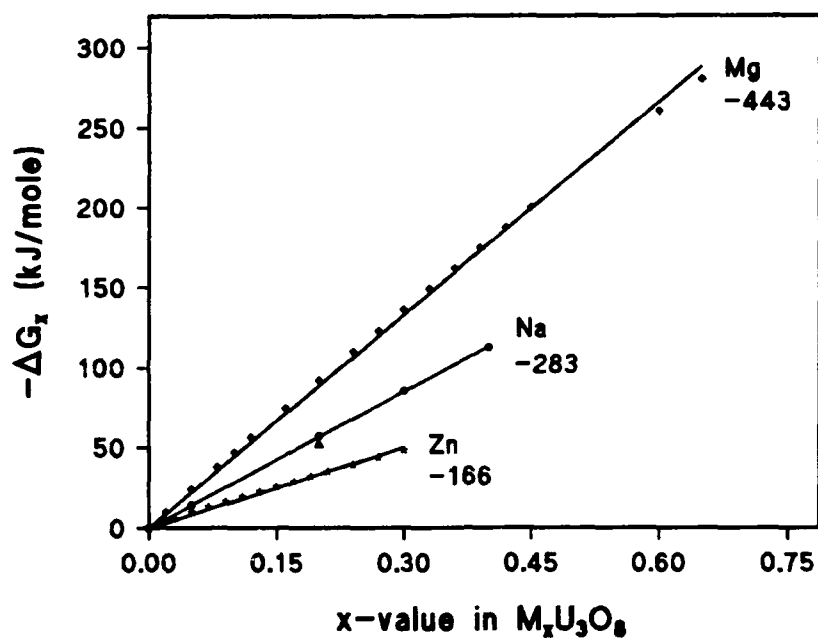


Figure 4.19 ΔG_x vs. x-value for U_3O_8 . Calorimeter values for ΔH_x shown as open triangles (34)

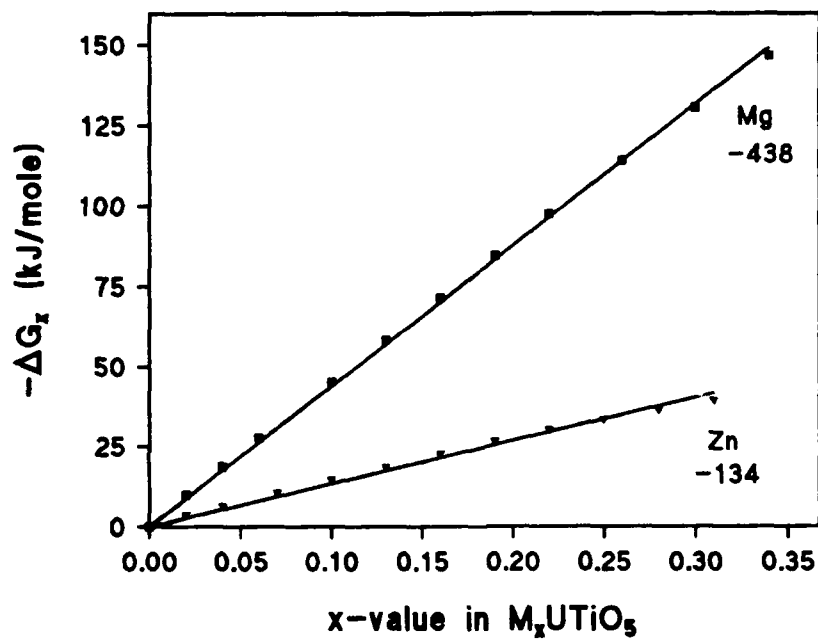


Figure 4.20 ΔG_x vs. x-value for $UTiO_5$.

A small decrease in site binding energies for sodium, magnesium, and zinc with the degree of uranium reduction can be observed by plotting $\Delta G_x/x$ vs. x -value (Figures 4.21 to 4.23). This trend was commented on previously by Dickens et al. (28). Estimates of site binding energies can be obtained by using a thermochemical cycle (35). The standard molar enthalpies of formation of binary- and ternary-metal oxides from gas-phase atoms vary approximately linearly with the metal's oxidation state (39), implying that the total binding energy varies linearly with the metal's oxidation state. Therefore, the site binding energy for the guest can be calculated from the difference between enthalpies of formation of the binary ($\text{MO}_{y-ax/2}$) and ternary (A^xMO_y) metal oxides at the same oxidation state of the metal ($\text{M}^{ax/2-y}$). As an example, the site binding energy of magnesium in $\text{UO}_{2.90}$ is calculated using the following scheme:



$$\Delta H_{24} = \Delta H_{19} + \Delta H_{20} + \Delta H_{21} + \Delta H_{22} + \Delta H_{23}$$

where ΔH_{21} is the hypothetical enthalpy of formation of $\text{UO}_{2.90-x}$ obtained from Figure 4.24. Values for ΔH_{22} and ΔH_{23} are calculated from data found in standard thermochemical tables (40). The free energy of insertion (ΔG_x) measured in this work was substituted for ΔH_{19} .

Table 4.5 lists the mean binding energies to oxygen for sodium, magnesium, and zinc $[\text{B}(\text{AO})]$ as given by $\Delta H_{24}/x$. The values support the assumption that the A-O site binding energy for a given inserted element varies little between metal oxides (3). The relative order of these values is reasonable in comparison to ΔH_f (per A) values for the formation of the corresponding metal oxides from gaseous atoms in the reaction



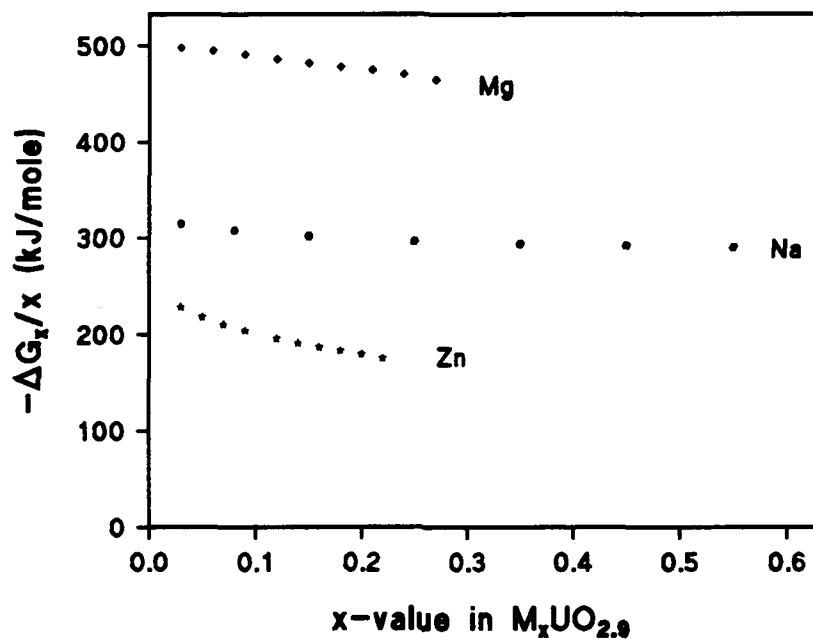
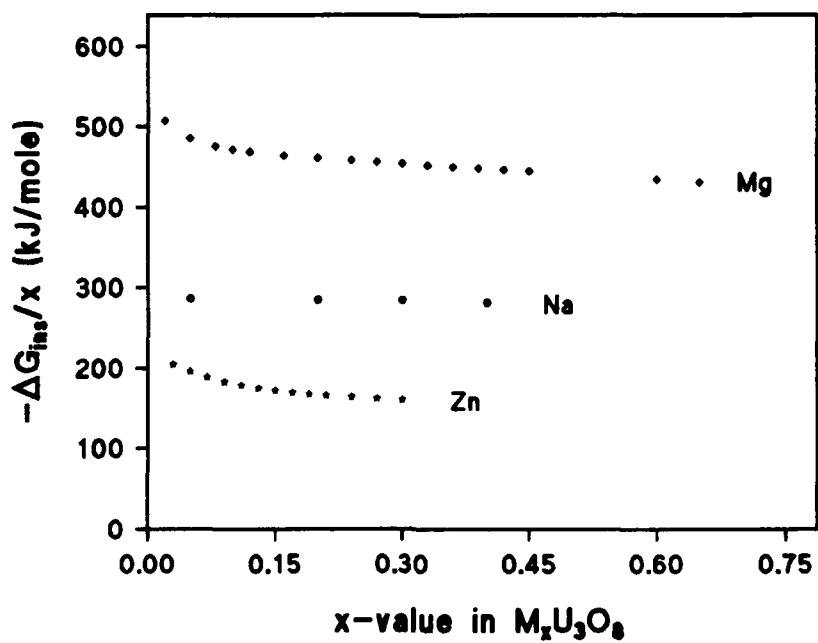
A plot of $\text{B}(\text{AO})$ vs. ΔH_f (per A) is shown in Figure 4.25.

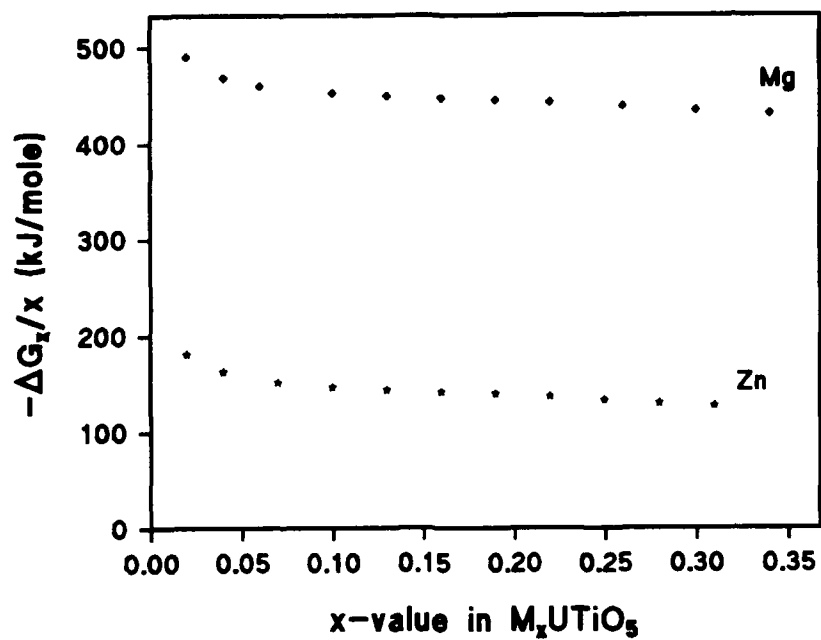
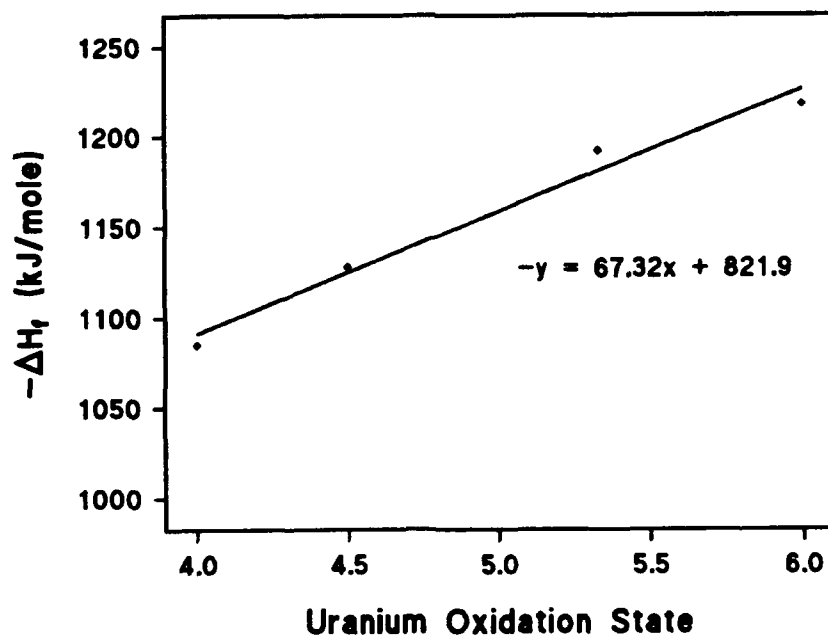
Table 4.5 Estimation of site binding energies

Compound	B(AO) (kJ mol ⁻¹)
Mg _{0.24} UO _{2.90}	1003
Zn _{0.18} UO _{2.90}	660
Na _{0.25} UO _{2.90}	558
¹ α-Li _{0.91} UO ₃	646
Mg _{0.20} UO _{2.67}	962
Zn _{0.08} UO _{2.67}	685
Na _{0.13} UO _{2.67}	582
² Li _{0.29} UO _{2.67}	689
¹ Reference 41	
² Reference 35	

4.5 KINETIC MEASUREMENTS

Kinetic values for Na⁺, Mg²⁺, and Zn²⁺ in single phase regions are listed in Table 4.6 along with values taken from the literature for these ions in other metal sulfide and oxide systems. The general trend in solid-state mobility, based upon values for D, is Li >> Na > Mg ≈ Zn. A similar trend was predicted by Ball (31) in his calculations of the activation energy of migration (E_a) for Li ($E_a = 0.7$ eV), Na ($E_a = 1.52$ eV), and Mg ($E_a = 1.25$ eV) in U₃O₈. Again, greater ionic size of sodium and the +2 charge of magnesium were cited as reasons for their larger activation energies when compared to lithium. Ball also calculated activation energies of migration in δ-UO₃ and found an even larger difference between Li ($E_a = 0.69$ eV), Na ($E_a = 3.81$ eV), and Mg ($E_a = 2.14$ eV). This large difference suggests Na and Mg insertion will be minimal, as was observed in this work.

Figure 4.21 $\Delta G_r/x$ vs. x-value for $UO_{2.9}$ Figure 4.22 $\Delta G_{iss}/x$ vs. x-value for U_3O_8

Figure 4.23 $\Delta G^\circ_e/x$ vs. x-value for $UTiO_5$ Figure 4.24 Least-squares fit of ΔH°_f of UO_x vs. uranium oxidation state

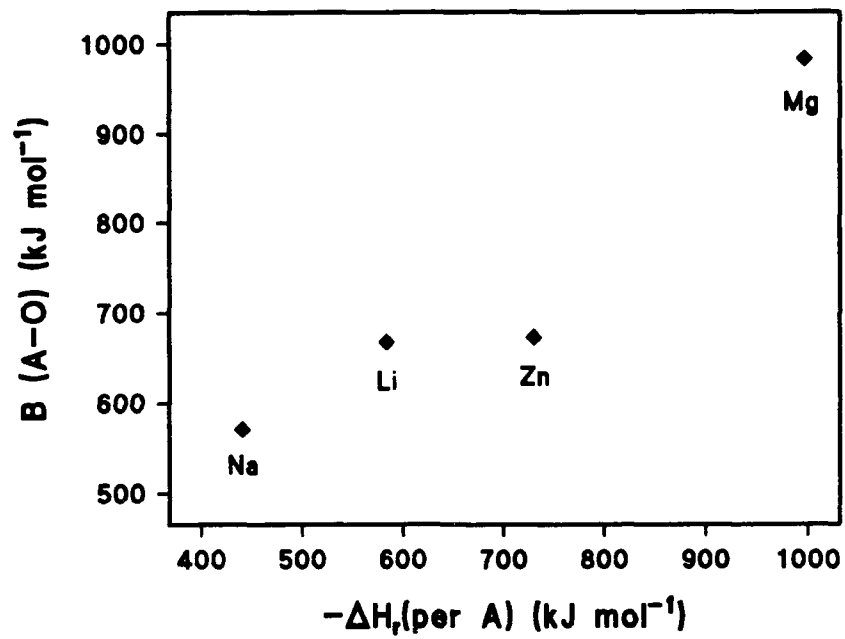


Figure 4.25 Site binding energy for A-O in $A_x\text{UO}_n$ vs. $-\Delta H_r$ (per A)

Table 4.6 Kinetic values of sodium, magnesium, zinc, and lithium in various metal oxides and sulfides

Cell	x-value	D (cm ² s ⁻¹)	D _n (cm ² s ⁻¹)	W	σ (Ω^{-1} cm ⁻¹)	Reference
Na _x UO _{2.9}	0.03	1.4E-11	6.0E-12	2.3	4.8E-8	this work
	0.08	1.1E-11	1.7E-12	6.2	3.7E-8	this work
Mg _x UO _{2.9}	0.03	3.7E-13	1.9E-13	2.0	2.2E-9	this work
Zn _x UO _{2.9}	0.03	9.2E-13	1.4E-13	6.5	1.6E-9	this work
	0.18	6.2E-12	1.4E-13	43.3	9.9E-9	this work
Na _x U ₃ O ₈	0.30	1.2E-11	2.9E-13	41.9	1.3E-8	this work
Mg _x U ₃ O ₈	0.02	8.1E-13	4.7E-13	1.7	1.4E-9	this work
	0.24	1.3E-11	6.4E-13	20.2	2.3E-8	this work
	0.45	1.5E-12	1.2E-13	13.0	7.8E-9	this work
Zn _x U ₃ O ₈	0.03	1.5E-12	1.6E-13	9.4	7.2E-10	this work
	0.13	5.1E-13	1.7E-13	3.1	3.3E-9	this work
Mg _x UTiO ₅	0.04	3.0E-12	7.4E-13	4.1	8.3E-9	this work
	0.22	1.3E-11	3.7E-13	35.6	2.3E-9	this work
Zn _x UTiO ₅	0.02	9.0E-12	2.2E-12	4.1	1.2E-8	this work
	0.22	1.1E-11	4.0E-13	27.2	2.5E-8	this work
Li _x U ₃ O ₈	0.88	2.8E-8				42
Li _x UTiO ₅	0.6	5.05E-9	4.0E-11			43
Zn _x V ₆ O ₁₃	0.05	3.7E-10				44
	0.1	3.5E-11				44
Na _x TiS ₂	0.6	1E-9				45
Na _x TaS ₂	0.4	3E-8				45
Na _x MnO ₂	0.2	4.6E-14				46
Na _x Mo ₂ O ₄	1.9	1E-10				47
Na _x WO ₃	1	1E-15				38
Na _x CrO ₂	0.6	1E-10				48
Na _x CoO ₂	0.6	5E-8				48

REFERENCES

1. Southampton Electrochemistry Group, Instrumental Methods in Electrochemistry, Ellis Horwood, London, (1990).
2. A. J. Bard and L. R. Faulkner, Electrochemical Methods, John Wiley & Sons, New York, (1980).
3. A. M. Chippindale, P. G. Dickens, and A. V. Powell, *Prog. Sol. State Chem.*, **21**, 133, (1991).
4. P. H. Rieger, Electrochemistry, Prentice-Hall, Englewood-Cliffs NJ, (1987).
5. O. Glemser and G. Lutz, *Z. Anorg. Allg. Chem.*, **264**, 17, (1951).
6. S. Falk and A. J. Salkind, Alkaline Storage Batteries, John Wiley & Sons, New York, (1968).
7. W. Weppner and R. A. Huggins, *Ann. Rev. Mater. Sci.*, **8**, 269, (1978).
8. W. Weppner and R. A. Huggins, *J. Sol. State Chem.*, **22**, 297, (1977).
9. C. J. Wen and R. A. Huggins, *Mat. Res. Bull.*, **15**, 1225, (1980).
10. C. J. Wen and R. A. Huggins, *J. Sol. State Chem.*, **35**, 376, (1980).
11. C. J. Wen, W. Weppner, B. A. Boukamp, and R. A. Huggins, *Met. Trans. B*, **11**, 131, (1980).
12. C. J. Wen and R. A. Huggins, *J. Electrochem. Soc.*, **128**, 1636, (1981).
13. J. P. Pereira-Ramos, R. Messina, and J. Perichon, *J. App. Electrochem.*, **16**, 379, (1986).
14. T. Palanisamy, R. L. Kerr, and J. T. Maloy, *J. Electrochem. Soc.*, **128**, 2090, (1981).
15. A. J. Vaccaro, T. Palanisamy, R. L. Kerr, and J. T. Maloy, *J. Electrochem. Soc.*, **129**, 4, 677, (1982).
16. A. J. Vaccaro, T. Palanisamy, R. L. Kerr, and J. T. Maloy, *J. Electrochem. Soc.*, **129**, 4, 682, (1982).
17. S. Basu and W. L. Worrell in Fast Ion Transport in Solids, (Vashishta, Mundy, and Shenoy eds.), Elsevier, Amsterdam, (1979).
18. W. F. Chu, H. Rickert, and W. Weppner, in Fast Ion Transport in Solids. Solid State Batteries and Devices, (W. van Gool ed.), North Holland Publishing Co., London, (1973).
19. H. Rickert and W. Weppner, *Z. Naturforsch., Teil A*, **29**, 1849, (1974).
20. B. C. H. Steele, in Mass Transport Phenomena in Ceramics, (A. R. Cooper and A. H. Heuer eds.), Plenum Press, New York, (1975).
21. J. B. Wagner, in Electrode Processes in Solid State Ionics, (M. Kleitz and J. Dupuy eds.), D. Reidel, Dordrecht, (1976).
22. A. Honders and G. H. J. Broers, *J. Sol. State Ion.*, **15**, 173, (1985).

Chapter 4 Chronopotentiometric Study

23. A. Honders, J. M. der Kinderen, A. H. van Heeren, J. H. W. de Wit, and G. H. J. Broers, *J. Sol. State Ion.*, **15**, 265, (1985).
24. W. Weppner and R. A. Huggins, *J. Electrochem. Soc.*, **124**, 10, 1569, (1977).
25. G. J. Reynolds, D. Phil. Thesis, Oxford, (1981).
26. J. Crank, The Mathematics of Diffusion, 2nd ed., Clarendon Press, Oxford, (1975).
27. J. P. Pereira-Ramos, R. Messina, and J. Perichon, *J. App. Electrochem.*, **16**, 379, (1986).
28. P. G. Dickens, A. V. Powell, and A. M. Chippindale, *Sol. State Ion.*, **28-30**, 1123, (1988).
29. R. G. J. Ball and P. G. Dickens, *J. Mater. Chem.*, **1**, 415, (1991).
30. M. J. Woodall, Chemistry Part II Thesis, Oxford, (1992).
31. R. G. J. Ball, D. Phil. Thesis, Oxford, (1992).
32. S. Kemmler-Sack and W. Rudorff, *Z. Anorg. Allg. Chem.*, **354**, 255, (1967).
33. J. P. Pereira-Ramos, R. Messina, and J. Perichon, *J. Electroanal. Chem.*, **218**, 241, (1987).
34. S. Patat, D. Phil. Thesis, Oxford, (1993).
35. P. G. Dickens, S. D. Lawrence, D. J. Penny, and A. V. Powell, *Sol. State Ion.*, **32/33**, 77, (1989).
36. P. G. Dickens and G. J. Reynolds, in Proc. Climax 4th Intern. Conf. Chemistry and Uses of Molybdenum, (H. F. Barry and P. C. H. Mitchell eds.), Climax Molybdenum Co., London, (1979).
37. P. G. Dickens and P. J. Wiseman, in Inorganic Chemistry Series Two V. 10. Solid State Chemistry, (L. E. J. Roberts ed.), Butterworths, London, (1975).
38. M. S. Whittingham, *J. Electrochem. Soc.*, **122**, 713, (1975).
39. S. Crouch-Baker, D. Phil. Thesis, Oxford, (1985).
40. O. Kubaschewski and C. B. Alcock, Metallurgical Thermochemistry, Pergamon, Oxford, (1979).
41. S. D. Lawrence, Chemistry Part II Thesis, Oxford, (1984).
42. P. G. Dickens, D. J. Penny, and M. T. Weller, *Sol. State Ion.*, **18/19**, 778, (1986).
43. G. P. Stuttard, Chemistry Part II Thesis, Oxford, (1990).
44. M. Z. A. Munshi, W. H. Smyrl, and C. Schmidtke, *Sol. State Ion.*, **47**, 265, (1991).
45. W. B. Johnson and W. L. Worrell, *Synthetic Metals*, **4**, 225, (1982).
46. J. Vondrak, J. Bludska, and I. Jakubec, *Electrochim. Acta*, **37**, 4, 603, (1992).
47. S. Colson, L. C. Klein, J. M. Tarascon, and D. Guyomond, *J. Electrochem. Soc.*, **139**, 9, 2359, (1992).
48. S. Kikkawa, S. Miyazaki, and M. Koizumi, *J. Power Sources*, **14**, 231, (1980).

CHAPTER 5 CYCLIC VOLTAMMETRIC STUDY OF CATION INSERTION

This chapter discusses the investigation of the mechanism of ion insertion into $\text{UO}_{2.9}$, U_3O_8 , $\gamma\text{-UO}_3$, and $\delta\text{-UO}_3$ using cyclic voltammetry.

5.1 THEORY

5.1.1 CLASSICAL SOLUTION VOLTAMMETRY

Controlled potential experiments (see Figure 5.1) can be divided into the two categories of potential step methods and potential sweep methods (1). In a potential step experiment, the potential is instantaneously changed (ΔE) or stepped from one value to another generating the waveform shown in Figure 5.2 and the current response is monitored with time. The complete electrochemical behavior of a system can be discerned by varying ΔE and plotting the current-time responses.

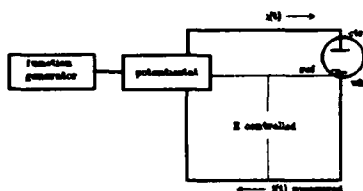


Figure 5.1 Schematic experimental arrangement for controlled potential experiments

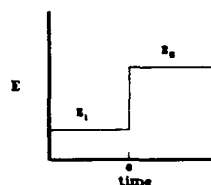


Figure 5.2 Waveform for a potential step experiment

However, more information can be gained in a single experiment by sweeping the potential with time and recording the current-potential response (Figure 5.3). The term for this technique is linear sweep voltammetry (LSV). A generally more useful technique is cyclic voltammetry (CV) which involves reversing the direction of the potential sweep at some time λ corresponding to the potential E_λ (Figure 5.4) (2). On reaching E_λ the sweep can be indefinitely halted, reversed, or continued in the same direction to another value.

Chapter 5 Cyclic Voltammetry

Cell current is monitored as a function of potential in both LSV and CV. Sweep rates vary in the range of 10^{-3} to 10^3 V/s depending upon the system and experiment. By observing the dependence of peak current (i_p) and potential (E_p) upon sweep rate (v), mechanistic and kinetic information about processes occurring at the working electrode can be obtained.

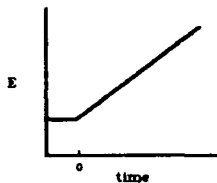


Figure 5.3 Waveform for linear sweep voltammetry

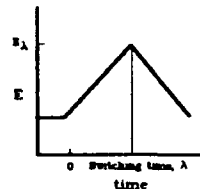


Figure 5.4 Waveform for cyclic voltammetry

Theoretical treatments of electrochemical systems require they be divided into one of the following three groups on the basis of their electrochemical reversibility: reversible, irreversible, and quasi-reversible (1,2).

Reversible Systems

Consider the reversible reaction where species O is electrochemically reduced to form R, assuming semi-infinite linear diffusion and the initial absence of R.



The potential is swept linearly at v V/s with the potential at time t given by

$$\begin{aligned} E(t) &= E_i - vt & \text{for } 0 < t < \lambda \\ E(t) &= E_i - 2v\lambda + vt & \text{for } t > \lambda \end{aligned} \quad (5.2)$$

Electron transfer is rapid enough for the Nernst equation

$$E = E^\circ + \frac{RT}{nF} \ln(C_O/C_R) \quad (5.3)$$

to apply at the electrode surface ($x = 0$). The exact form of the cyclic voltammogram is obtained from the solution of Fick's second law for O and R (assuming $D_O = D_R = D$) with the following conditions

$$\partial C/\partial t = D\partial^2 C/\partial x^2 \quad (5.4)$$

at $t = 0, x > 0$: $C_O = C_O^\infty$ and $C_R = 0$

at $t > 0, x = \infty$: $C_O = C_O^\infty$ and $C_R = 0$

at $t > 0, x = 0$: $D(\partial C_O/\partial x) + D(\partial C_R/\partial x) = 0$

$(C_O/C_R)_{x=0} = \exp[nF/(RT)(E - E^*)]$

$-i = nFDA(\partial C_O/\partial x)_{x=0}$

which at 25°C yields the Randles-Sevcik equation:

$$i_p = (-2.69 \times 10^5)n^{3/2}AC_O^\infty D^{1/2}v^{1/2} \quad (5.5)$$

Peak current (i_p) is seen to be proportional to the bulk concentration of the electroactive species (C_O^∞) and to the square roots of the chemical diffusion coefficient (D) and sweep rate

(v). Diagnostic tests for cyclic voltammograms of reversible processes at 25°C are (2):

1. $\Delta E_p = 59/n$ mV
2. $|E_p - E_{p/2}| = 59/n$ mV
3. $|i_p^A/i_p^C| = 1$
4. $i_p \propto v^{1/2}$
5. E_p is independent of v
6. at potentials beyond E_p , $i \propto t^{-1/2}$

Test 4 is particularly applicable to this study because it indicates diffusion control is occurring within the system.

Irreversible Systems

For irreversible processes ($O + ne^- \rightarrow R$) the rate of electron transfer is insufficient to maintain Nernstian equilibrium at the electrode surface and a new boundary condition for $t > 0, x = 0$ must be substituted into equation 5.4.

$$-i/(nFA) = D_O(\partial C_O/\partial x)_{x=0} = k(C_O)_{x=0} \quad (5.6)$$

Numerical integration leads to the solution

$$i_p = (-2.99 \times 10^5)n(\alpha_c n_\alpha)^{1/2}AC_O^\infty D_O^{1/2}v^{1/2} \quad (5.7)$$

where α_c is the transfer coefficient and n_α is the number of electrons transferred up to and including the rate determining step. Diagnostic tests for totally irreversible systems at 25°C are (2)

1. no reverse peak
2. $i_p^c \propto v^{1/2}$
3. E_p^c shifts $-30/\alpha_c n_\alpha$ mV for each decade increase in v
4. $|E_p - E_{p/2}| = 43/\alpha_c n_\alpha$ mV.

Besides the absence of a reverse peak the irreversible system shows a dependence of peak current on the square root of the scan rate.

Quasi-reversible Systems

As the name implies, quasi-reversible systems exhibit behavior of both reversible and irreversible systems. At slow scan rates, the rate of electron transfer relative to mass transport is adequate to maintain Nernstian equilibrium at the electrode surface and thus behavior is reversible. The transition to irreversible behavior occurs at higher scan rates where the electron transfer rate is not adequate to maintain Nernstian equilibrium. The solution to equation 5.4 is not important to this study, but the diagnostic tests for quasi-reversible systems are useful (2):

1. $|i_p|$ increases with $v^{1/2}$ but is not proportional to it
2. $|i_p^a/i_p^c| = 1$ provided $\alpha_c = \alpha_a = 0.5$
3. ΔE_p is greater than $59/n$ mV and increases with v
4. E_p^c shifts negatively with increasing v .

The discussion of cyclic voltammetry thus far has assumed that all the reactants and products are freely soluble in solution without considering surface processes such as phase formation and reversal and reactant or product adsorption. Reactions involving surface processes exhibit shapes and sweep rate dependences in their voltammograms different from those previously discussed. The simplest case is where the electroactive species O is already present on the electrode surface. Analysis of such a system is fairly straightforward since mass transport effects (i.e. diffusion, migration, and convection) can be ignored. For example, in the case of adsorption described by a Langmuir isotherm, the governing equation is (2)

$$|i_p^c| = An^2F^2\Gamma_O v/(4RT) \quad (5.8)$$

where Γ_O is the initial surface excess of O. It is important to note that i_p is proportional not to $v^{1/2}$ as before, but to v . This distinction is indicative of the role mass transport plays and will be important in later discussions on insertion (1,2).

5.1.2 SOLID-STATE VOLTAMMETRY

The theoretical treatment of solid-state systems is more complex than that of liquid solutions previously discussed because mass transport occurs in both the liquid and solid

phases. Two kinetic models of insertion compounds were developed by Reichman and Bard (3) for H_xWO_3 and Vaccaro et al. (4) for Li_xTiS_2 . These models assume that mass transport of ions within solution and electronic conduction within the solid are not rate limiting processes. This leaves only charge transfer or solid-state mass transport as the rate determining step. The remainder of this chapter focuses on the investigation of these two processes in the electrochemical formation of uranium oxide insertion compounds.

5.2 CYCLIC VOLTAMMETRY OF INSERTION COMPOUNDS

Voltammetric studies of insertion compounds have been much less prevalent than chronopotentiometric studies. Work by Vacarro et al. on TiS_2 (4), Pereira-Ramos with V_2O_5 (5,6), Hardwick with MoO_3 (7), Armand et al. (8) with RuO_2 , and Novák et al. (9) on various transition-metal oxides and sulfides showed that voltammetry can be used to study the insertion process. However, the drawback to these studies was that, under the conditions in which these experiments have to be conducted, the slow kinetics of the insertion process required the use of very slow scan rates ($v \leq 2 \text{ mV/s}$) and the useful time domain available for exploration of mechanistic aspects remained very restricted (tens of minutes time scale). Furthermore, electrodes in some cases were large (area $\approx 2 \text{ cm}^2$) and contained high amounts of graphite (upwards of 90 weight-percent) added to increase conductivity which caused high background currents that tended to obscure details of the voltammograms.

In order to obtain a voltammetric response in the seconds time domain for a metal oxide, in addition to having adequate electrical conductivity, it is necessary to have available at least two accessible metal oxidation states between which electron transfer can take place with a mass transport mechanism to maintain electroneutrality. In the case of the uranium oxides considered in this study, the U(VI)/U(V) oxidation states should be readily available, although it is less obvious how the conductivity and mass transport requirements may be satisfied. Ionic motion within a solid was discussed in Chapter 4 with the conclusion that Na^+ , Mg^{2+} , and Zn^{2+} mass transport within the solid is likely to be predominantly diffusion controlled.

In view of the above discussion, provided adequate conductivity is available in uranium oxides, their voltammetry may be expected to show electron transfer between the

U(VI)/U(V) metal cations coupled with diffusion of ions that may be capable of insertion into the reduced form of the lattice. Recently, a new approach to studying the voltammetry of solids was developed whereby trace amounts of solution-phase insoluble solid material are mechanically transferred, rather than electrochemically deposited, onto the surface of a suitable solid electrode (10-14) which is then placed in an electrolyte containing solution where electrochemical aspects of the process may then be studied by conventional voltammetry at fast scan rates. With this method, experimental procedures are extremely simple and wide time domains may be readily achieved since the redox chemistry in the solid takes place in what are effectively arrays of small electroactive sites where diffusion is hemispherical and IR drop problems, which are likely to be important with semi- and non-conductors such as the uranium oxides, are minimized.

5.3 DESCRIPTION OF TEST SET-UP

Figure 5.5 shows the three-compartment Pyrex cell in which cyclic voltammetry experiments were conducted. The working electrode was 3.2 mm diameter high purity graphite rod (Ultra Carbon) used without further treatment. Solid samples were ground with a mortar and pestle (5-10 μm particle size) and the lower surface of the graphite rod pressed into the powder and rubbed gently on it. The electrode was lightly tapped several times to remove loose sample and the edges of the rod wiped clean with a tissue. The height of the electrode was adjusted within the cell to expose only its lower surface to the electrolyte. After each measurement the electrode surface was renewed by simply cutting off the end of the graphite rod with a scalpel.

The reference electrode in all cases was a Radiometer-Copenhagen model K401 saturated calomel electrode which was connected to the working electrode compartment via a Luggin capillary. Platinum mesh served as the counter electrode. Solutions were made to the stated concentrations using deionized water and either $\text{MgCl}_2 \cdot 6\text{H}_2\text{O}$ (BDH), $\text{Mg}(\text{ClO}_4)_2$ (BDH), $\text{LiCl} \cdot 6\text{H}_2\text{O}$ (BDH), NaCl (Fluka), or CsCl (BDH) without further purification. High purity argon was passed through an oxygen removal column (Chrompack) ($\text{O}_2 < 1 \text{ ppm}$) and bubbled into the cell for at least 20 minutes prior to each experiment. Solution pH was measured using a Radiometer-Copenhagen model 84 research pH meter.

Voltammetric measurements were made using an instrument built by Ursar Scientific and recorded on a Gould model 60000 X-Y recorder. Experiments were divided into two categories on the basis of their time domain: short - up to several minutes and long - from 1 to 12 hours. All experiments were conducted at ambient temperature ($\approx 20^\circ\text{C}$).

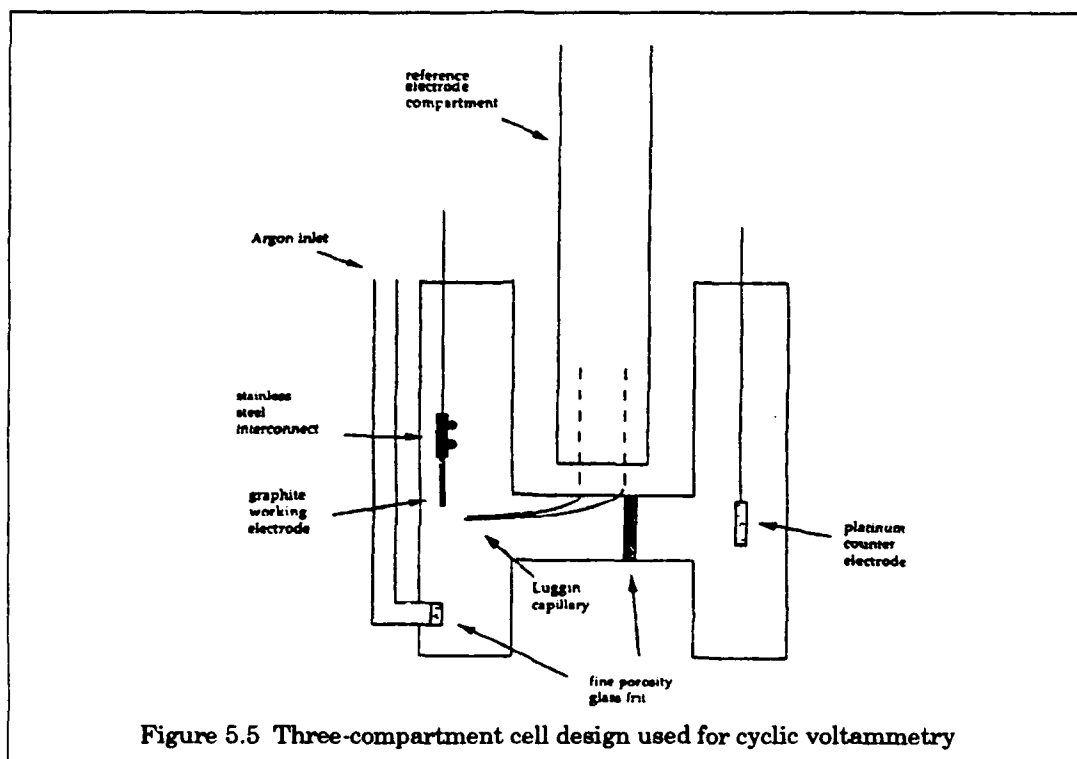


Figure 5.5 Three-compartment cell design used for cyclic voltammetry

5.4 VOLTAMMETRY OF U_3O_8

5.4.1 SHORT TIME DOMAIN EXPERIMENTS IN ELECTROLYTE CONTAINING Mg^{2+}

As was shown in Chapters 2 and 4, Mg^{2+} does not form insertion compounds as readily as monovalent cations such as Li^+ and Na^+ and its mobility in the solid-state is lower. However, the method of their preparation suggests that the electron transfer process, $\text{U(VI)} \rightarrow \text{U(V)}$, still is coupled with insertion of the ions. Consequently, if Mg^{2+} ions are not rapidly inserted, then details of the coupling of electron transfer and mass transport prior to cation insertion may be revealed by short time domain (fast scan) voltammetric studies.

The first and 30th scans of cyclic voltammograms ($v = 100 \text{ mV/s}$) obtained for U_3O_8 mechanically attached to a carbon electrode in 0.1 M and 0.5 M MgCl_2 are shown in Figures 5.6a and 5.6b. The primary reduction process (labelled process 1 in Figure 5.6), which is the same in both MgCl_2 and $\text{Mg}(\text{ClO}_4)_2$ (curves not shown) electrolytes over the scan rate range

of 20 to 500 mV/s, is characterized by an almost chemically reversible, surface confined, one-electron transfer process which may be written as



In 0.1 M $MgCl_2$, a well defined almost symmetric reduction peak found at ≈ -0.8 V (all potentials versus SCE) is coupled with an equally sharp oxidation peak at ≈ -0.6 V to give process 1. On the first reverse scan of the cyclic voltammogram, a small, broad oxidation peak is observed at ≈ -0.15 V. In 0.1 M $MgCl_2$, as the potential range was repeatedly scanned or cycled, a second broad reduction peak slowly developed at ≈ -0.25 V to form an almost chemically reversible couple labelled process 2 in Figure 5.6a. Even after interruption of cycling, with the potential held at the initial value (+0.20 V) for several minutes, both processes were retained in the voltammogram after recommencing the scanning, confirming that the U_3O_8 remains attached to the surface at all times. After the initial development of process 2 cycling could be continued for very lengthy periods (hours) with the only change being a decrease in the peak currents (i_p).

It is worth noting at this point that the clarity of the voltammograms was partially dependent upon the amount and distribution of the metal oxide on the electrode surface. All scans of samples of a given metal oxide mechanically transferred to the carbon electrode had the same general shape and peak positions, but some samples produced sharper peaks than others. Such behavior implies the surface area of the metal oxide plays a role in the insertion process. Additionally, uncompensated resistance may cause ohmic distortion, particularly when large amounts of material are transferred to the electrode surface.

The scan rate dependence of process 1 for a single, well conditioned sample (i.e. cycled numerous times) was examined over the range 20 to 500 mV/s. The reduction peak current ($(i_p^{red})_1$) increases and peak potential ($(E_p^{red})_1$) shifts negatively as the scan rate increases. Interestingly, a plot of $(i_p^{red})_1$ versus $v^{1/2}$ for process 1 in all magnesium electrolytes examined (0.1 to 2.0 M $MgCl_2$ and 0.1 M $Mg(ClO_4)_2$) yields a linear equation, which in the case of data shown in Figure 5.7, is given in equation 5.10.

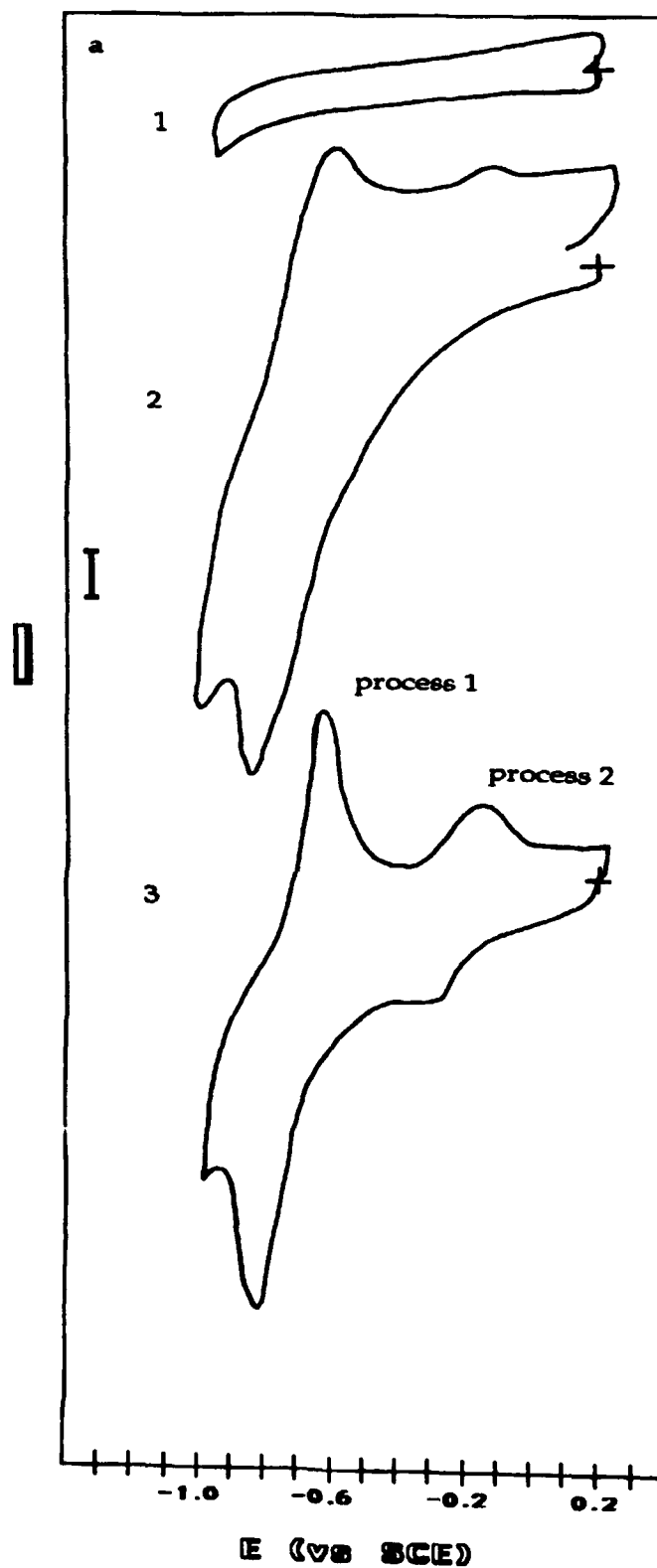


Figure 5.6 Cyclic voltammograms for reduction of U_3O_8 with $v = 100 \text{ mV/s}$ and $i = 20 \text{ } \mu\text{A/unit}$ in a) 0.1 M MgCl_2 1) background, 2) U_3O_8 initial cycle, and 3) U_3O_8 30th cycle

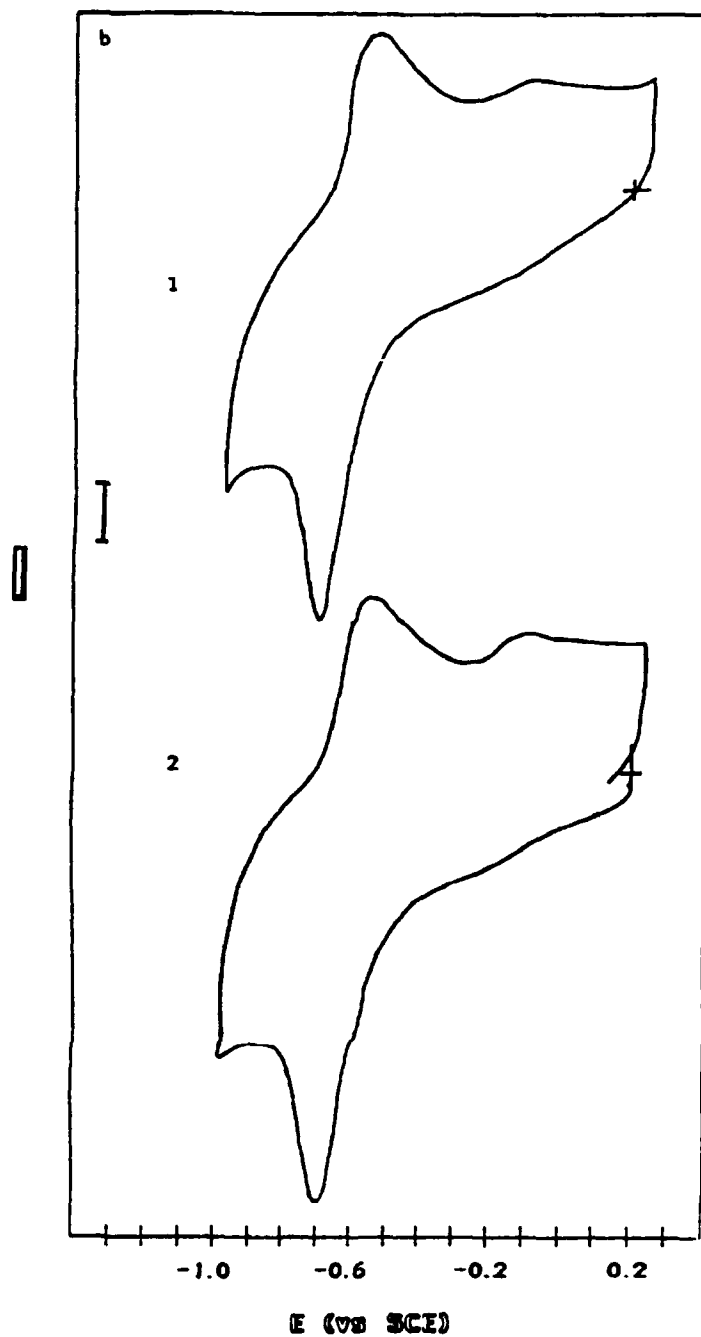


Figure 5.6b 0.5 M MgCl_2 1) U_3O_8 initial cycle and 2) U_3O_8 30th cycle

$$(i_p^{\text{red}})_1 (\mu\text{A}) = 10.2v^{1/2} - 30.7 \quad (R^2 = 0.999) \quad (5.10)$$

The $v^{1/2}$ dependence of i_p^{red} (see Figure 5.8) suggests that mass transport by diffusion is coupled to electron transfer. If only a surface confined process were present (i.e. no diffusion coupled with electron transfer), $(i_p^{\text{red}})_1$ should exhibit a linear dependence on v rather than $v^{1/2}$ (1). Correction of $(i_p^{\text{red}})_1$ for the background current requires an extrapolation of data obtained at potentials well removed from the peak potential. A systematic error in

Chapter 5 Cyclic Voltammetry

correcting for the background in this way may account for the non-zero intercept reported in equation 5.10.

On comparison of Figures 5.6a and 5.6b it is apparent that process 1 (but not process 2) shifts to more positive potentials at the higher MgCl_2 concentration. Table 5.1 provides the peak potentials for process 1 at various scan rates and MgCl_2 concentrations. While data are not completely reproducible because of uncertainties in the amount of material transferred to the electrode in each experiment, the direction of shifts in potential are considerable and significant within experimental error. Data in Table 5.1 also show the expected pH decrease with increasing MgCl_2 concentration. However, experiments with addition of hydrochloric acid showed that the shifts in potential are not due to the pH change over the range 3 to 6.

Table 5.1 Peak potentials ($E_{p, \text{red}}$, $E_{p, \text{ox}}$ in V) for process 1 obtained from cyclic voltammetry of U_3O_8 at various scan rates and MgCl_2 concentrations

Scan Rate (mV/s)	[MgCl_2] M							
	0.1 M (6.5) ^a		0.1 M (3.3) ^{a, b}		0.5 M (6.0) ^a		2.0 M (4.4) ^a	
	$E_{p, \text{red}}$	$E_{p, \text{ox}}$	$E_{p, \text{red}}$	$E_{p, \text{ox}}$	$E_{p, \text{red}}$	$E_{p, \text{ox}}$	$E_{p, \text{red}}$	$E_{p, \text{ox}}$
50	-0.79	-0.65	-0.78	-0.64	-0.70	-0.54	-0.63	-0.49
100	-0.81	-0.64	-0.80	-0.63	-0.70	-0.53	-0.63	-0.48
200	-0.83	-0.58	-0.83	-0.59	-0.70	-0.52	-0.64	-0.46
500	-0.87	-0.55	-0.86	-0.53	-0.71	-0.50	-0.64	-0.43

^a pH value

^b pH adjusted with HCl(aq)

The dependence of $(i_{p, \text{red}})_1$ on $v^{1/2}$ indicates that diffusion is coupled to the U(VI)/U(V) electron transfer process in the solid attached to the carbon surface. The lack of dependence on the anion (0.1 M MgCl_2 and 0.1 M $\text{Mg}(\text{ClO}_4)_2$ electrolytes give the same results) suggests that the anion is not the diffusing species whereas the dependence on Mg^{2+} concentration is consistent with diffusion of this ion. If Mg^{2+} transport from the bulk solution to the solid occurs on the voltammetric time scale, then the voltammetry should be modified by stirring the solution. However, as shown in Figure 5.9 both the peak position and peak current are independent of stirring rate. By inference, the data are then only explicable in terms of Mg^{2+} diffusion occurring within the solid which is coupled to the electron transfer process.

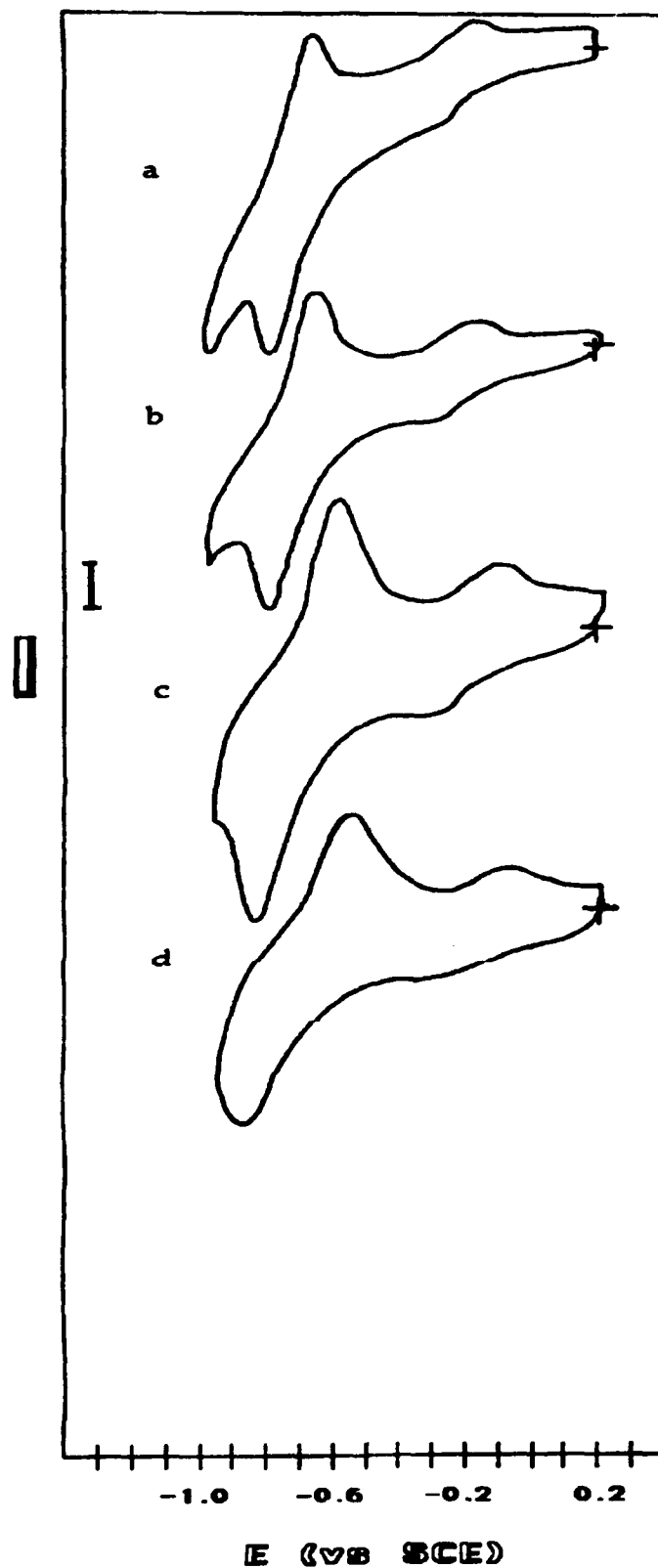


Figure 5.7 Cyclic voltammograms for reduction of U_3O_8 in 0.1 M MgCl_2 at various scan rates: a) 20 mV/s, $i = 10 \mu\text{A/unit}$; b) 50 mV/s, $i = 20 \mu\text{A/unit}$; c) 200 mV/s, $i = 40 \mu\text{A/unit}$; and d) 500 mV/s, $i = 100 \mu\text{A/unit}$

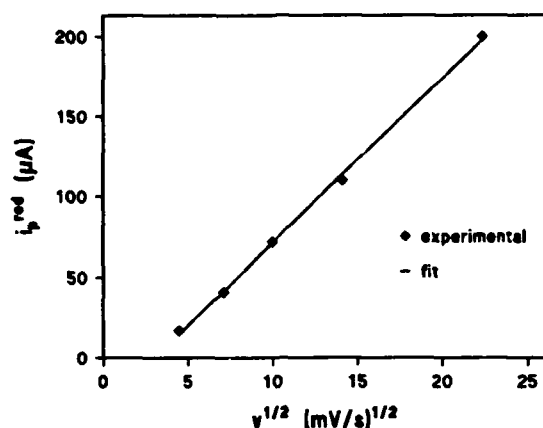


Figure 5.8 Plot of $(i_p^{\text{red}})_1$ vs. $v^{1/2}$ for U_3O_8 in 0.1 M MgCl_2

5.4.2 LONG TIME DOMAIN EXPERIMENTS IN ELECTROLYTE CONTAINING Mg^{2+}

The short time domain experiments discussed above appear to reflect electron transfer coupled with diffusion of Mg^{2+} within the lattice. The starting potential was changed in another set of experiments to -1.2 V and held here for a fixed period of time before scanning in the positive direction (Figure 5.10). During the period while the potential is held at -1.2 V reduction and diffusion will occur on a much longer time scale than is the case with the previously described experiment where only a few seconds are available at the potential where reduction coupled with diffusion occur. After holding the potential at -1.2 V, voltammograms have the same basic shape as before, but the potentials of process 1 shift to more positive values. Under the conditions given in Figure 5.10, $(E_p^{\text{red}})_1 = -0.78$ V and $(E_p^{\text{ox}})_1 = -0.38$ V as compared to $(E_p^{\text{red}})_1 = -0.83$ V and $(E_p^{\text{ox}})_1 = -0.58$ V for the previously described experiment. Cycling caused the $(E_p^{\text{ox}})_1$ to return to a more negative potential ($(E_p^{\text{ox}})_1 = -0.47$ V), yet both peaks remained more positive than previous values. Returning the starting potential to its previous value of +0.20 V and holding it there for one hour restored the peaks to their previous potentials listed in Table 5.1. The longer the time the potential is held at -1.2 V, the more positive becomes process 1, consistent with data obtained with increasing the Mg^{2+} concentration in the previously described experiments. Apparently, holding the potential at -1.2 V causes the concentration of Mg^{2+} in the reduced oxide to increase by diffusion into the lattice as is required to form an insertion compound.

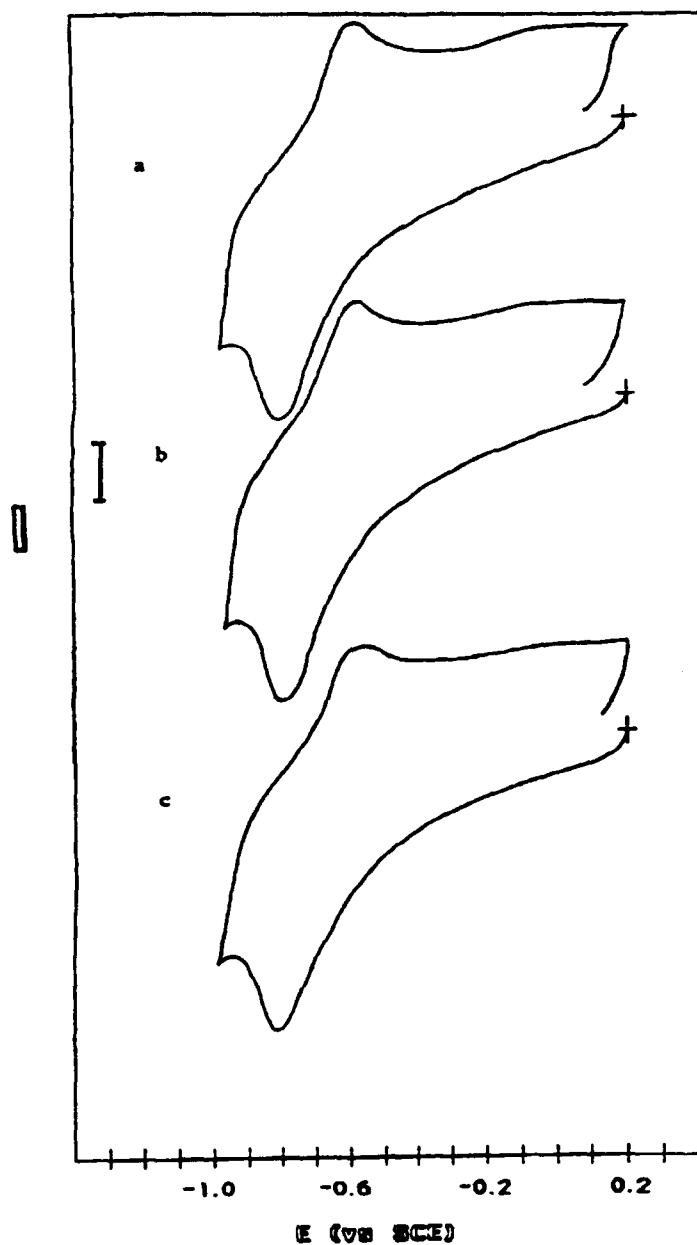


Figure 5.9 Cyclic voltammograms for reduction of U_3O_8 in 0.1 M MgCl_2 with $v = 200$ mV/s and $i = 40$ $\mu\text{A}/\text{unit}$: a) no stirring, b) slow stirring, and c) fast stirring of the solution

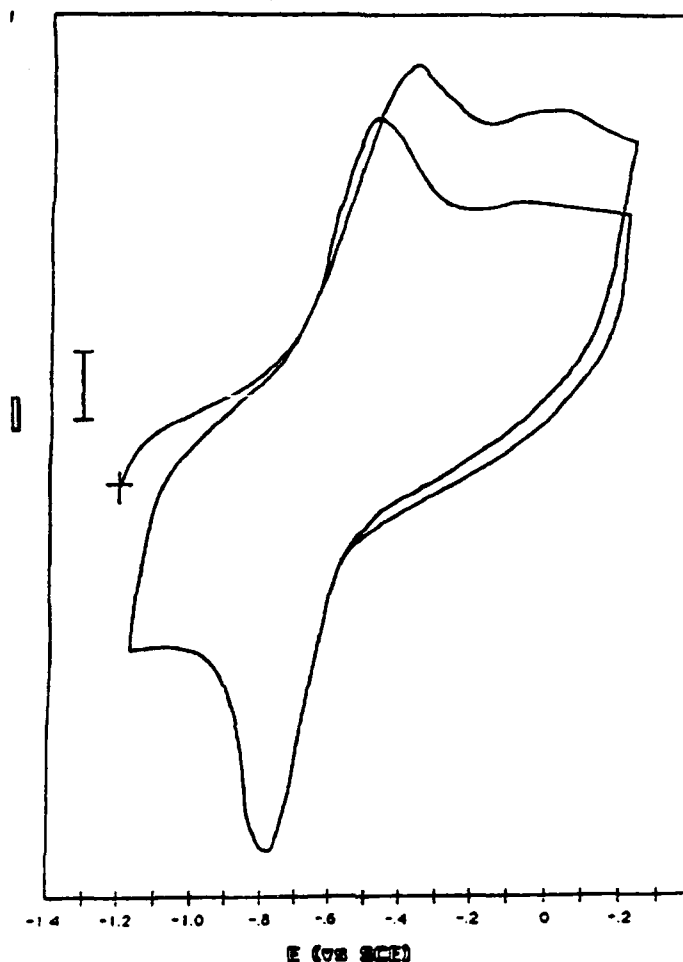


Figure 5.10 First two cyclic voltammograms of U_3O_8 in 0.1 M MgCl_2 ($v = 200$ mV/s, $i = 20$ $\mu\text{A}/\text{unit}$) held at an initial potential of -1.2 V for 30 minutes

5.4.3 SHORT TIME DOMAIN EXPERIMENTS WITH MIXED CATION ELECTROLYTES

Two other insertion ions, Li^+ and Na^+ , were used as electrolytes to study the reduction of U_3O_8 mechanically transferred to the carbon electrode. Results (Figures 5.11a, 5.11b and 5.12a, 5.12b) show contrasting and similar behavior to that obtained with Mg^{2+} . The most apparent difference in the Li^+ and Na^+ electrolytes is the large decrease in $(i_p^{\text{ox}})_1$ on the reverse or oxidative scan direction at ≈ -0.60 V for both ions. Additionally, $(E_p^{\text{red}})_1$ occurred at more negative potentials in both electrolytes (Table 5.2). Voltammograms became more complex with cycling, although a dependence of $(i_p^{\text{red}})_1$ on $v^{1/2}$ was always observed. Electrodes initially cycled over the potential range $+0.2$ to -1.0 V in 0.1 M XCl ($\text{X} = \text{Li}^+$ or Na^+) were then transferred to an electrolyte containing 0.1 M XCl and 0.1 M MgCl_2 and again cycled over the same potential range (Figures 5.11c and 5.12c). For both solutions,

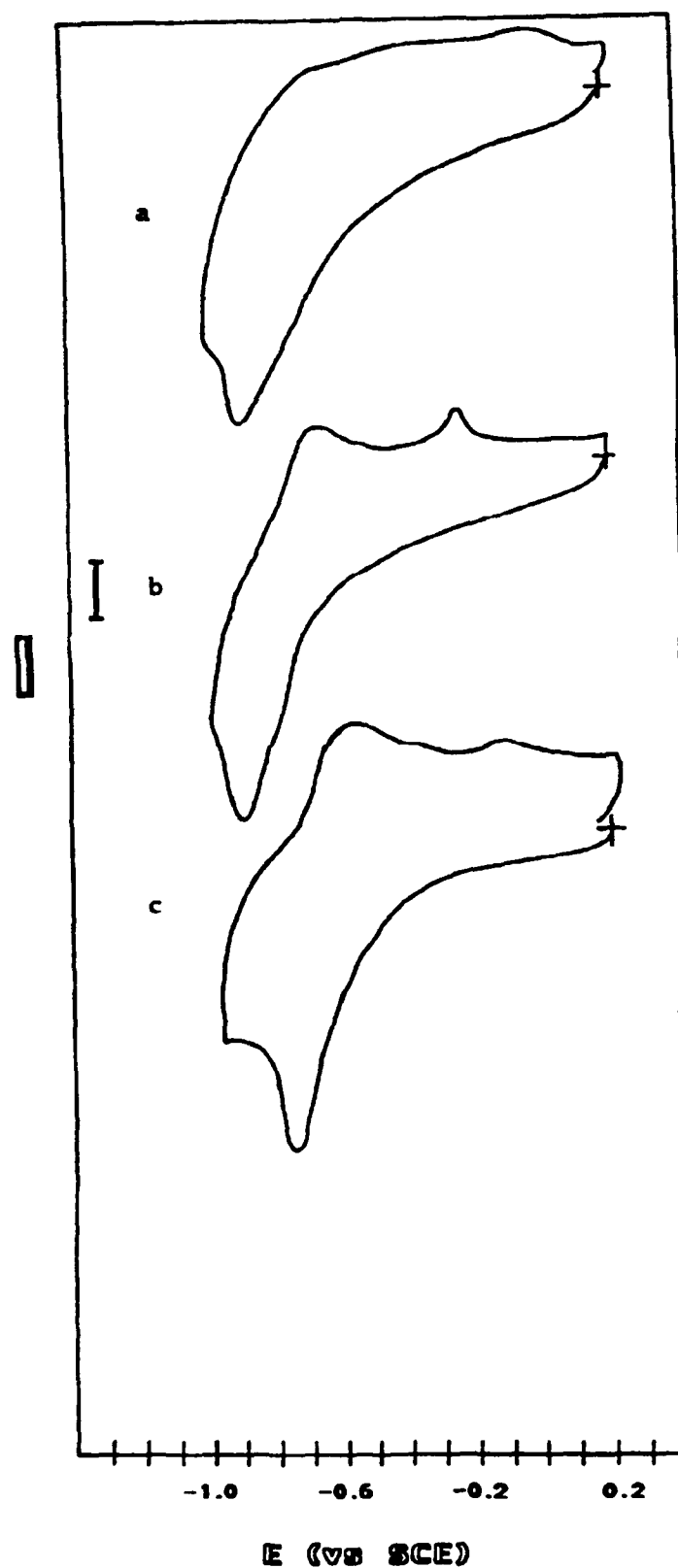


Figure 5.11 Cyclic voltammograms for reduction of U_3O_8 at $v = 100$ mV/s and $i = 20$ μ A/unit in a) 0.1 M LiCl, initial cycle; b) 0.1 M LiCl, 35th cycle; and c) 0.1 M LiCl + 0.1 M $MgCl_2$, initial cycle

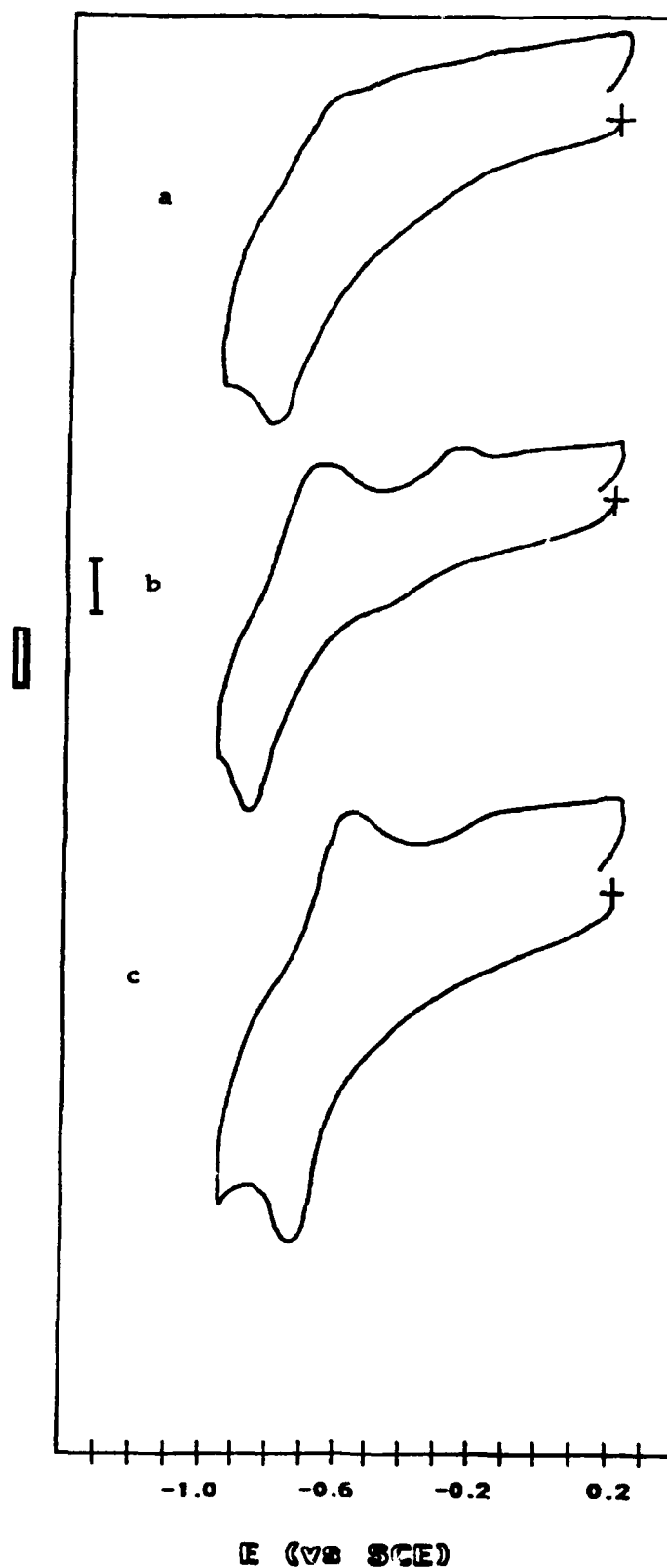


Figure 5.12 Cyclic voltammograms for reduction of U_3O_8 at $v = 100$ mV/s and $i = 20$ μ A/unit in a) 0.1 M NaCl, initial cycle; b) 0.1 M NaCl, 35th cycle; and c) 0.1 M NaCl + 0.1 M $MgCl_2$, initial cycle

the shapes and peak potentials of the voltammograms rapidly became identical to the short and long time domain data for the Mg^{2+} electrolyte described above. In the case of Li^+ and Na^+ electrolytes, it would appear these ions diffuse rapidly enough to positions within the host oxide which leads to the observation of an irreversible process, as is the case with long time domain magnesium experiments. That is in the Na^+ and Li^+ cases the electron transfer and diffusion steps are not resolved at scan rates in the range 20 to 500 mV/s, although at the upper limit some evidence for chemical reversibility is apparent.

Table 5.2 Peak potentials for process 1 of U_3O_8 at $v = 100$ mV/s in three separate solutions of 0.1 M concentration

Solution	pH	E_p^{red} (V)	E_p^{ox} (V)	$i_p^{\text{red}}/i_p^{\text{ox}}$
MgCl_2	6.5	-0.81	-0.64	0.95
LiCl	7.1	-0.87	-0.67	2.1
NaCl	6.6	-0.87	-0.68	1.5

5.5 VOLTAMMETRY OF $\text{UO}_{2.90}$, $\delta\text{-UO}_3$, and $\gamma\text{-UO}_3$

5.5.1 SHORT TIME DOMAIN EXPERIMENTS IN ELECTROLYTE CONTAINING Mg^{2+}

Scans of $\text{UO}_{2.90}$, $\delta\text{-UO}_3$, and $\gamma\text{-UO}_3$ mechanically transferred to a carbon electrode in 0.1 M MgCl_2 appear in Figure 5.13 where the initial potential was +0.20 V vs. SCE. Peak shapes and potentials for all three compounds are similar to those found for U_3O_8 . A well defined reduction peak at -0.26 V appeared after several cycles in $\text{UO}_{2.90}$, as was the case for U_3O_8 , whereas $\gamma\text{-UO}_3$ displayed a very broad peak around this potential for all scans. No peak was observed at this potential for $\delta\text{-UO}_3$. Apparently, electron transfer and mass transport prior to formation of the insertion compounds can also be observed with the uranium (VI) oxides.

The dependence of peak current (μA) of process 1 at different scan rates (mV/s) was again measured for all three polymorphs of UO_3 , yielding the following equations:

$$i_p(\text{UO}_{2.90}) = 6.94v^{1/2} + 6.12 \quad R^2 = 0.994 \quad (5.11)$$

$$i_p(\delta\text{-UO}_3) = 11.07v^{1/2} - 12.77 \quad R^2 = 0.991 \quad (5.12)$$

$$i_p(\alpha\text{-UO}_3) = 11.25v^{1/2} - 32.44 \quad R^2 = 0.999. \quad (5.13)$$

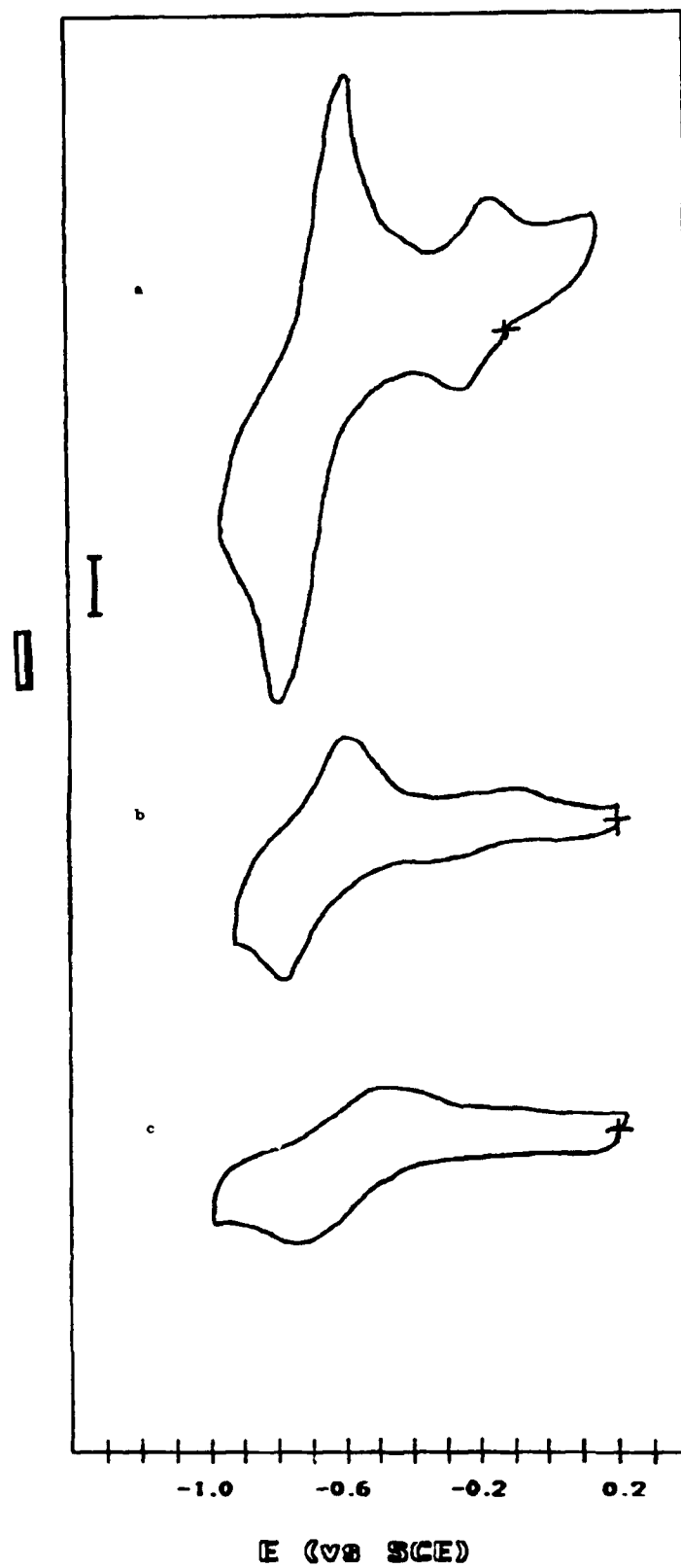


Figure 5.13 Cyclic voltammograms for reduction of uranium oxides at $v = 200$ mV/s and $i = 40$ $\mu\text{A}/\text{unit}$ in 0.1 M MgCl_2 : a) $\text{UO}_{2.90}$, b) $\gamma\text{-UO}_3$, and c) $\delta\text{-UO}_3$

The proportionality of i_p to $v^{1/2}$ again indicates the role of diffusion at the working electrode.

However, as before, stirring the solution has no effect upon peak current or potential (see Table 5.3).

Table 5.3 Cathodic peak currents of process 1 at various stirring rates in 0.1 M $\text{MgCl}_2(\text{aq})$, $v = 200 \text{ mV/s}$

Compound	peak current (μA) stirring rate		
	none	slow	fast
$\text{UO}_{2.90}$	82	80	80
$\delta\text{-UO}_3$	59	61	60
$\gamma\text{-UO}_3$	36	34	34

5.5.2 LONG TIME DOMAIN EXPERIMENTS IN ELECTROLYTE CONTAINING Mg^{2+}

The effect of holding the potential at -1.2 V for a period of time had a much greater impact on the voltammetry of $\text{UO}_{2.90}$ and $\gamma\text{-UO}_3$ than for U_3O_8 and $\delta\text{-UO}_3$ and demonstrates the importance of structural difference of these compounds and the retention of this difference even after mechanical transfer to a carbon electrode. The scans in Figure 5.14 show that in the long time domain mode the major oxidation peak in $\text{UO}_{2.90}$ and $\gamma\text{-UO}_3$ became broader and shifted to much more positive potentials relative to experiments described in the previous section and indeed resemble short time experiments with Na^+ and Li^+ electrolytes. However, unlike the cases of U_3O_8 and $\delta\text{-UO}_3$, with $\text{UO}_{2.90}$ and $\gamma\text{-UO}_3$, repeatedly cycling the potential did not return the voltammograms to their previous shapes and complete irreversibility is retained once the insertion compound is formed. Presumably, again there is a retention of structural difference.

5.6 DISCUSSION

The data presented in this work indicate the reactions at the working electrode surface connected with process 1 for U_3O_8 , $\text{UO}_{2.90}$, $\delta\text{-UO}_3$, and $\gamma\text{-UO}_3$ mechanically transferred to a carbon electrode in Mg^{2+} electrolyte do not display the classical behavior associated with UO_2^{2+} (uranyl ion) solution electrochemistry, as is the case with the solution phase (15-17)



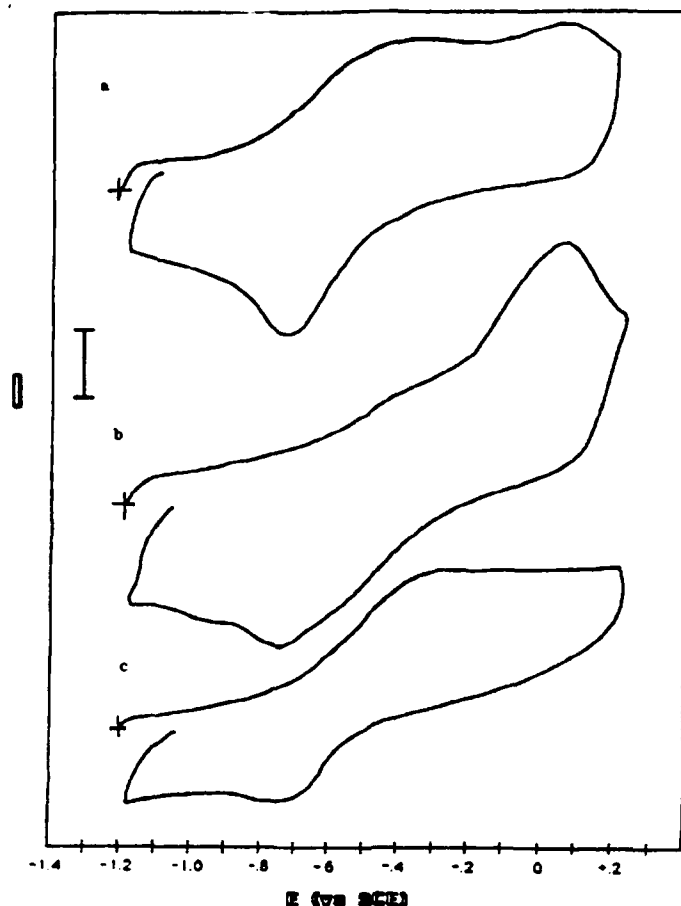


Figure 5.14 Cyclic voltammograms for reduction of uranium oxides at $v = 200$ mV/s and $i = 40$ μ A/unit in 0.1 M MgCl_2 with the initial potential held at -1.2 V for 30 minutes: a) $\gamma\text{-UO}_3$, b) $\text{UO}_{2.90}$ and, c) $\delta\text{-UO}_3$

where diffusion of UO_2^{2+} in the bulk solution is the mass-transport mechanism. The peaks for process 1 (Figures 5.6 and 5.7) are very narrow and symmetric and do not display the skewness associated with an $i = f(t^{-1/2})$ or Cottrellian bulk diffusion model. Stirring the solution to decrease the diffusion layer and modify solution mass transport had no impact on i_p or E_p . However, in all cases, plots of $(i_p^{\text{red}})_1$ were linear functions of $v^{1/2}$, although they do not pass through the origin for reasons previously given. This same linear dependence of i_p vs. $v^{1/2}$ was also observed by Armand et al. (8) for lithium insertion into RuO_2 .

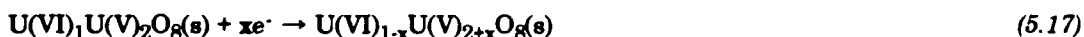
Over the scan rate range of 20 to 500 mV/s, the shape of the voltammogram remains the same. The development of process 2 occurs at ≈ -0.25 V only after reduction of the oxide has occurred and is of unknown origin. Experiments conducted after interruption of cycling for several minutes showed no alteration to process 2 so that the process also is surface confined.

During a U(VI)/U(V) process in the reduction of uranium oxides, in principle, either disproportionation of U(V) to U(VI) and U(IV), structural rearrangement (e.g. equations 5.15 and 5.16), or topochemical reactions (e.g. equations 5.17 and 5.18) occur at the working electrode (17).

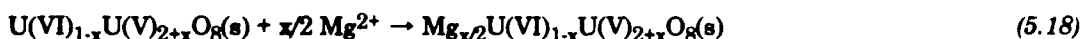


In all other reactions except the topochemical insertion reaction, the parent oxide's crystalline structure is altered. Given the considerable structural rearrangement involved in these reactions, the chemical reversibility is expected to be minimal. However, results with oxides transferred to a carbon electrode with magnesium electrolyte are chemically reversible. Furthermore, the observed dependence of the reaction upon the solution cation and independence of pH (Table 5.1) are inconsistent with disproportionation and the powder X-ray diffraction patterns of products obtained from the chronopotentiometric titration of U_3O_8 with lithium and magnesium (19) to potentials as low as -0.9 V (vs SCE) showed only the orthorhombic structure present and did not lead to structural change, but only insertion of the cation.

All results on mechanically transferred oxides strongly support the occurrence of electron transfer coupled with diffusion in topochemical insertion reactions rather than disproportionation. A mechanism consistent with these observations would be the electron transfer step



coupled with the diffusion step



in which unbound Mg^{2+} contained within or on the surface of the solid becomes specifically associated with the reduced form of the uranium oxide after mass transport by diffusion to the reduced site. Subsequent to mass transport of a sufficient amount of Mg^{2+} by diffusion, the stable insertion compound would be expected to be formed. This additional step required to form the insertion compound would be expected to occur on a long time domain and lead to

incomplete reversibility in the overall process since diffusion would be hindered in a fully occupied lattice.

The diffusing ion has a profound effect for U_3O_8 when comparing the voltammograms for Li^+ , Na^+ , and Mg^{2+} . The effect of cation size is dramatically shown in Figure 5.15 where an attempt was made to insert Cs^+ (ionic radius = 1.69 Å) into U_3O_8 . The lack of an electrochemical response suggests Cs^+ is too large for insertion. With Mg^{2+} , the diffusion and insertion processes appear to be time resolved, probably because the diffusion is slower and occurs over a longer time domain. Such differences in behavior may be due to the variations in ion size and charge. Vacarro et al. (4) obtained significantly different values for the chemical diffusion coefficient for lithium (D_{Li}) in TiS_2 when various solvents and electrolytes were used. They suggested that the measured D_{Li} is of the solvated ion. However, infrared analysis of cathodic products from the cell $\text{Mg(s)}/\text{MgCl}_2(\text{aq})/\text{U}_3\text{O}_8(\text{s})$ did not show the co-insertion of water molecules with Mg^{2+} (19).

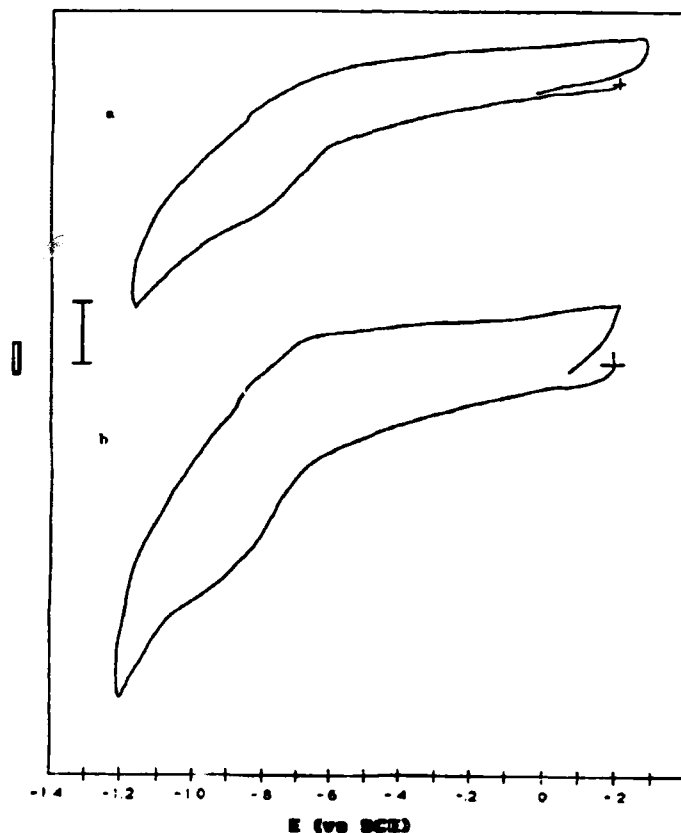


Figure 5.15 Cyclic voltammograms for reduction of U_3O_8 in 0.1 M CsCl , $i = 20 \mu\text{A}/\text{unit}$: a) $v = 100 \text{ mV/s}$ and b) $v = 200 \text{ mV/s}$

The effect of metal oxide quantity and distribution on voltammogram clarity can best be explained in terms of a model developed for ion insertion into TiS_2 (20). In this model an inserting ion's solid-state diffusion path is assumed to be no greater than the average particle diameter (i.e. no inter-particle transport); and therefore, the active particles of the material are only those in contact with the liquid electrolyte. If the same assumption is made for the uranium oxides, then ion insertion is dependent upon the surface area of active material on the electrode. It follows then that the electrochemical response will be a function of uranium oxide surface area on the electrode with the best response obtained when this is maximized.

Increasing the Mg^{2+} concentration in solution produces a positive shift in peak potentials (Table 5.1). Gregory et al. (21) also found the Mg^{2+} solution concentration to be important in chronopotentiometric studies of various metal oxide and sulfide insertions. Similarly, holding the potential at -1.2 V leads to a shift to less negative potentials and is consistent with an effective increase in Mg^{2+} concentration. Reichman et al. (3) and Vacarro et al. (4) concluded in their studies of WO_3 and TiS_2 that the rate-determining step is not ionic transport within the bulk solution, but rather ionic transport within the bulk solid. Diffusion coefficients in the solid phase generally are on the order of 10^6 times smaller than in the liquid phase, so that the diffusion process may only occur from the surface to a short distance within the arrays of material dispersed across the carbon surface.

The similarity in the diffusion component of voltammograms of U_3O_8 , $\text{UO}_{2.90}$, $\delta\text{-UO}_3$ and $\gamma\text{-UO}_3$ in 0.1 M MgCl_2 as deduced from short time frame experiments is consistent with common structural features. The short time domain voltammograms of structurally similar U_3O_8 and $\text{UO}_{2.90}$ are practically superimposable even including the appearance of process 2. Thus, at least two new phases, each maintaining the host metal-oxide's lattice, are formed during cycling in these two compounds. Chronopotentiometric studies of aqueous lithium and magnesium (19) insertion into U_3O_8 also showed the presence of at least two new solid phases isostructural with the host oxide. However, differences in the insertion compounds are observed on long time scale experiments achieved by holding the potential at -1.2 V. In

this case, insertion of Mg^{2+} was found to be reversible with U_3O_8 and $\delta\text{-UO}_3$, but not with the structures of $\text{UO}_{2.90}$ and $\gamma\text{-UO}_3$, at least on the hours time scale.

REFERENCES

1. A. J. Bard and L. R. Faulkner, Electrochemical Methods, John Wiley & Sons, New York, (1980).
2. Southampton Electrochemical Group, Instrumental Methods in Electrochemistry, Ellis Horwood, London, (1990).
3. B. Reichman, A. J. Bard and D. J. Laser, *J. Electrochem. Soc.*, **127**, 3, 647, (1980).
4. A. J. Vaccaro, T. Palanisamy, R. L. Kerr, and J. T. Maloy, *J. Electrochem. Soc.*, **129**, 4, 677, (1982).
5. J. P. Pereira-Ramos, R. Messina, and J. Perichon, *J. App. Elec.*, **16**, 379, (1986).
6. J. P. Pereira-Ramos, R. Messina, and J. Perichon, *J. Electroanal. Chem.*, **218**, 241, (1987).
7. A. Hardwick, D.Phil. Thesis, Oxford University, (1982).
8. M. Armand, F. Dalard, D. Deroo, and C. Mouliom, *Sol. State Ion.*, **15**, 205, (1985).
9. P. Novák and J. Desilvestro, *J. Electrochem. Soc.*, **140**, 1, 141, (1993).
10. F. Scholz, L. Nitschke, G. Henrion, and F. Damaschun, *Fresenius Z. Anal. Chem.*, **335**, 189, (1989).
11. F. Scholz, L. Nitschke, and G. Henrion, *Electroanalysis* (N.Y.), **2**, 85, (1990).
12. A. M. Bond, A. Bobrowski, and F. Scholz, *J. Chem. Soc., Dalton Trans.*, 411, (1991).
13. A. M. Bond and F. Scholz, *Langmuir*, **7**, 3197, (1991).
14. A. M. Bond and F. Scholz, *J. Phy. Chem.*, **95**, 19, 7460, (1991).
15. W. E. Harris and I. M. Kolthoff, *J. Am. Chem. Soc.*, **67**, 1484, (1945).
16. I. M. Kolthoff and W. E. Harris, *J. Am. Chem. Soc.*, **68**, 1175, (1946).
17. W. E. Harris and I. M. Kolthoff, *J. Am. Chem. Soc.*, **69**, 446, (1947).
18. M. S. Whittingham, *J. Electrochem. Soc.*, **123**, 3, 315, (1976).
19. J. M. Fleetwood, Chemistry Part II Thesis, Oxford, (1990).
20. A. J. Vaccaro, T. Palanisamy, R. L. Kerr, and J. T. Maloy, *J. Electrochem. Soc.*, **129**, 4, 682, (1982).
21. T. D. Gregory, R. J. Hoffman, and R. C. Winterton, *J. Electrochem. Soc.*, **137**, 3, 775, (1990).

CHAPTER 6 MAGNETIC PROPERTIES

The magnetic properties of UO_2 , U_3O_8 , and $\delta\text{-UO}_2$ and their insertion compounds were studied in order to obtain information about their electronic structure. This was achieved by measurement over a wide temperature range of magnetic susceptibility and a subsequent comparison of measured values with those obtained using model systems which take into account the environment of the magnetic species involved and the extent of insertion. The necessary theory and experimental technique underlying this approach are discussed below. The definitions of magnetic quantities and their units used here are given in the SI system (1-3).

6.1 MACROSCOPIC QUANTITIES

The magnetic induction, B (T), within a material situated in a magnetic field is given by the equation

$$B = B_0 + \mu_0 M \quad (6.1)$$

where B_0 is the magnetic induction in free space, M is the magnetization per unit volume, and μ_0 ($4\pi \times 10^{-7} \text{ H m}^{-1}$) is the permeability of free space. In free space, $B = B_0 = \mu_0 H$ where H (A m^{-1}) is the magnetic field.

From these primary quantities are derived the volume magnetic susceptibility, χ (dimensionless),

$$\chi = M/H = \mu_0 M/B_0 \quad (6.2)$$

and the molar magnetic susceptibility, χ'_{mol} ($\text{m}^3 \text{ mol}^{-1}$),

$$\chi'_{\text{mol}} = \chi(\text{RMM})/10^3 \rho \quad (6.3)$$

where ρ is the density and RMM the relative molecular mass.

The experimental quantity measured in this work using a SQUID susceptometer is the magnetic moment, m (A m^2), of the sample:

$$m = MV \quad (6.4)$$

where V is the volume. The relationship between m and χ'_{mol} is

$$\chi'_{\text{mol}} = \mu_0 m/B_0 n \quad (6.5)$$

where n is the number of moles of sample.

For comparison of data given in the alternative cgs/emu system use is made of the conversion

$$\chi'_{\text{mol}} (\text{SI}) = 4\pi \times 10^{-6} \chi'_{\text{mol}} (\text{cgs}). \quad (6.6)$$

Magnetization is negative in diamagnetic materials and positive in paramagnetic materials. In general, $B = \mu H$ where μ is the permeability of the material. Permeability is constant over a wide range of values of H for diamagnetic and paramagnetic materials, but varies strongly with H for ferromagnetic materials (2).

The measured quantity related to theoretical values for appropriate models is the molar paramagnetic susceptibility χ_{mol} . This quantity is obtained from the total magnetic susceptibility of the sample by subtracting a correction for the diamagnetic susceptibility arising from filled electron shells (2).

$$\chi_{\text{mol}} = \chi'_{\text{mol}} - \chi_{\text{diamagnetic}} \quad (6.7)$$

In general χ is a tensor quantity, but for powders only the average susceptibility, $\langle \chi \rangle$, can be measured:

$$\langle \chi \rangle = (\chi_{||} + 2\chi_{\perp})/3 \quad (6.8)$$

where $\chi_{||}$ and χ_{\perp} are the susceptibilities measured parallel and perpendicular to the principal crystal axis.

6.2 MEASUREMENT OF MAGNETIZATION

Magnetization of a specimen can be measured by induction methods, force methods, or the dipole moment method. Of the induction methods, the vibrating sample magnetometer is the most favored with a magnetic moment sensitivity approaching $5 \times 10^{-8} \text{ A m}^2$. Force methods, which use the Guoy and Faraday balances, have maximum sensitivities of 10^{-9} A m^2 . The greatest sensitivity ($< 10^{-10} \text{ A m}^2$), however, is achieved using a superconducting quantum interference device or SQUID (4).

6.2.1 PRINCIPLES OF OPERATION - SQUID

Superconductors cooled below their transition temperature expel all flux (i.e. Meissner effect) and behave as perfect diamagnets. However, shaping them into the form of a ring leads to flux being trapped within the ring upon cooling below the transition temperature. This flux (ϕ) is quantized and can be represented by the equation:

$$\phi = k\phi_0$$

(6.9)

where k is an integer and ϕ_0 is one flux quantum ($h/2e = 2 \times 10^{-15}$ Wb). The presence of a magnetic field normal to the plane of the superconducting ring produces an external flux (ϕ_x) which causes an opposing screening current (I_s) to flow. Equation 6.9 is modified to read

$$\phi_x + LI_s = k\phi_0$$

(6.10)

where L is the self-inductance of the ring.

Measuring ϕ_x by monitoring I_s requires a weak link or Josephson junction be introduced into the superconducting ring (Figure 6.1). Josephson (5) showed that in the absence of an applied potential the supercurrent flowing through a weak link could be expressed as

$$I_s = I_c \sin \Delta\theta$$

(6.11)

where I_c is the critical current and $\Delta\theta$ is the phase change in the superconducting wave function across the junction.

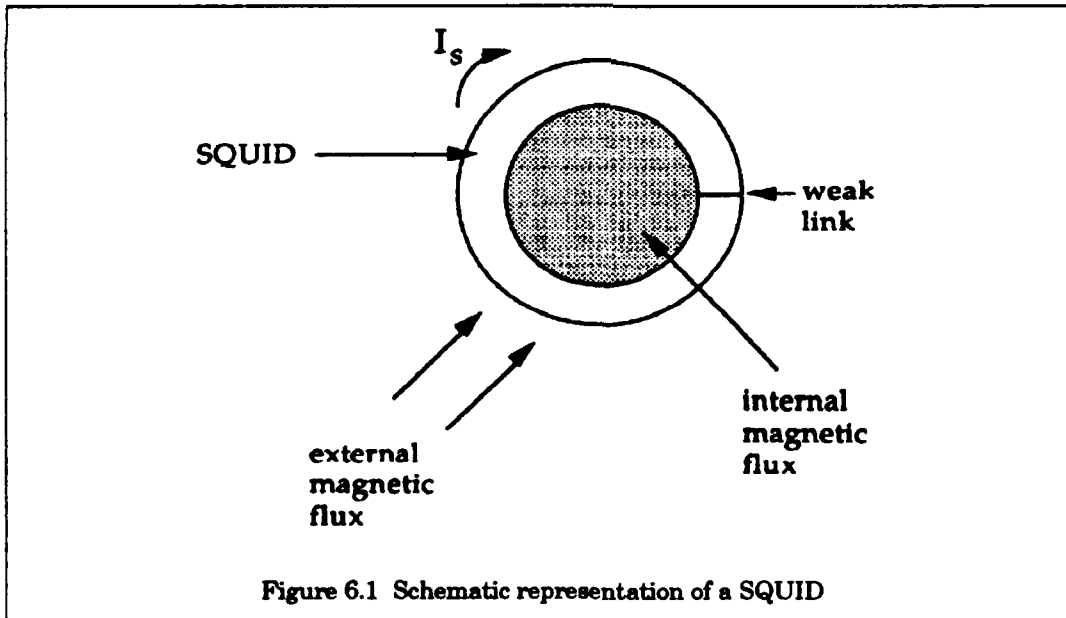


Figure 6.1 Schematic representation of a SQUID

The response of the ring with a weak link to an applied magnetic flux is shown in Figure 6.2. Starting at the origin O (for $k = 0$), a steadily increasing external flux, ϕ_x , will cause the SQUID to traverse the path OA , the circulating current growing from zero to I_c (point A) which represents the maximum superconducting current the weak link can sustain ($\approx 10 \mu A$). If the process is continued, the SQUID must undergo a transition to a different k .

state, and it is in the successful control of this process that the basis of SQUID magnetometry lies. By careful design of the weak link a fairly rigorous 'selection rule' of $\Delta k = \pm 1$ can be established, and with increasing external flux, the circulating current follows the path OABZY etc. Conversely, if after the first transition at A the flux is reduced, the loop can be made to undergo a further transition at C and follow the path OABCD, describing a hysteresis loop. Monitoring changes in I_s using a radio frequency tank circuit enables ϕ_x , and ultimately the magnetic moment, to be determined (4).

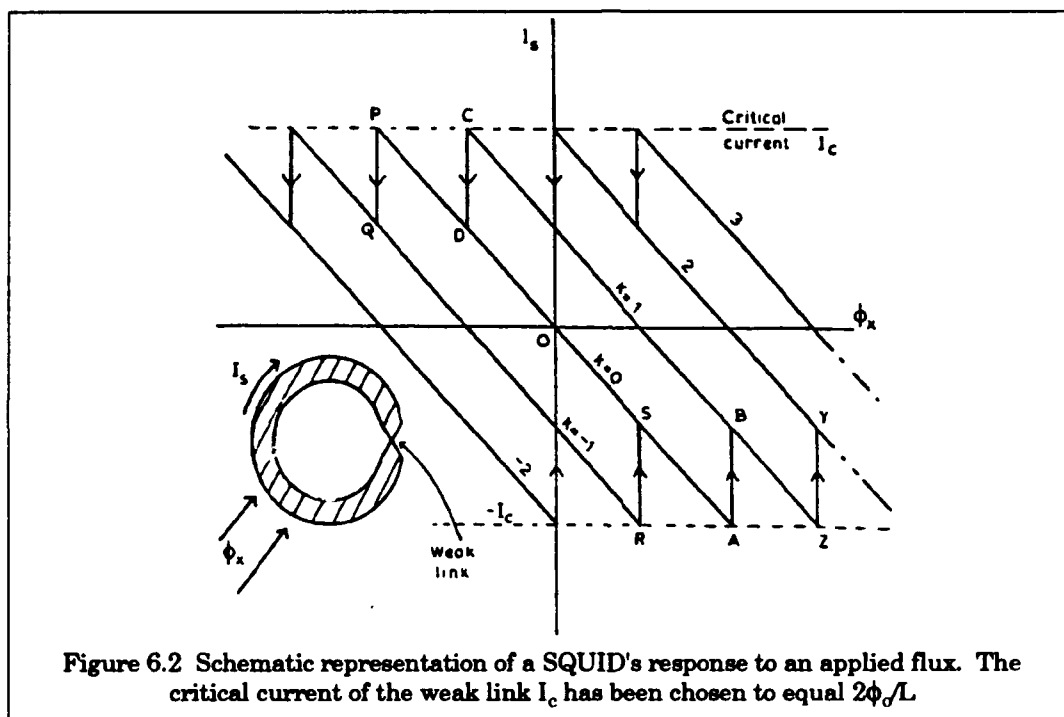
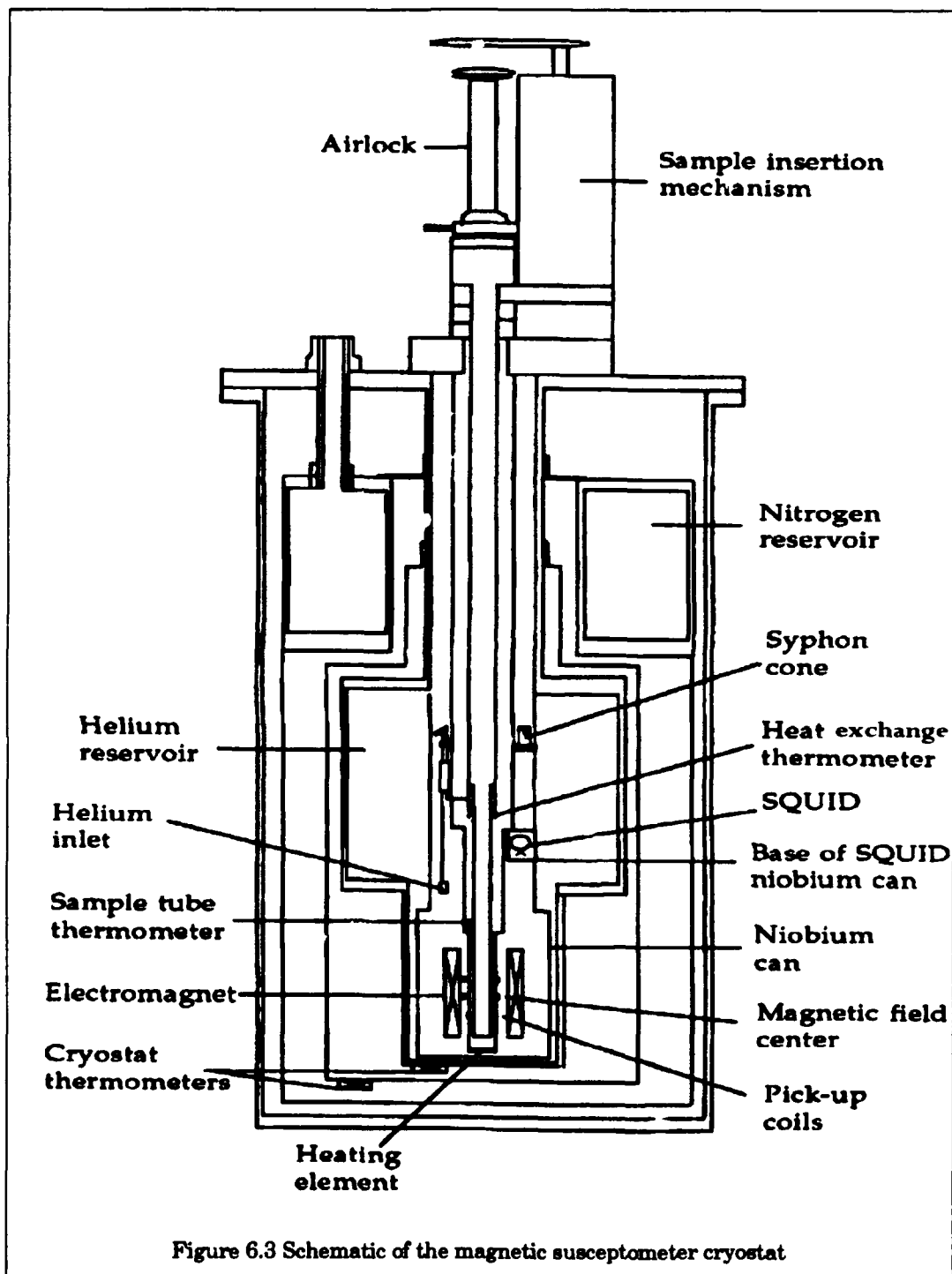


Figure 6.2 Schematic representation of a SQUID's response to an applied flux. The critical current of the weak link I_c has been chosen to equal $2\phi_0/L$.

6.2.2 THE SQUID SUSCEPTOMETER

Figure 6.3 is a schematic of the cryostat which contains the SQUID, magnet, and sample chamber. Although using an unshielded SQUID to directly observe magnetic field fluctuations is possible, it is advantageous to shield the SQUID inside a superconducting niobium can and couple it to a flux transformer. Such an arrangement keeps the SQUID at a constant 4.2 K and shields it from magnetic fields. The flux transformer consists of a pair of counter-wound pick-up coils situated in the sample chamber which connect to an input coil at the SQUID. Flux changes at the pick-up coils cause equal but opposite changes at the input

coil. Balancing the pick-up coils enables the SQUID to sense only changes in magnetic flux occurring when a sample is introduced into the uniform magnetic field.



The sample itself is contained in a quartz bucket attached by PTFE tape to one end of a 10 cm strand of diamagnetic copper wire. A stainless steel rod 1.2 m in length is

Chapter 6 Magnetism

attached to the other end. A synchronous motor drives the sample through the two pick-up coils with the signal output to a computer for conversion to a magnetic moment value (in A m²).

6.2.3 EXPERIMENTAL

Powder samples of 50 - 130 mg were cooled to 6 K in a 0 T field over a period of several hours. Magnetic field dependence measurements were made at this temperature before recording the magnetization at 5 K or 10 K intervals up to 296 K. The moment measured was the raw moment, m_{raw} , in SI units. The moment of the standard small quartz bucket used was found to be constant with temperature and linear with field. The correction factor, C-factor, was obtained using the relationship

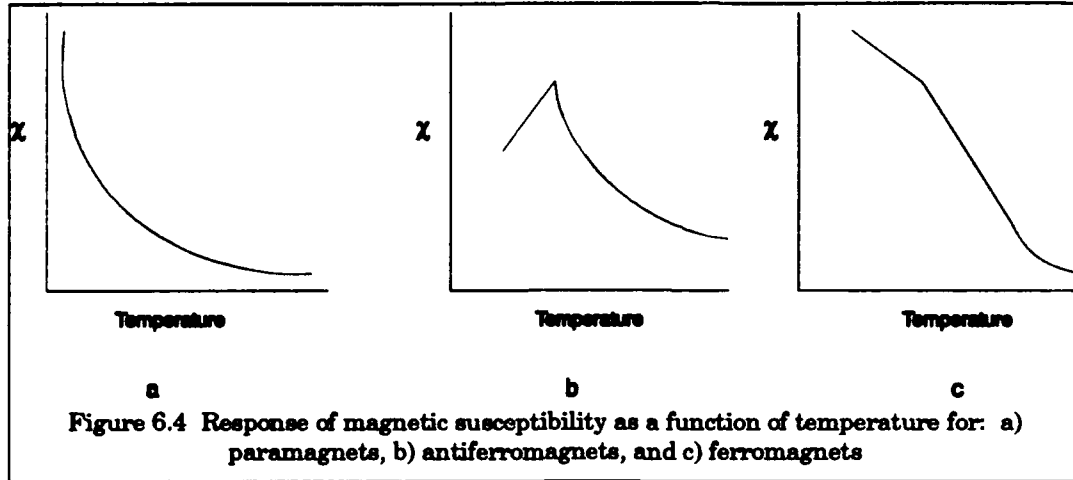
$$\text{C-factor} = [-3.085 \times 10^{-3}][\text{bucket mass (kg)}][\text{field (T)}]. \quad (6.12)$$

with $m = m_{\text{raw}} - \text{C-factor}$. Measurements were lastly corrected for intrinsic diamagnetism of the samples using Pascal's constants (6).

6.3 THEORETICAL BACKGROUND AND MODEL SYSTEMS

In solid metal oxides paramagnetic metal cations are separated by diamagnetic oxygen anions, resulting in two extreme types of magnetic behavior. If the paramagnetic ions do not interact significantly the sample is described as magnetically dilute and the susceptibility is independent of the magnetic field and follows a Curie law ($\chi = C/T$) or shows Langevin-Debye behavior ($\chi = C/T + A$). From the parameters C and A information about the electronic structures of the individual metal ions can be deduced.

On the other hand, if the magnetic ions interact strongly with each other, varying types of collective magnetic behavior result of which the most important are antiferromagnetism and ferromagnetism. Phenomenologically a Curie-Weiss law ($\chi = C/(T - \Theta)$) is often obeyed; however, relating the observed parameters to features of the ion's electronic structure is difficult without further information (7). Behavior of χ vs. T for the systems commonly encountered are shown in Figure 6.4.



6.3.1 MAGNETICALLY DILUTE SYSTEM

For a solid composed of N identical noninteracting magnetic species (ions or atoms with partially filled electronic shells) the total magnetic moment of the sample is $\mu = N\mu_{\text{avg}}$ where μ_{avg} is the mean atomic magnetic moment obtained by thermally averaging over the atom's available electronic energy levels, E_i . The dependence of the electronic energy levels on the applied magnetic field in a particular direction is given by

$$E_i = W_i^{(0)} + W_i^{(1)}B + W_i^{(2)}B^2 + \dots \quad (6.13)$$

where $W_i^{(0)}$ is the energy of the unperturbed i th state and W_i are the Zeeman coefficients.

The magnetic moment associated with the i th state is $\mu_i = -\partial E_i / \partial B_0$ and the total magnetic moment of the sample in the direction of the applied field is

$$\mu = N \sum_i (-\partial E_i / \partial B_0) \exp(-E_i/kT) / \sum_i \exp(-E_i/kT). \quad (6.14)$$

Provided that separation between levels within the ground state is small and separation between the ground state and the next excited state is large, both compared with kT , then the susceptibility is given by the van Vleck formula (8)

$$\chi = N \sum_i (W_i^{(1)2}/kT - 2W_i^{(2)}) \exp(-W_i^{(0)}/kT) / \sum_i \exp(-W_i^{(0)}/kT). \quad (6.15)$$

Three important simplifying situations lead to special forms of equation 6.15:

(1) if in zero field there is only one, n -fold degenerate energy level, then $W_i^{(2)} = 0$ and

$$\chi = [N \sum_i W_i^{(1)2}/kT]/n = C/T \quad (\text{Curie law}) \quad (6.16)$$

(2) if the ground term is nondegenerate with at least one degenerate excited state at $E_i \gg$

kT , then as a consequence $W_i^{(1)} = 0$ and for all excited states $\exp(-W_i^{(0)}/kT) = 0$, and therefore

$$\chi = N \sum_i W_i^{(2)} = N\alpha \quad (6.17)$$

Chapter 6 Magnetism

(3) if the ground state is degenerate and all excited states are at $E_i \gg kT$ above the ground state, then (1) and (2) are combined to yield

$$\chi = C/T + N\alpha = C/T + A \quad (\text{Langevin-Debye law}). \quad (6.18)$$

This is a real situation and can often be observed in transition metal complexes with symmetry O_h or T_d where the ground term possesses A or E symmetry. In this situation, the excited state is $\gg kT$ above the ground state and the ground state is not split by spin-orbit coupling to create a low lying excited state (7).

In order to calculate χ it is necessary to evaluate the first and second order Zeeman coefficients, $W_i^{(1)}$ and $W_i^{(2)}$ using quantum mechanical perturbation theory (7). The

Hamiltonian for the interaction of the magnetic field with the atomic moment is of the form

$$H = (L + 2S)\mu_B B \quad (6.19)$$

where L and S represent the orbital and spin angular momentum operators and μ_B is the Bohr magneton. Its application leads to the expressions used to calculate the z-axis component of χ in equation 6.15 with similar expressions for the other components

$$W_i^{(1)} = \mu_B \langle \psi_i | L_z + 2S_z | \psi_i \rangle \quad (6.20)$$

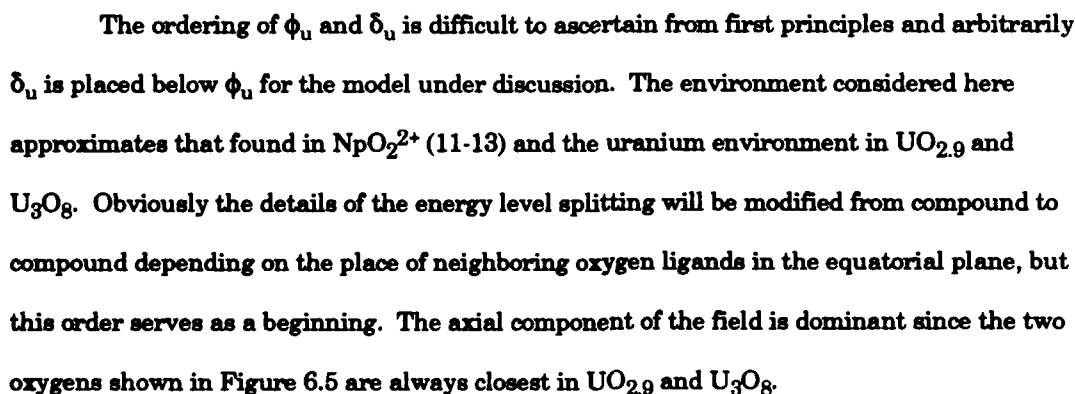
$$W_i^{(2)} = \mu_B^2 \sum \langle \psi_i | L_z + 2S_z | \psi_j \rangle \langle \psi_j | L_z + 2S_z | \psi_i \rangle (W_i^{(0)} - W_j^{(0)}) \quad (6.21)$$

where ψ_i and ψ_j are the electronic wave functions.

In order to illustrate the application of the expressions so far developed to the calculation of the molar magnetic susceptibility of an array of non-interacting magnetic ions the behavior of the f^1 ion U(V) consecutively subjected to a $D_{\infty h}$ crystal field, spin-orbit coupling, and a weak magnetic field is analyzed. Results for a crystal field of O_h symmetry are then summarily presented.

6.3.1.1 $D_{\infty h}$ (UO_2 and U_3O_8)

In the presence of a field of cylindrical symmetry ($D_{\infty h}$) along the z-direction the seven-fold degeneracy of the free ion 2F state is split into states characterized by their m_l values (Figure 6.5) The pattern of levels and their order follow from simple crystal field or covalent model considerations (9,10). In a covalent model, the σ_u and π_u combinations of the oxygen 2s and 2p orbitals will interact with the σ_u and π_u f-orbitals, raising the energy of the latter with σ above π . No oxygen orbitals possess δ_u or ϕ_u symmetry, so the δ_u and ϕ_u f-



The zero order wave functions corresponding to the field split levels shown in Figure 6.5 are listed in the Appendix C with the labels ($|m_l, m_s\rangle$): $\phi_1 = |-3, 1/2\rangle, \dots, \phi_3 = |-2, 1/2\rangle, \dots, \phi_5 = |1, 1/2\rangle, \dots, \phi_{13} = |0, 1/2\rangle, \dots$. Spin-orbit coupling introduces a term $H = \lambda L \cdot S$ into the Hamiltonian for the f^1 atom where λ is the spin-orbit coupling constant. The effect of the perturbation transforms the original spin-orbitals ϕ_k into a new basis set ψ_i such that $\psi = \sum_i c_i \phi_i$. The perturbed energy levels E_i and the coefficients c_i are obtained by solving the matrix equation $Hc = Ec$ where H is the square matrix with elements $H_{ij} = \langle \phi_i | \lambda L \cdot S | \phi_j \rangle$.

and c is the column vector with elements c_j . E is a diagonal matrix whose elements (eigenvalues) are the energy of the perturbed system. The only off-diagonal elements of H arise from coupling of states ϕ_i, ϕ_j with the same m_j value.

The combined effect of axial ligand field and spin-orbit coupling is shown in Figure 6.6 with the expressions for the wavefunctions and energies given in Appendix C. The resulting energy levels are Kramers doublets and the states are classified by m_j values. For NpO_2^{2+} , $\lambda \approx 2,000 \text{ cm}^{-1}$ and $\Delta_1 - \Delta_3$ values are in the range $1,000 - 40,000 \text{ cm}^{-1}$ (13). Similar values are anticipated for U(V) in the environment postulated in the model.

The final perturbation due to interaction between the magnetic field B_0 and the spin and orbital momenta is much smaller ($\approx 1 \text{ cm}^{-1}$ at 1 T) than that for the ligand field and spin-orbit coupling. Therefore, the approach to be adopted in which the new wave functions are used as the basis set for the extra perturbing term

$$h = \mu_B(L + 2S)B_0 \quad (6.22)$$

is justified. Again new perturbed energies are obtained by solving a matrix equation $ha = Ea$ where the matrix elements of h are $h_{ij} = \langle \psi_i | \mu_B(L + 2S)B_0 | \psi_j \rangle$. The elements h_{ij} are required to calculate the value of χ_{mol} in equation 6.15 where

$$W_i^{(1)} = \mu_B h_{ii} \text{ and } W_i^{(2)} = \mu_B^2 \sum_j h_{ij} h_{ji} / (W_i^{(0)} - W_j^{(0)}). \quad (6.23)$$

Expressions for the first and second order Zeeman coefficients for the z -direction are included in Appendix C. A complete listing for those in the x - and y -directions is given elsewhere (14).

To illustrate the use of these formulas to obtain an approximate result which can be related to experiment, a typical case is examined. If the ground state in $D_{\infty h}$ arises from δ_u ($m_l = \pm 2$) which after the spin-orbit coupling becomes $\Delta_{3/2u}$ in Figure 6.6, and this state is much lower in energy than the excited states, the corresponding ground state wave functions are $|2, -1/2\rangle$ and $|-2, 1/2\rangle$ with no orbital admixture with other states. Evaluation of the elements $\langle \psi_i | \mu_B(L + 2S)B_0 | \psi_j \rangle$ $ij = 1, 2$ leads to the results shown below

E_i	$W_i^{(1)}(z)/\mu_B$	$W_i^{(1)}(x,y)/\mu_B$	$W_i^{(2)}(z)/\mu_B^2$	$W_i^{(2)}(x,y)/\mu_B^2$
$E_1 = E_2$	± 1	0	0	0

Chapter 6 Magnetism

The components of χ_z , χ_x , χ_y , and $\langle\chi_{\text{mol}}\rangle$ are given by: $\chi_z = N\mu_B^2/kT$, $\chi_x = 0$, $\chi_y = 0$, and $\langle\chi_{\text{mol}}\rangle = N\mu_B^2/3kT$. It is conventional to define an effective magnetic moment, μ_{eff} , in the equation

$$\chi_{\text{mol}} = N\mu_B^2\langle g^2 \rangle / 4kT = N\mu_B^2\mu_{\text{eff}}^2 / 3kT = C/T \quad (6.24)$$

where g is the spectroscopic splitting factor. Comparison with equation 6.24 shows that $\mu_{\text{eff}} = 1$ for the case discussed and this quantity should be independent of temperature. This value should be compared with the spin-only value of $1.73 \mu_B$ and the free ion value of $2.54 \mu_B$ for the isolated f^1 ion.

The effect of lowering $D_{\infty h}$ symmetry is to split δ_u levels leading to a quenching of the orbital contribution to the moment associated with the ground state (14). A final calculated moment of $\mu = 0.6 - 1 \mu_B$ is obtained for typical separations of δ_u levels of a few hundred cm^{-1} .

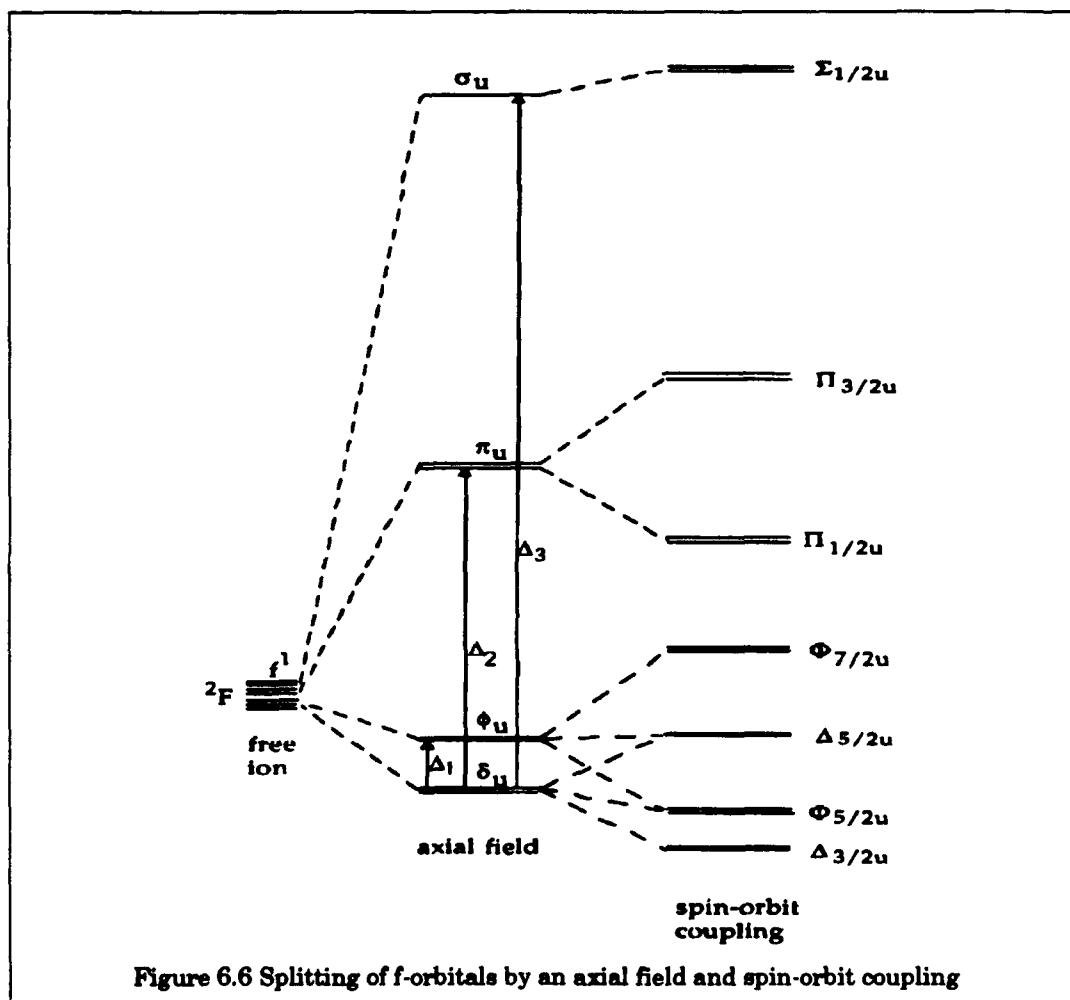


Figure 6.6 Splitting of f-orbitals by an axial field and spin-orbit coupling

6.3.1.2 O_h (δ - Li_xUO_3)

Ambient-temperature δ - Li_xUO_3 has the same basic perovskite structure as the high temperature alkali monouranates (15) with U(V) octahedrally coordinated to six oxygens and the alkali-metal occupying the body center position. Theoretical studies of a single 5f electron in an octahedral field have been reported (16-20). Figure 6.7 shows the splitting of the seven-fold degenerate energy state of the f-orbitals by the octahedral field and spin-orbit coupling. Using the representation of the octahedral crystal field (O_h), the f-orbitals are split into the A_2 , T_2 , and T_1 states with Δ and Θ the energy separations. The A_2 orbital points towards the corners of a cube and is furthest from the negatively charged ligands; therefore, it has the lowest energy. T_2 orbitals are next highest in energy as they point towards the centers of the edges of the cube. T_1 orbitals are highest in energy as they point directly at the ligands (19). Considering only s- and p-orbitals on the ligands; A_2 is nonbonding, T_2 are π -bonding, and T_1 are σ - and π -bonding. Expressions for these states in their real form are (21):

$$A_2 = \frac{1}{2i}\sqrt{5}(|-2\rangle - |2\rangle) \quad (6.25)$$

$$T_2 = \frac{1}{4}\{\sqrt{5}|1\rangle - \sqrt{5}|-1\rangle + \sqrt{3}|3\rangle - \sqrt{3}|-3\rangle\} \\ \frac{1}{4i}\{\sqrt{5}|1\rangle + \sqrt{5}|-1\rangle - \sqrt{3}|3\rangle - \sqrt{3}|-3\rangle\} \\ \frac{1}{2}\sqrt{5}(|2\rangle + |-2\rangle) \quad (6.26)$$

$$T_1 = \frac{1}{4}\{\sqrt{3}|1\rangle - \sqrt{3}|-1\rangle - \sqrt{5}|3\rangle + \sqrt{5}|-3\rangle\} \\ \frac{1}{4}\{\sqrt{3}|1\rangle + \sqrt{3}|-1\rangle + \sqrt{5}|3\rangle + \sqrt{5}|-3\rangle\} \\ |0\rangle \quad (6.27)$$

The combined effects of O_h ligand field and spin-orbit coupling is to transform or split the A_2 , T_2 , and T_1 levels into spin-orbit levels which span representations of the double group O' (22); these are $E_{5/2}(a_2)$, $G_{3/2}(t_2)$, $E_{5/2}(t_2)$, $G_{3/2}(t_1)$, and $E_{1/2}(t_1)$ respectively (Figure 6.7). The ground state doublet $E_{5/2}$ arises from a mixture of the A_2 and T_2 states and the first excited state quartet $G_{3/2}$ from a mixture of T_2 and T_1 . The energy matrices for $E_{1/2}$, $E_{5/2}$, and $G_{3/2}$ are (23)

$$E_{1/2}: |\Delta - \Theta + 1.5\lambda|$$

$$G_{3/2}: \begin{vmatrix} \Delta + 0.25\lambda & 1.68\lambda \\ 1.68\lambda & \Delta + \Theta - 1.5\lambda \end{vmatrix}$$

$$E_{5/2}: \begin{vmatrix} 0 & 1.73\lambda \\ 1.73\lambda & \Delta - 0.5\lambda \end{vmatrix}$$

Chapter 6 Magnetism

The wavefunctions produced from the diagonalization of the $E_{5/2}$ matrix are

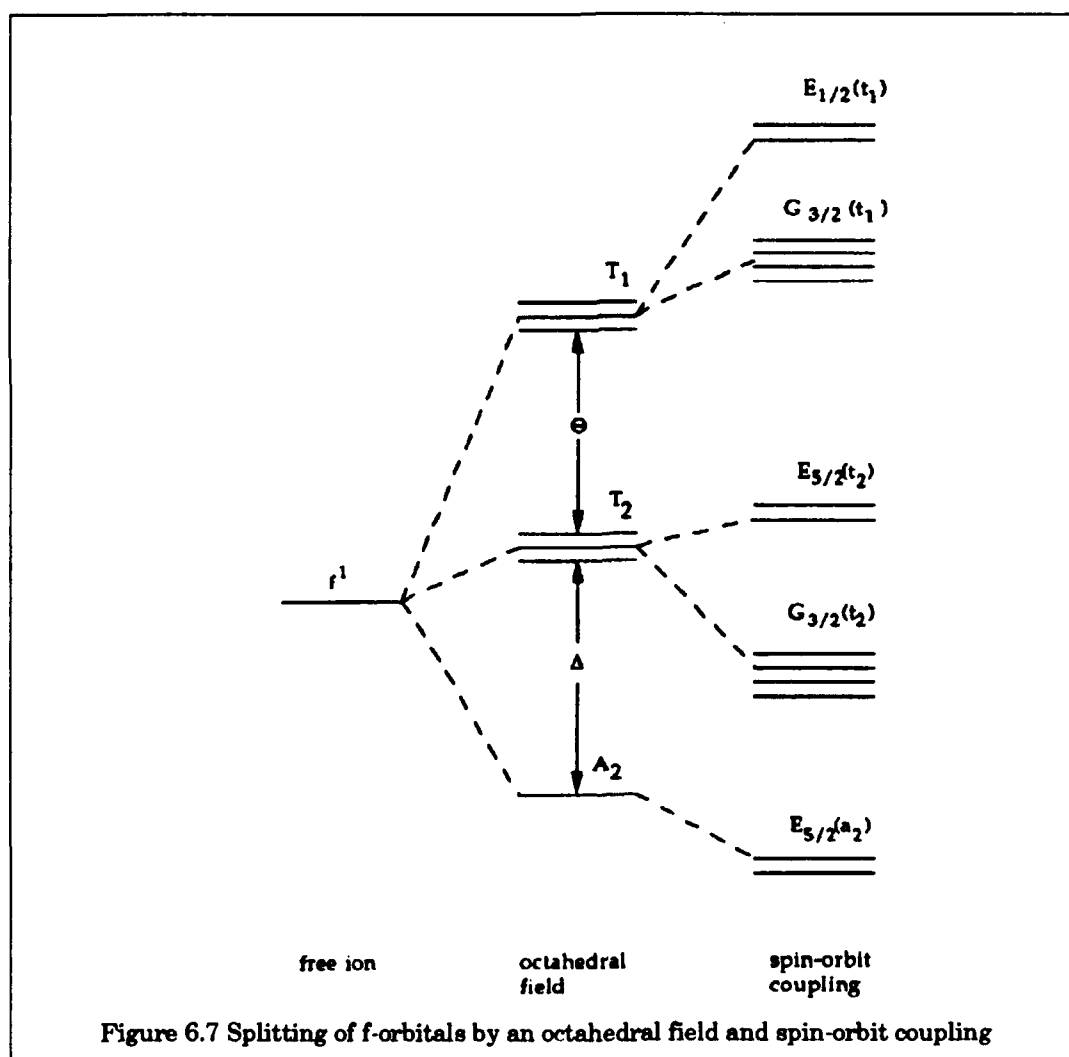
$$|E_{5/2}\rangle = x|E_{5/2}(a_2)\rangle - y|E_{5/2}(t_2)\rangle \quad (6.28)$$

$$|E'_{5/2}\rangle = y|E_{5/2}(a_2)\rangle + x|E_{5/2}(t_2)\rangle \quad (6.29)$$

where x and y are the normalized mixing coefficients and $|E_{5/2}\rangle$ and $|E'_{5/2}\rangle$ are the symmetry adapted basis set spin-orbitals. Similarly, diagonalization of the $G_{3/2}$ matrix produces the two levels $|G_{3/2}\rangle$ and $|G'_{3/2}\rangle$ (23).

$$|G_{3/2}\rangle = x'|G_{3/2}(t_2)\rangle - y'|G_{3/2}(t_1)\rangle \quad (6.30)$$

$$|G'_{3/2}\rangle = y'|G_{3/2}(t_2)\rangle + x'|G_{3/2}(t_1)\rangle \quad (6.31)$$



Provided that when compared to kT the separation of levels within the ground state is small and the energy of the first excited state is large, the susceptibility is determined by

equation 6.15, leading to the form $\chi = C/T + A$. Eisenstein and Pryce (16) give the expressions for C and A as

$$C = (N\mu_B^2/2k) \sum | \langle E_{5/2} | L_z + 2S_z | E_{5/2} \rangle |^2. \quad (6.32)$$

$$A = 2N\mu_B^2 [\langle E_{5/2}(t_2) | L_z + 2S_z | E_{5/2}(a_2) \rangle^2 / (W^{(0)}E_{5/2}(t_2) - W^{(0)}E_{5/2}(a_2)) + \\ \langle G_{3/2}(t_2) | L_z + 2S_z | E_{5/2}(a_2) \rangle^2 / (W^{(0)}G_{3/2}(t_2) - W^{(0)}E_{5/2}(a_2)) + \\ \langle G_{3/2}(t_1) | L_z + 2S_z | E_{5/2}(a_2) \rangle^2 / (W^{(0)}G_{3/2}(t_1) - W^{(0)}E_{5/2}(a_2))] \quad (6.33)$$

Applying the magnetic moment operator gives the expression for C as a function of x and y

$$C = N\mu_B^2/kT [x^2 - (4/\sqrt{3})xy]^2 \quad (6.34)$$

where x and y are functions of the spectral parameters Δ and λ .

$$2xy/(x^2 - y^2) = 2\sqrt{3}/(\Delta/\lambda - 0.5) \quad (6.35)$$

Similar expressions for A as a function of Δ , θ , and λ are reported elsewhere (23).

6.3.2 MAGNETICALLY CONCENTRATED SYSTEMS - EXCHANGE COUPLING

In a magnetically dilute system, the Hamiltonian describing the interaction between the magnetic field and the magnetic moments of the *i*th magnetic species it contains is composed only of single ion terms.

$$H = \mu_B B_0 \sum_i (L_i + 2S_i) \quad (6.36)$$

The average atomic moment μ_{avg} is obtained by thermal averaging over the energy levels of the individual ions. As a consequence of this as $T \rightarrow 0$, $\chi \rightarrow \infty$ and μ_{avg} reaches a constant value.

To account for the significant interaction between the ions arising from the presence of partially filled shells and to reproduce the experimentally observed magnetic behavior over a wide temperature range it is necessary to include in the complete Hamiltonian for the system the additional term for magnetic exchange (due to Heisenberg and van Vleck) $-\sum_{i < j} 2J_{ij} S_i S_j$, where S_i and S_j are resultant spin operators of ions *i* and *j*. Energy is the dimension of the exchange constant *J* which measures the extent of interaction between magnetic centers. A negative *J* couples adjacent spins anti-parallel (i.e. antiferromagnetic) while a positive *J* indicates parallel spin coupling (i.e. ferromagnetic). In a region where $|J/kT| \ll 1$ the solid behaves as a normal paramagnet, but when $|J/kT| \sim 1$ a cooperative change to an ordered state occurs. As $T \rightarrow 0$ K an antiferromagnet will adopt an ordered

Chapter 6 Magnetism

structure in which spins orientate anti-parallel and within the unit cell $\sum S_i = 0$. The behavior of χ vs. T for a typical antiferromagnet is shown in Figure 6.4.

In the $D_{\infty h}$ insertion compounds examined here sufficient numbers of U(V) could be linked together through diamagnetic oxide bridges U-O-U. In this situation the "superexchange" mechanism proposed by Kramers (24) and Anderson (25) involving the electrons and orbitals of the bridging oxygen provides a driving force towards antiferromagnetism that is particularly strong along a 180° U-O-U line (σ transfer). Along a chain of such a path it has been observed that $|J/k|$ has a r^{-n} dependence ($n \approx 12$) and exchange interactions decline rapidly with distance between metal ion centers (26). Irrespective of the actual mechanism determining the magnitude and sign of J , statistical mechanical models have been applied to account for the functional dependence of χ vs. T . One model uses the isotropic Heisenberg nearest-neighbors coupling scheme applied to a linear chain. This chooses as the appropriate Hamiltonian

$$H_{ex} = -2J_{ij} \sum_{i < j} (S_{iz}S_{jz} + S_{ix}S_{jx} + S_{iy}S_{jy}) \quad (6.37)$$

where summation is over nearest neighbors only. Even for this simple case no exact, closed form solution is obtainable. However, for antiferromagnetic interaction Bonner and Fisher (27) showed that for $S = 1/2$ ions the magnetic susceptibility passes through a maximum at a temperature defined by the expression

$$kT_{max}/|J| = 1.282 \quad (6.38)$$

with

$$\chi_{max}|J|/(Ng^2\mu_B) = 0.07346 \quad (6.39)$$

and

$$\mu_{eff} = \mu_B g[S(S+1)]^{1/2}. \quad (6.40)$$

For an assembly of $S = 1/2$ ions antiferromagnetically coupled in linear chains a numerical expression for χ as a function of $|J/kT|$ has been derived for the Heisenberg isotropic model (28)

$$\chi_{mol} = (Ng^2\mu_B^2/kT)(A+Bx+Cx^2)/(1+Dx+Ex^2+Fx^3)+(T.I.P.) \quad (6.41)$$

where $x = |J|/kT$ and A,B,C... are constants.

Magnetic susceptibility measurements of powder samples have been noted to be inadequate to unequivocally distinguish between this model and alternatives for magnetic ordering that appear in the literature (25). In the present case however, there is some advantage in using a simple model which provides a value for $\langle \chi \rangle$ since this is the only quantity which is measurable for a powder sample. Moreover, the required structural elements of one dimensional chains are easily recognized in the UO_{3-x} and U_3O_8 studied here. Although, this model ignores intralayer magnetic interactions, it does provide a means of estimating the expected behavior. For these reasons equation 6.41 is used to simulate the functional behavior of χ as a $f(T)$ in the ordering region ($kT \approx |J|$) leading to the estimation of $|J|$ and g as fitting parameters.

6.4 RESULTS

Molar magnetic susceptibility as a function of temperature at constant field strength (0.1 - 0.5 T was the range used for all compounds) for $\delta\text{-UO}_3$, $\text{UO}_{2.9}$, U_3O_8 , and their insertion compounds is plotted in Figures 6.8 to 6.10. The plots show χ_{mol} increases with insertion, keeping in mind that two electrons are transferred with magnesium and zinc, which coincides with the reduction of U(VI) to U(V). This behavior is seen more clearly in Figure 6.11 where χ_{mol} vs. x -value at 296 K is plotted for $\delta\text{-Li}_x\text{UO}_3$.

Predominantly paramagnetic behavior is exhibited by all but two compounds - $\delta\text{-UO}_3$ and $\text{Li}_{0.85}\text{U}_3\text{O}_8$. The small susceptibility of diamagnetic $\delta\text{-UO}_3$ in Figure 6.8 arises solely from temperature independent magnetism. The susceptibility of $\text{Li}_{0.85}\text{U}_3\text{O}_8$ shows a broad maximum near 36 K, which is generally indicative of the onset of long-range antiferromagnetic ordering. However, peculiar behavior is observed at lower temperatures as χ_{mol} actually increases below 21 K. χ_{mol} also displays a weak field dependence at 6 K (Figure 6.12).

Magnetism was also used qualitatively to verify the extent of electrochemical insertion into the uranium oxides. Figure 6.13 compares χ_{mol} vs. T of a mixture of 90 weight percent U_3O_8 and 10 weight percent graphite before and after the electrochemical insertion of magnesium to an x -value of 0.40. As with the chemically prepared insertion compounds,

Chapter 6 Magnetism

χ_{mol} becomes greater after insertion. The maximum in χ_{mol} at $T = 14 \text{ K}$ for $\text{Mg}_{0.40}\text{U}_3\text{O}_8$ suggests magnetic ordering is occurring.

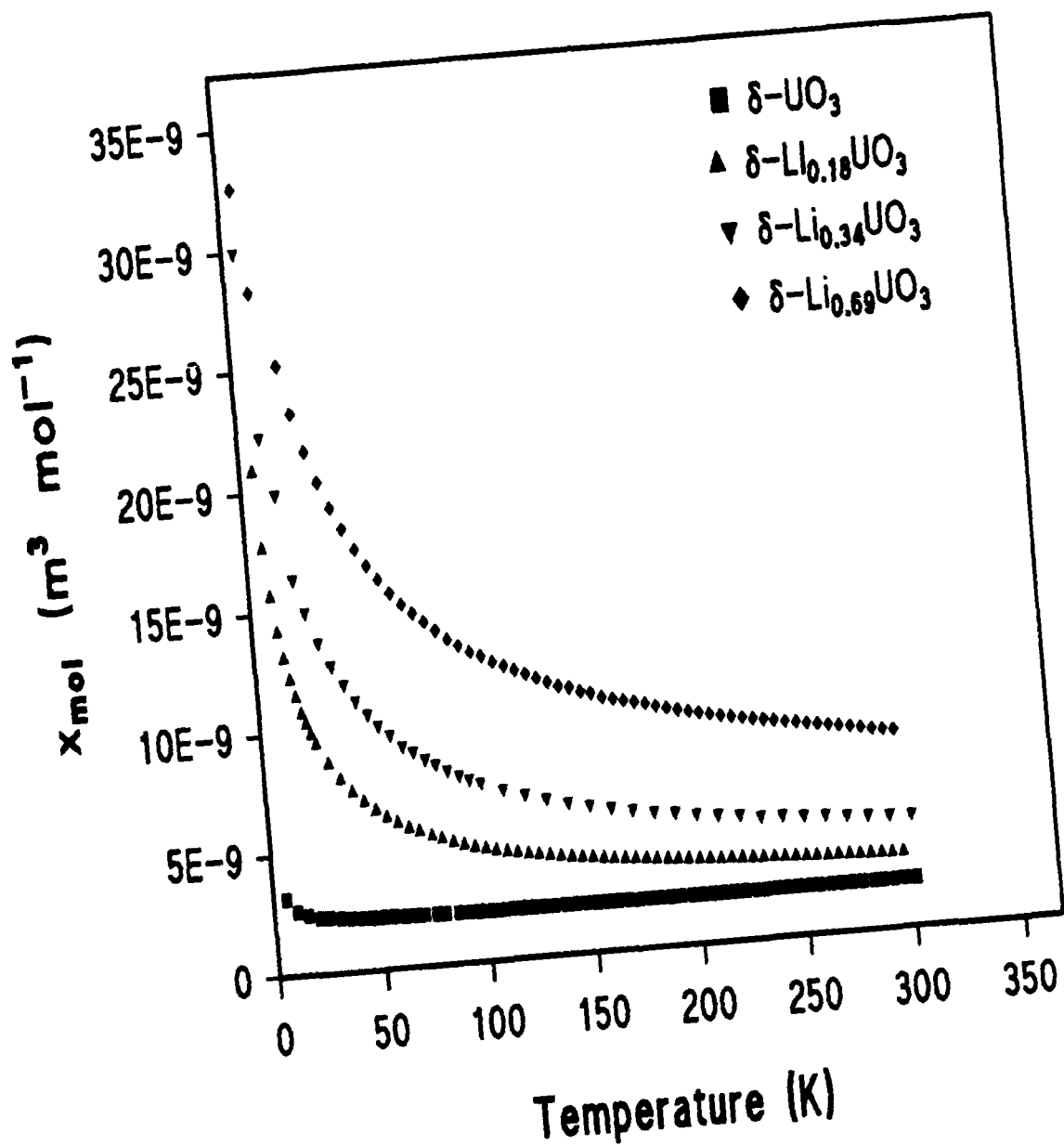
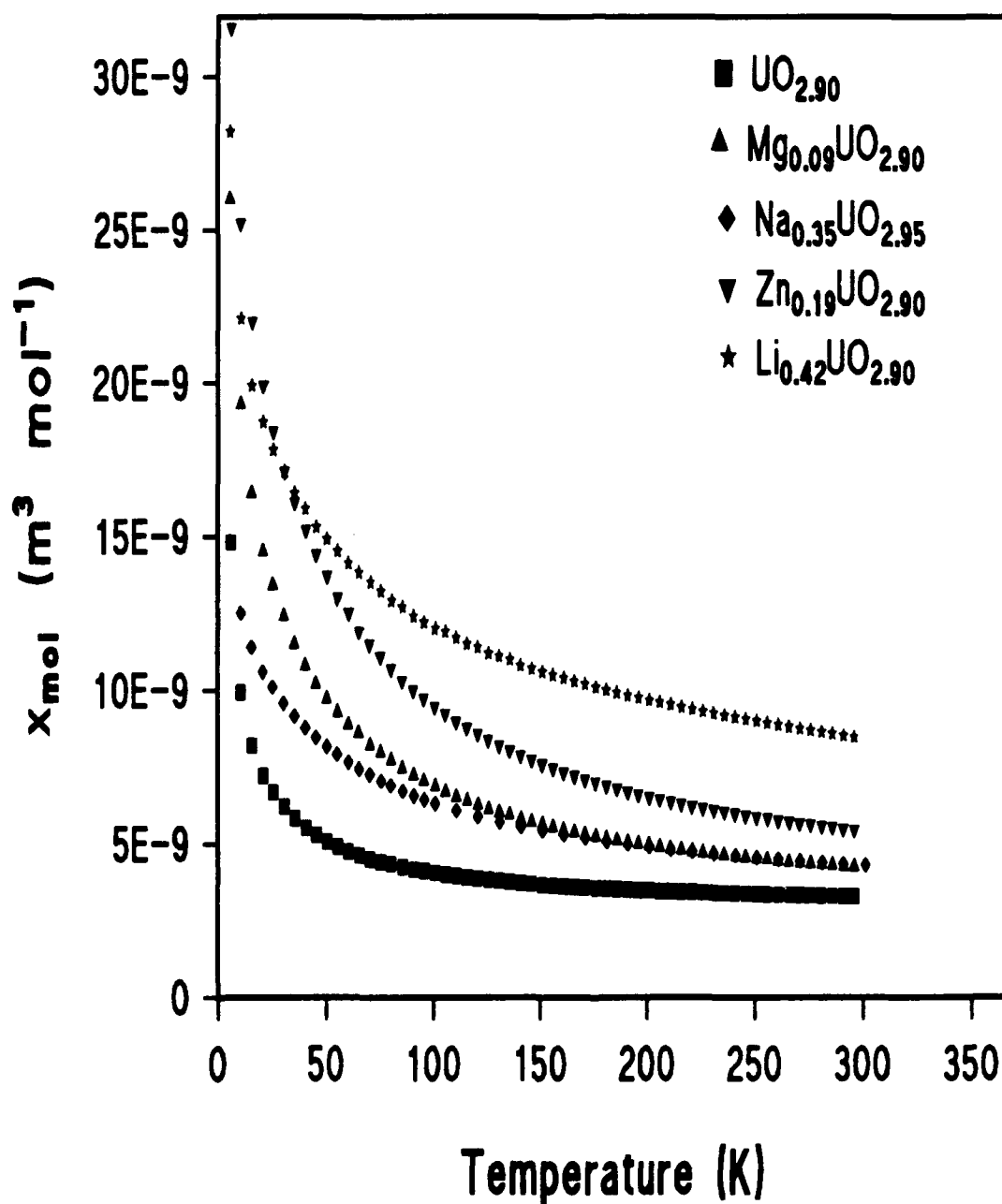
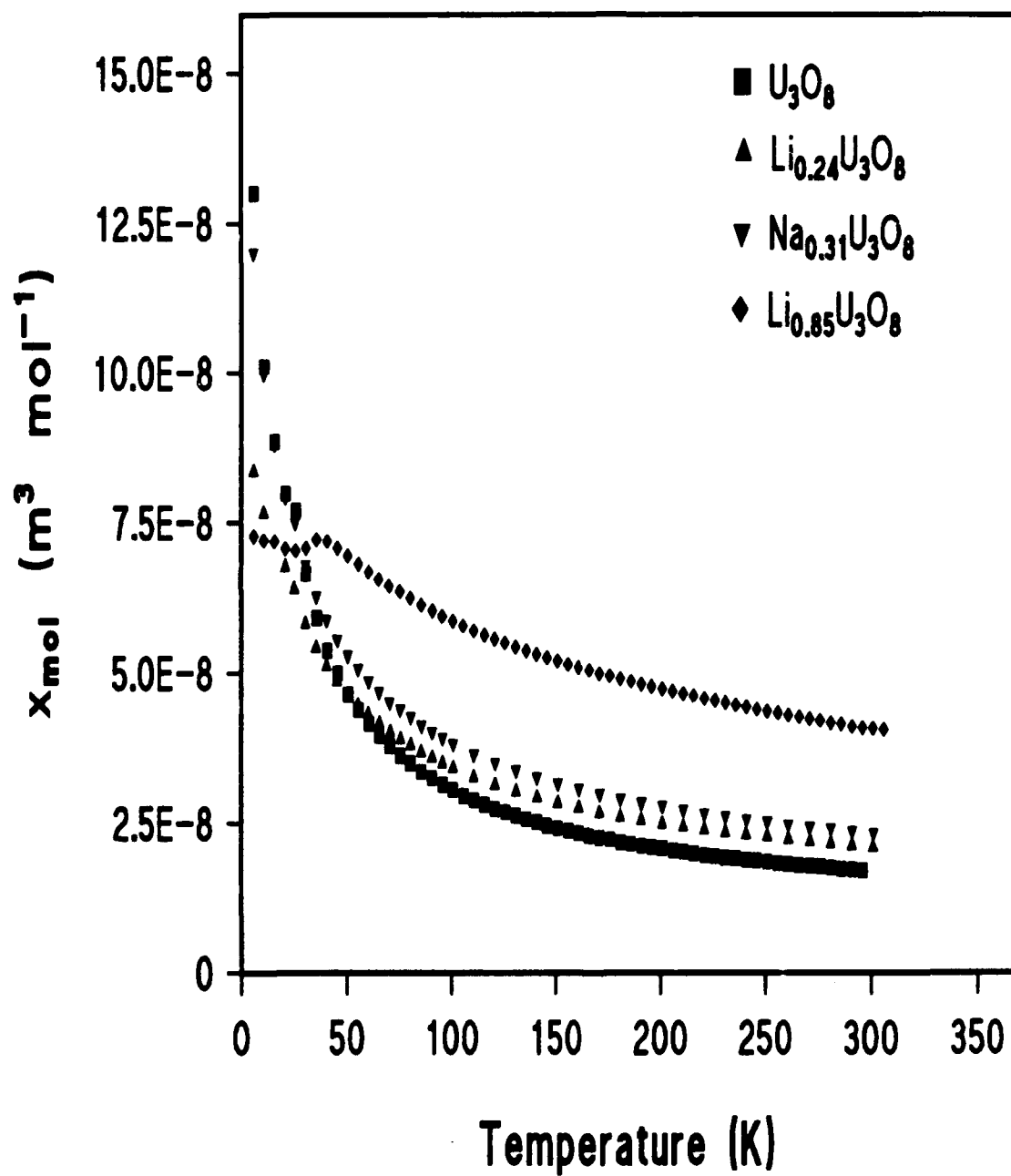
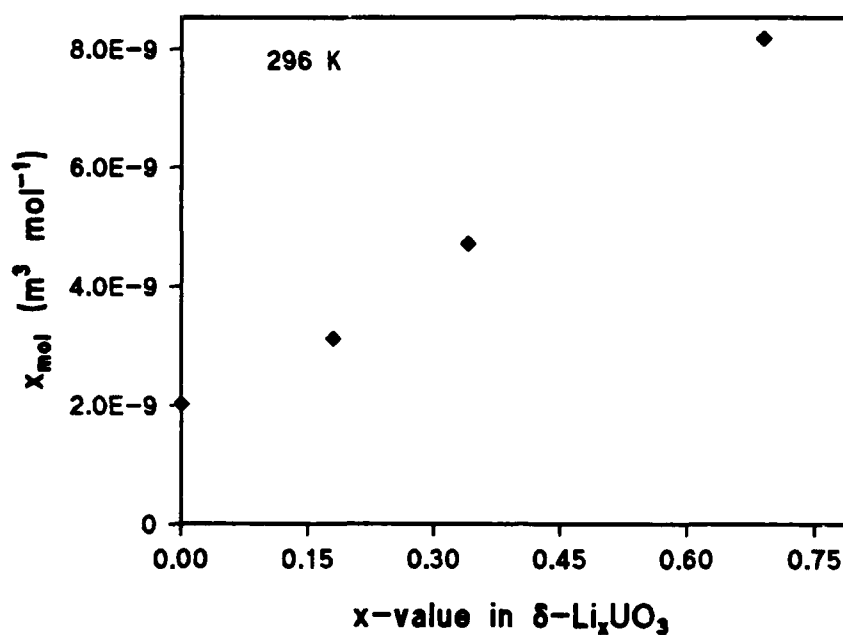
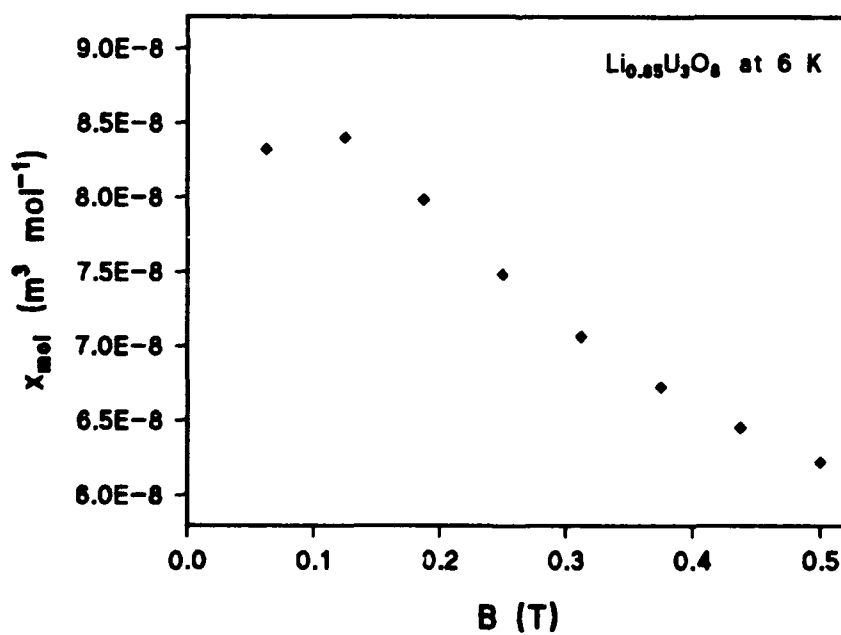


Figure 6.8 χ_{mol} vs. T for $\delta\text{-Li}_x\text{UO}_3$

Figure 6.9 χ_{mol} vs. T for $\text{M}_x\text{UO}_{2.9}$ ($\text{M}=\text{Li}, \text{Mg}, \text{Zn}, \text{Na}$)

Figure 6.10 χ_{mol} vs. T for $\text{M}_x\text{U}_3\text{O}_8$ ($\text{M}=\text{Li}, \text{Na}$)

Figure 6.11 χ_{mol} vs. x-value in $\delta\text{-Li}_x\text{UO}_3$ at 296 KFigure 6.12 χ_{mol} vs. B for $\text{Li}_{0.85}\text{U}_3\text{O}_8$ at 6 K

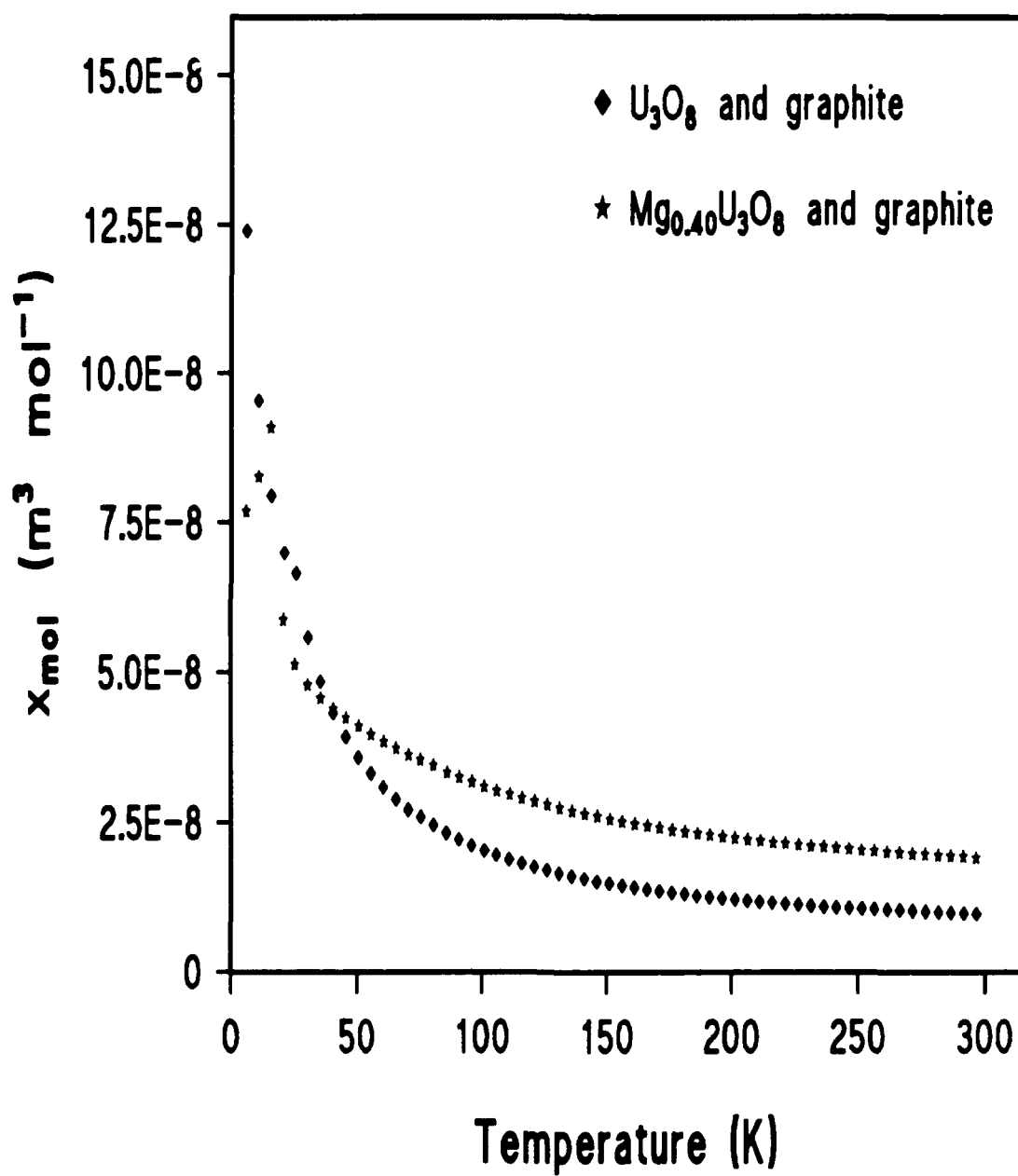


Figure 6.13 χ_{mol} vs. T for U_3O_8 +graphite and electrochemically prepared $\text{Mg}_{0.40}\text{U}_3\text{O}_8$ +graphite

Experimental data in the temperature range 150 - 296 K for assumed magnetically dilute compounds were fitted by the Langevin-Debye equation to yield parameters C^{exp} and A^{exp} (Table 6.1). Figures 6.14 to 6.17 show experimental values and the best fit for $(\chi_{\text{mol}} \text{ per } U(V))^{-1}$ vs. T. $\mu_{\text{eff}}^{\text{exp}}$ per $U(V)$ was calculated using the expression

$$\mu_{\text{eff}}^{\text{exp}} = [(3kC)/(N\mu_B^2)]^{1/2} \quad (6.42)$$

which is derived from the more common expression $\mu_{\text{eff}} = 2.83(\chi_{\text{mol}}T)^{1/2}$ by removing temperature independent paramagnetism. Calculations of Δ , Δ_2 , and A^{calc} , which are included in Table 6.1, are explained later in section 6.5.

Experimental data for $\text{Li}_{0.85}\text{U}_3\text{O}_8$ were fitted by the Langevin-Debye equation in the temperature range 150 - 296 K and by equation 6.41 in the temperature range 36 - 100 K with the results shown in Figure 6.18 and Table 6.1. Because it was not pure, no attempt was made to fit the results of electrochemically prepared $\text{Mg}_{0.40}\text{U}_3\text{O}_8$.

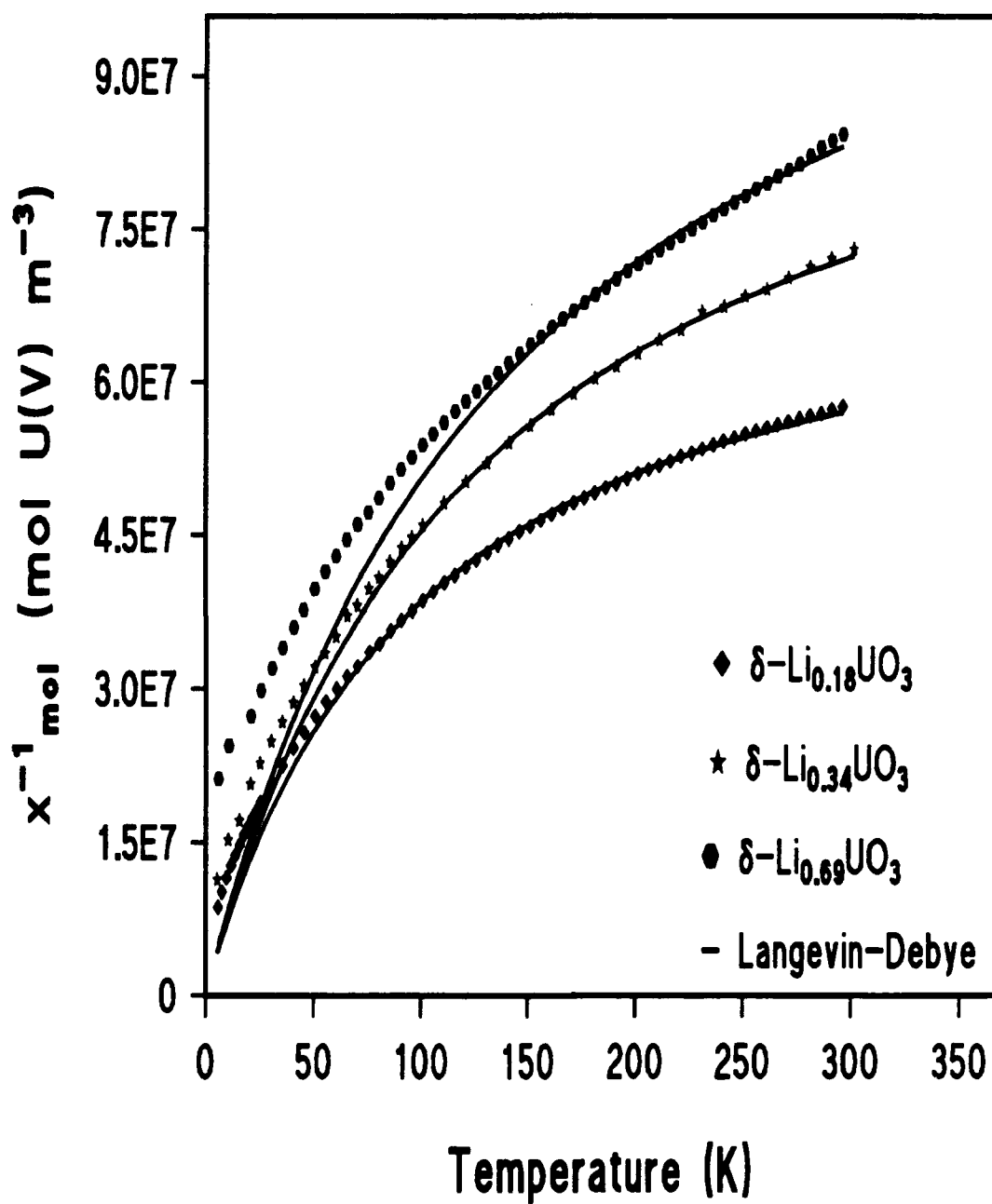
Table 6.1 Experimental and derived values for $U(V)$
octahedral crystal field

Compound	$C^{\text{exp}}/10^6$ $\text{m}^3 \text{ mol}^{-1} \text{ K}$	$A^{\text{exp}}/10^9$ $\text{m}^3 \text{ mol}^{-1}$	$A^{\text{calc}}/10^9$ $\text{m}^3 \text{ mol}^{-1}$	$\langle g^2 \rangle^{1/2}$	$\mu_{\text{eff}}^{\text{exp}}/\mu_B$	$\Delta (\text{cm}^{-1})$
$\delta\text{-UO}_3$		2.02				
$\delta\text{-Li}_{0.18}\text{UO}_3$	1.3	13.2	2.41	1.04	0.90	2,515
$\delta\text{-Li}_{0.34}\text{UO}_3$	1.2	9.72	2.40	1.02	0.89	2,609
$\delta\text{-Li}_{0.69}\text{UO}_3$	1.2	8.06	2.39	1.00	0.87	2,703
$^1\text{LiUO}_3$	0.63	4.57	3.27	0.73	0.63	3,974
$^1\text{NaUO}_3$	0.73	4.78	3.19	0.79	0.68	3,656
$^1\text{KUO}_3$	0.50	4.90	3.19	0.66	0.57	4,313

cylindrical crystal field

Compound	$C^{\text{exp}}/10^6$ $\text{m}^3 \text{ mol}^{-1} \text{ K}$	$A^{\text{exp}}/10^9$ $\text{m}^3 \text{ mol}^{-1}$	$A^{\text{calc}}/10^9$ $\text{m}^3 \text{ mol}^{-1}$	$\langle g^2 \rangle^{1/2}$	$\mu_{\text{eff}}^{\text{exp}}/\mu_B$	$\Delta_2 (\text{cm}^{-1})$	$1J/k \text{ K}$
$\text{UO}_{2.90}$	0.59	14.3	8.83	0.71	0.61	4,100	
$\text{Mg}_{0.09}\text{UO}_{2.90}$	1.1	7.38	8.51	0.98	0.85	10,000	
$\text{Zn}_{0.19}\text{UO}_{2.90}$	1.1	5.55	9.40	0.99	0.85	10,500	
$\text{Na}_{0.35}\text{UO}_{2.95}$	0.77	7.03	6.46	0.81	0.70	5,500	
$\text{Li}_{0.42}\text{UO}_{2.90}$	1.1	10.2	13.1	0.95	0.82	8,800	
U_3O_8	1.1	4.76	8.51	0.97	0.84	9,600	
$\text{Li}_{0.24}\text{U}_3\text{O}_8$	1.0	6.03	9.27	0.92	0.80	7,900	
$\text{Na}_{0.31}\text{U}_3\text{O}_8$	1.1	6.47	10.1	0.97	0.84	9,600	
$\text{Li}_{0.85}\text{U}_3\text{O}_8$	1.2	10.3	13.8	1.02	0.89	11,900	
$\text{Li}_{0.85}\text{U}_3\text{O}_8$		15.8		0.51			27.2
$^1\text{U}_3\text{O}_8$	1.3	4.52		1.06	0.92		

¹Reference 29

Figure 6.14 (χ_{mol} per U(V)) $^{-1}$ vs. T for $\delta\text{-Li}_x\text{UO}_3$

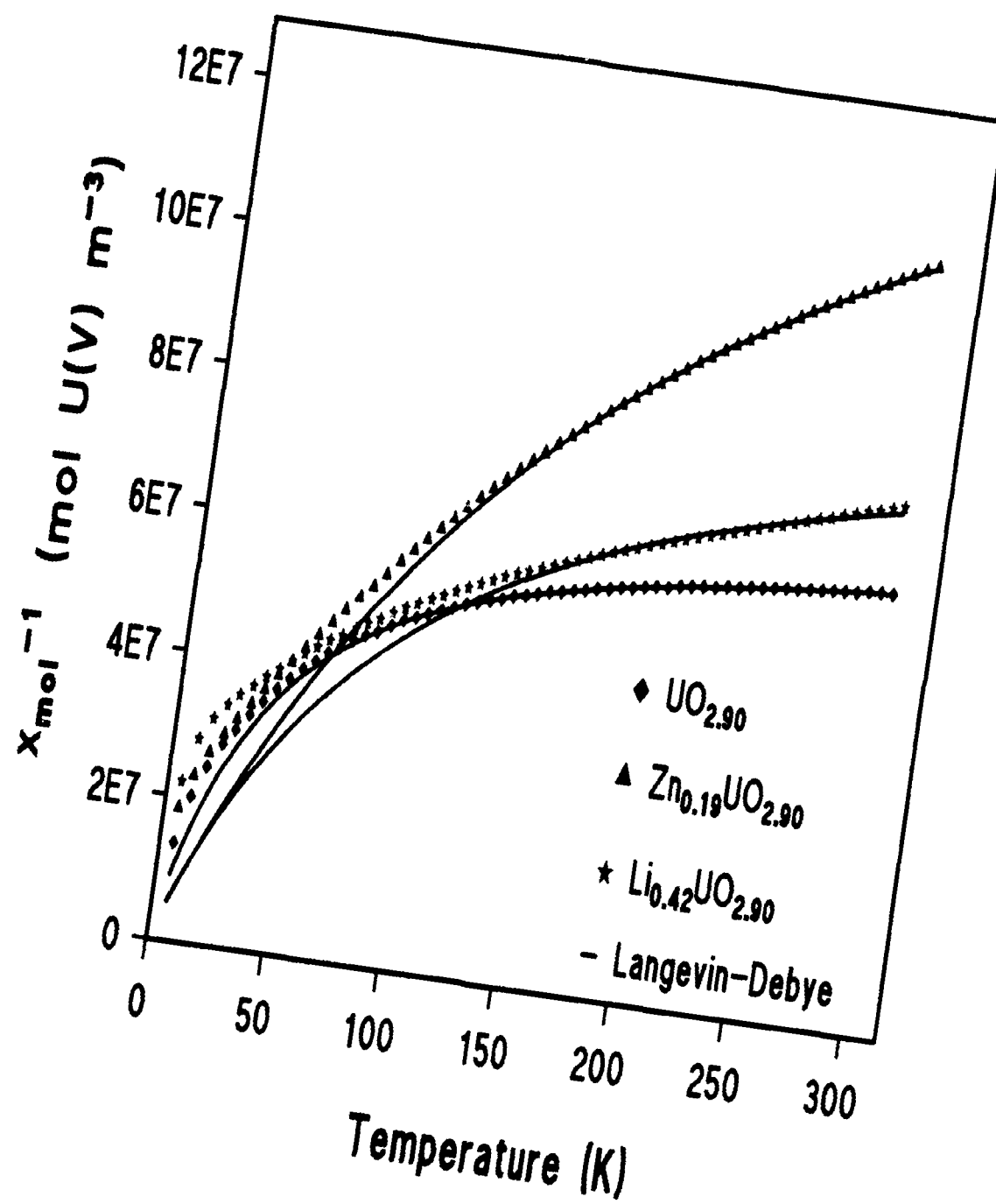


Figure 6.15 (χ_{mol} per U(V)) $^{-1}$ vs. T for $\text{M}_x\text{UO}_{2.9}$ (M=Zn, Li)

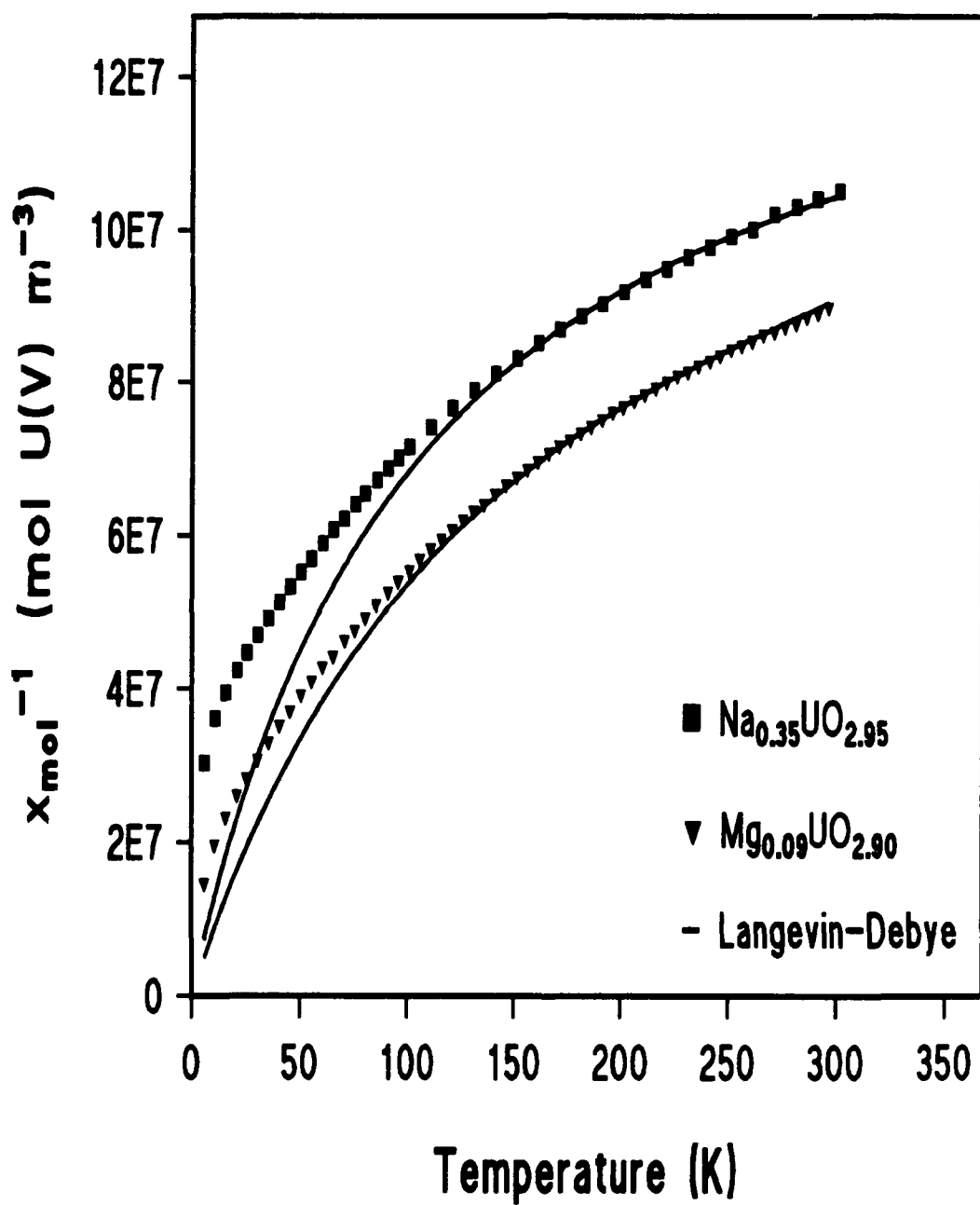


Figure 6.16 $(\chi_{\text{mol}} \text{ per U(V)})^{-1}$ vs. T for $\text{M}_x\text{UO}_{2.9}$ (M=Mg,Na)

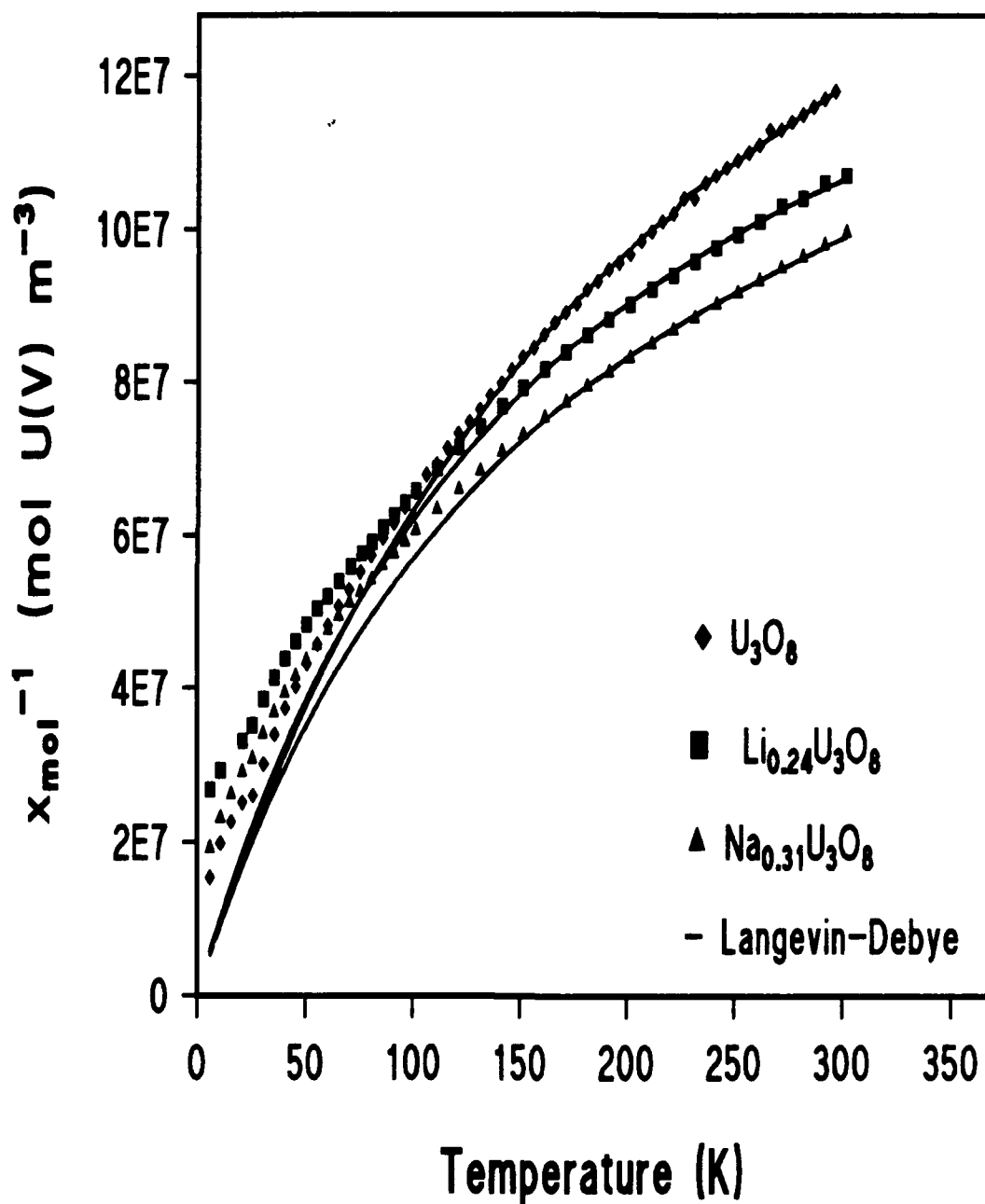


Figure 6.17 (χ_{mol} per U(V)^{-1}) vs. T for U_3O_8 and $\text{M}_x\text{U}_3\text{O}_8$ ($\text{M}=\text{Li}, \text{Na}$)

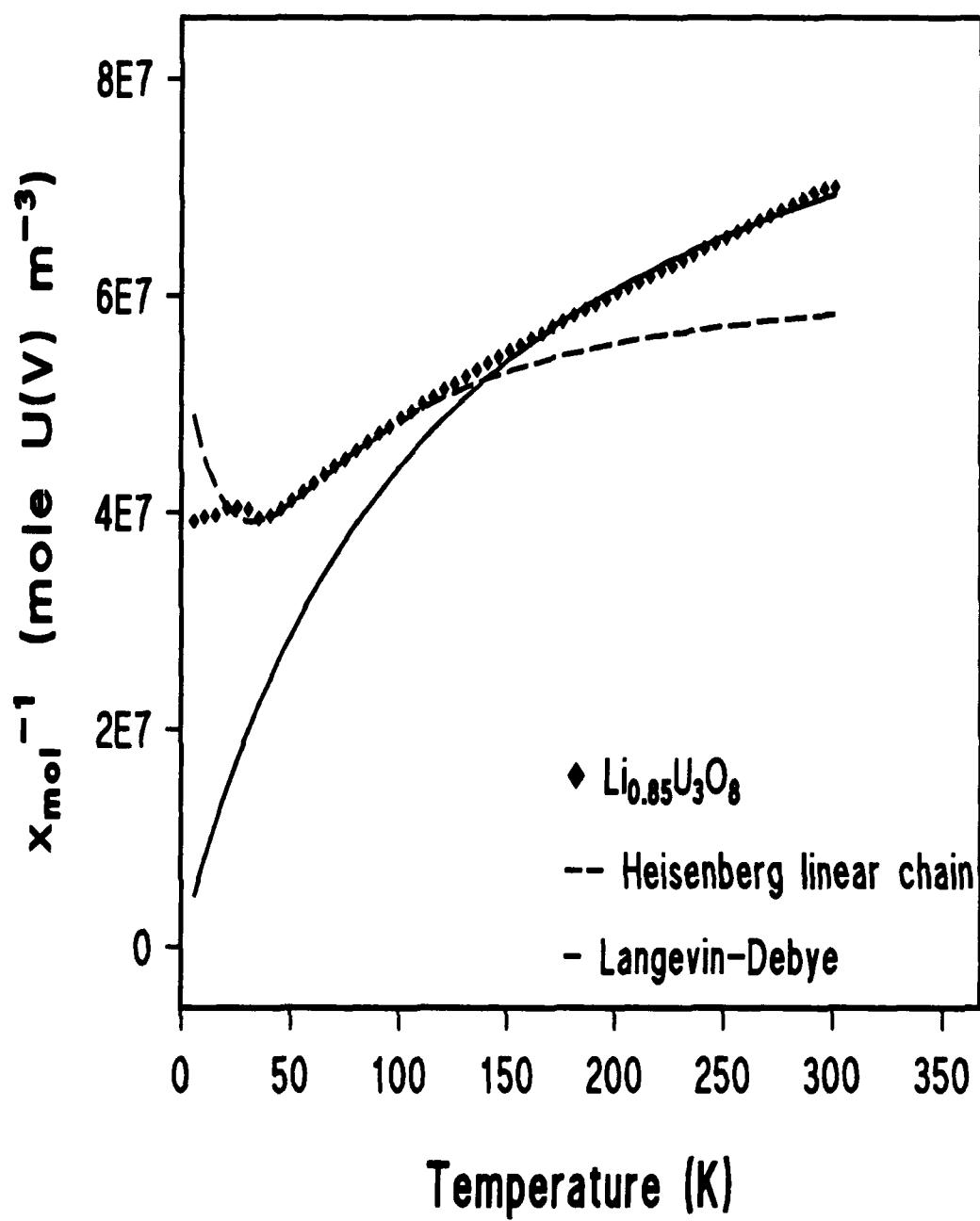


Figure 6.18 $(\chi_{\text{mol}} \text{ per U(V)})^{-1}$ vs. T for $\text{Li}_{0.85}\text{U}_3\text{O}_8$

6.5 DISCUSSION

A major aim of the work in this chapter was to detect changes in the electronic and magnetic properties of uranium oxides after insertion of metal ions. Figure 6.11 clearly shows χ_{mol} increases as a function of x-value. These results confirm that the formation of U(V) is a consequence of the insertion reaction



The success of magnetic susceptometry in this work and in others (14,30) at detecting this increase confirms it as a suitable diagnostic tool for analyzing electron transfer in insertion compounds.

The best fit of experimental data to the Langevin-Debye expression is at the higher temperatures where cooperative magnetic interactions are least significant. The deviations which occur between the two at lower temperatures are indicative of magnetic interaction between U(V) ions, with the size of the deviation increasing with the x-value. As U(V) concentration increases with insertion, the extent of the interaction between these paramagnetic centers becomes greater. Based upon the values for χ_{mol} being less than predicted by the Langevin-Debye equation at low temperatures, it appears the interactions are short-range and antiferromagnetic at small x-values. At high x-values (e.g. $\text{Li}_{0.85}\text{U}_3\text{O}_8$) the interactions between U(V) become long-range and the compound is antiferromagnetic below its Neel temperature.

Two models were selected, based upon the environment surrounding U(V), to predict the electronic and magnetic properties of the uranium oxides and their insertion compounds. The theoretical models previously discussed are well developed and have been shown to fit empirical data for other f^1 systems. It must be noted, however, that these models often have too many adjustable parameters to produce a unique solution. In order to fully utilize these models, the energies of the states shown in Figures 6.6 and 6.7 must be known.

Unfortunately, attempts to obtain these energies from spectral measurements in the near-IR and UV/VIS regions failed due to limitations of available instrumentation for measuring micro-crystalline powders. Without values for the energies, it was impossible to confirm independently the calculation of χ_{mol} using the van Vleck equation.

Nevertheless, some information pertaining to the electronic properties in both environments was still obtained using the models in conjunction with results from other f^1 systems (e.g. NpO_2^{2+} , NpF_6 , LiUO_3) in similar environments (13,16,29). Under the assumptions discussed in section 6.3, only the terms comprising the ground state contribute to μ_{eff} . It can be seen from Figures 6.6 and 6.7 that the composition of the ground state is determined by the crystal-field energy (Δ_2 or Δ) and the spin-orbit coupling constant (λ). Using equations 6.34 and 6.35 for O_h symmetry and those in Appendix C for $D_{\infty h}$ symmetry, Figures 6.19 and 6.20 show $\mu_{\text{eff}}^{\text{calc}}$ as a function of Δ_2 or Δ with the value of λ for U(V) taken from previous work to be $2,000 \text{ cm}^{-1}$ (29). With these models and the values for $\mu_{\text{eff}}^{\text{exp}}$ derived directly from C^{exp} , Δ_2 and Δ were calculated. These parameters were then used in equation 6.33 or in those listed in Appendix C to compute A^{calc} . The additional parameters for this calculation, $\theta = 4,000 \text{ cm}^{-1}$ and $\Delta_2 = 2,200 \text{ cm}^{-1}$, were taken from the literature for compounds structurally similar to those studied (14,23). All results are listed in Table 6.1.

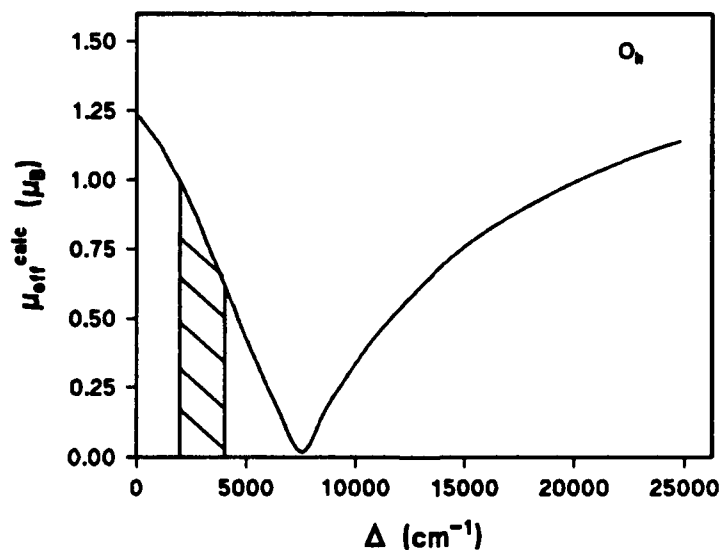


Figure 6.19 Calculated values for μ_{eff} as a function of Δ for f^1 in an octahedral field

Given the simplicity of the models, these values are in reasonable agreement with those obtained for structurally similar compounds also listed in Table 6.1. All values for Δ

either calculated or taken from the literature fall within the shaded region in Figure 6.19.

The tendency of the octahedral model to underestimate A (T.I.P.) was also found by

Kanellakopulos et al. (23) using similar expressions. The proximity of λ to Δ_2 and Δ

indicates both spin-orbit coupling and ligand field effects are significant, which account for $\mu_{\text{eff}}^{\text{exp}}$ being significantly lower than the free ion ($2.54 \mu_B$) and spin only ($1.73 \mu_B$) values.

The other plausible explanations, namely the effect of lowering the symmetry surrounding U(V) and the introduction of covalency into the bonding, cannot be addressed in this simple model (7).

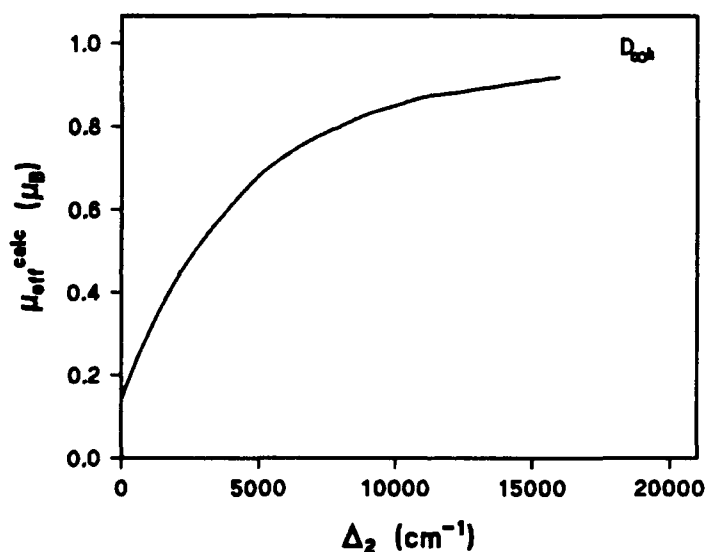


Figure 6.20 Calculated values for μ_{eff} as a function of Δ for f^1 in an axial field

Evidence for long-range magnetic ordering was observed in only two compounds; $\text{Li}_{0.85}\text{U}_3\text{O}_8$ and $\text{Mg}_{0.40}\text{U}_3\text{O}_8$. Since both compounds have a high concentration of U(V), cooperative magnetic interaction is feasible, especially along the interlayer U(V)-O-U(V) chains. The low, broad maximum in χ_{mol} for $\text{Li}_{0.85}\text{U}_3\text{O}_8$ is characteristic of one-dimensional magnetic systems (31). However, the upturn in χ_{mol} below 21 K is not explicable using this model and is thought to be caused by trace impurities. The presence of impurities could also account for the sharp spike in χ_{mol} for $\text{Mg}_{0.40}\text{U}_3\text{O}_8$. Reports of long-range ordering occurring

Chapter 6 Magnetism

in the U(V) compounds LiUO_3 , NaUO_3 , and KUO_3 have been made (23,32,33), although the published data are conflicting.

REFERENCES

1. J. Crangle, Solid State Magnetism, Edward Arnold, London, (1991).
2. D. Jiles, Introduction to Magnetism and Magnetic Materials, Chapman and Hall, London, (1991).
3. G. Pass and H. Sutcliffe, *J. Chem. Ed.*, **48**, 3, 180, (1971).
4. S. J. Swithenby, *Contemp. Phys.*, **15**, 3, 249, (1974).
5. B. D. Josephson, *Phys. Lett.*, **1**, 251, (1962).
6. C. J. O'Connor, in Progress in Inorganic Chemistry Vol. 29, (S. J. Lippard ed.), John Wiley and Sons, New York, (1982).
7. F. E. Mabbs and D. J. Machin, Magnetism and Transition Metal Complexes, Chapman and Hall, London, (1973).
8. J. H. Van Vleck, The Theory of Electric and Magnetic Susceptibilities, Oxford University Press, London, (1932).
9. C. J. Ballhausen, Introduction to Ligand Field Theory, McGraw-Hill, London, (1962).
10. R. G. Denning, *Structure and Bonding*, **79**, 215, (1992).
11. J. C. Eisenstein and M. H. L. Pryce, *Proc. Roy. Soc.*, **A229**, 20, (1955).
12. J. C. Eisenstein and M. H. L. Pryce, *Proc. Roy. Soc.*, **A238**, 31, (1956).
13. J. C. Eisenstein and M. H. L. Pryce, *J. Res. NBS-A. Phys. and Chem.*, **69A**, 3, 217, (1965).
14. S. Patat, D.Phil. Thesis, Oxford, (1992).
15. A. M. Chippindale, P. G. Dickens, and A. V. Powell, *Prog. Sol. State Chem.*, **21**, 3, 133, (1991).
16. J. C. Eisenstein and M. H. L. Pryce, *Proc. Roy. Soc.*, **A255**, 181, (1960).
17. C. J. Ballhausen, *Theor. Chim. Acta*, **24**, 234, (1972).
18. H. G. Hecht, W. B. Lewis, and M. P. Eastman, *Adv. Chem. Phys.*, **21**, 351, (1971).
19. N. Edelstein, *Rev. Chim. Miner.*, **14**, 149, (1977).
20. J. Selbin, C. J. Ballhausen, and D. G. Durrett, *Inorg. Chem.*, **11**, 510, (1972).
21. J. S. Griffith and L. E. Orgel, *J. Chem. Phys.*, **26**, 5, 988, (1957).
22. P. W. Atkins, M. S. Child, and C. S. G. Phillips, Tables for Group Theory, Oxford University Press, New York, (1990).
23. B. Kanellakopoulos, E. Henrich, C. Keller, F. Baumgartner, E. Konig, and V. P. Desai, *Chem. Phys.*, **53**, 197, (1980).
24. H. A. Kramers, *Physica*, **1**, 182, (1934).

Chapter 6 Magnetism

25. P. W. Anderson, *Phys. Rev.*, **79**, 350, (1950).
26. R. L. Carlin, *Magnetochemistry*, Springer-Verlag, Berlin, (1986).
27. J. C. Bonner and M. E. Fisher, *Phys. Rev. A*, **135**, 640, (1964).
28. W. E. Hatfield, in *Solid State Chemistry Techniques*, (A. K. Cheatham and P. Day eds.), Clarendon Press, Oxford, (1987).
29. S. Kemmler-Sack, E. Stumpp, W. Rudorff, and H. Erfurth, *Z. Anorg. Allg. Chem.*, **354**, 287, (1967).
30. M. J. Woodall, Part II Thesis, Oxford, (1992).
31. J. C. Bonner, *J. Appl. Phys.*, **49**, 1299, (1978).
32. C. Miyake, K. Fujino, and S. Imoto, *Chem. Phys. Lett.*, **46**, 349, (1977).
33. C. Miyake, K. Fujino, and S. Imoto, *Chem. Phys. Lett.*, **61**, 124, (1979).

CHAPTER 7 CONCLUSIONS

The purpose of this chapter is to provide a brief summary of the main conclusions of this work grouped into the following themes: structural, thermodynamics, kinetics, and magnetism. Following the summary, suggestions for further work are given.

7.1 STRUCTURAL

Insertion of sodium, magnesium, and zinc by chemical and electrochemical methods was shown to achieve lower x -values than those previously attained for lithium. These lower x -values are attributed to the greater electronegativity of these elements, their larger ionic radii, and their higher charge when compared to lithium. Cell parameters showed only small changes upon insertion with a decrease in the crystallinity of the parent metal oxide. The greatest loss of the host's crystal structure occurred when sodium was inserted into δ - UO_3 and UTiO_5 . Loss of crystallinity was thought to be partially responsible for the irreversible behavior exhibited by cells during charging.

7.2 THERMODYNAMICS

The integral Gibbs free energy of insertion (ΔG_x) for sodium, magnesium, and zinc into $\text{UO}_{2.9}$, U_3O_8 , and UTiO_5 were calculated using equilibrium cell potentials. Results compiled in Figures 4.18 to 4.20 showing the close agreement between ΔG_x and ΔH_x verifies the correct behavior of the new cell designs developed during the course of this work. The large $-\Delta G_x$ values for magnesium are a reflection of the two-electron transfer accompanying its insertion. The $-\Delta G_x$ values for sodium were found to be comparable to those measured for lithium insertion into the same uranium oxides. Zinc's relatively low values for $-\Delta G_x$ are due to it being the most electronegative of the guest metals examined.

7.3 KINETICS

The diffusivity in the solid-state of sodium, magnesium, and zinc was found to be three-to-four orders of magnitude lower than that previously reported for lithium in the uranium oxides. These results confirm previous theoretical calculations which cited the large size of sodium and the divalency of magnesium (and zinc) as the reasons for their low

Chapter 7 Conclusions

mobilities. Such low mobilities could also have contributed to the irreversible behavior exhibited by cells during charge.

Cyclic voltammetric studies of uranium oxides mechanically transferred to a carbon electrode support a mechanism for insertion whereby electron transfer is coupled with solid-state diffusion. These two processes were separable in electrolytes containing magnesium, but not so in lithium and sodium electrolytes at scan rates ≤ 500 mV/s. Such differences in behavior are consistent with the diffusion of magnesium being slower than the more mobile alkali-metals.

7.4 MAGNETISM

The magnetic susceptibilities of $\text{UO}_{2.9}$, U_3O_8 , and $\delta\text{-UO}_3$ and their insertion compounds were measured over the temperature range 6 - 300 K using a SQUID susceptometer. The data were fitted by the Langevin-Debye equation which yielded parameters used in the calculation of the magnetic moment and crystal-field splitting energy. The results for U(V) in both O_h (i.e. $\delta\text{-UO}_3$) and $\text{D}_{\infty h}$ (U_3O_8 and $\text{UO}_{2.9}$) symmetries indicate electrons are transferred to the uranium 5f-orbitals to form an $2F$ state. At high x-values in $\text{Li}_x\text{U}_3\text{O}_8$, evidence for antiferromagnetic ordering was observed at temperatures below 36 K.

7.5 SUGGESTIONS FOR FURTHER WORK

An overwhelming majority of work pertaining to electrochemical insertion has been performed at room-temperature. The electrochemical systems developed during this work would enable the maximum temperature for studying insertion to be increased to 200°C. Operating at higher temperatures would improve the kinetics of some systems that are too slow for study at room-temperature.

Additional work is needed to confirm the ordering of energy levels within U(V) compounds with $\text{D}_{\infty h}$ symmetry. Recommended techniques for obtaining this information are ESR and diffuse-reflectance spectroscopy using powder samples.

Detailed studies of the magnetic behavior of compounds with high U(V) concentrations at low temperatures are also recommended.

APPENDIX

APPENDIX A X-RAY DIFFRACTION PATTERNS

Appendix A.1 X-Ray Diffraction Pattern for γ - UO_3

2θ	d (obs)	d (calc)	I	h k l
13.546	6.531	6.517	16	1 1 0
17.750	4.993	4.984	32	0 4 0
20.250	4.382	4.375	59	1 2 1
25.795	3.451	3.452	100	1 5 0
27.348	3.258	3.258	72	2 2 0
29.291	3.046	3.046	52	2 1 1
31.980	2.796	2.796	76	2 3 1
32.561	2.748	2.744	17	1 6 1
34.033	2.632	2.632	16	1 7 0
37.571	2.392	2.392	6	2 6 0
41.257	2.186	2.188	17	2 4 2
42.433	2.128	2.130	16	3 2 1
42.830	2.110	2.092	15	2 7 1
44.798	2.021	2.020	20	2 8 0
45.520	1.991	1.991	20	3 5 0
47.790	1.902	1.902	12	3 1 2
49.558	1.838	1.837	23	3 3 2
52.137	1.753	1.753	12	1 11 0
52.395	1.745	1.741	22	2 8 2
53.089	1.724	1.724	27	4 0 0
56.443	1.629	1.629	8	4 4 0
59.994	1.541	1.541	18	4 0 2
68.389	1.371	1.372	9	2 12 2

Orthorhombic

a = 6.896(5) b = 19.934(17) c = 6.877(20)

Appendix A.2 X-Ray Diffraction Pattern for $\gamma\text{-Li}_{0.81}\text{UO}_3$

2θ	d (obs)	d (calc)	I	h k l
13.409	6.598	6.526	21	1 1 0
17.730	4.998	4.964	18	0 4 0
20.240	4.384	4.391	63	1 2 1
25.862	3.442	3.443	100	1 5 0
27.091	3.289	3.263	70	2 2 0
29.250	3.051	3.056	68	2 1 1
31.955	2.798	2.802	70	2 3 1
32.675	2.738	2.742	21	1 6 1
34.145	2.624	2.624	11	1 7 0
41.273	2.185	2.196	21	2 4 2
42.304	2.135	2.135	12	3 2 1
47.741	1.903	1.910	22	3 1 2
49.081	1.855	1.843	31	3 3 2
52.459	1.743	1.743	21	2 8 2
53.006	1.726	1.727	25	4 0 0
56.350	1.631	1.631	9	4 4 0

Orthorhombic

a = 6.910(8) b = 19.856(69) c = 6.938(35)

Appendix A.3 X-Ray Diffraction Pattern for $\gamma\text{-Mg}_{0.05}\text{UO}_3$

2θ	d (obs)	d (calc)	I	h k l
13.516	6.546	6.512	9	1 1 0
17.768	4.988	4.973	26	0 4 0
20.256	4.380	4.372	42	1 2 1
25.812	3.449	3.446	100	1 5 0
27.347	3.258	3.256	50	2 2 0
29.278	3.048	3.044	41	2 1 1
31.959	2.798	2.794	58	2 3 1
33.979	2.636	2.627	19	1 7 0
37.531	2.394	2.389	85	2 6 0
41.223	2.188	2.186	17	2 4 2
42.382	2.131	2.128	13	3 2 1
42.866	2.108	2.089	13	2 7 1
45.546	1.990	1.989	21	3 5 0
49.585	1.837	1.835	24	3 3 2
52.475	1.742	1.731	25	2 8 2
53.162	1.721	1.723	27	4 0 0
60.062	1.539	1.540	16	4 0 2
68.528	1.368	1.370	16	2 12 2

Orthorhombic

a = 6.892(9) b = 19.892(32) c = 6.875(34)

Appendix A.4 X-Ray Diffraction Pattern for $\gamma\text{-Zn}_{0.04}\text{UO}_3$

2θ	d (obs)	d (calc)	I	h k l
13.571	6.519	6.517	11	1 1 0
17.770	4.987	4.982	29	0 4 0
20.266	4.378	4.381	48	1 2 1
25.801	3.450	3.451	100	1 5 0
27.354	3.258	3.258	56	2 2 0
29.302	3.045	3.048	33	2 1 1
31.964	2.797	2.798	60	2 3 1
32.594	2.745	2.746	11	1 6 1
33.993	2.635	2.632	13	1 7 0
37.521	2.395	2.392	4	2 6 0
41.150	2.192	2.191	13	2 4 2
42.428	2.129	2.130	11	3 2 1
45.513	1.991	1.991	13	3 5 0
49.542	1.838	1.838	16	3 3 2
52.535	1.740	1.743	20	2 8 2
53.111	1.723	1.724	21	4 0 0
59.887	1.543	1.542	13	4 0 2
68.250	1.373	1.373	8	2 12 2

Orthorhombic

$$a = 6.896(2) \quad b = 19.929(9) \quad c = 6.902(10)$$

Appendix A.5 X-Ray Diffraction Pattern for $\delta\text{-UO}_3$

2θ	d (obs)	d (calc)	I	h k l
21.434	4.142	4.146	100	1 0 0
30.545	2.924	2.932	61	1 1 0
37.901	2.372	2.394	14	1 1 1
43.599	2.074	2.073	24	2 0 0
48.851	1.863	1.854	32	2 1 0
54.222	1.690	1.693	23	2 1 1

Cubic

$$a = 4.146(7)$$

Appendix A.6 X-Ray Diffraction Pattern for $\delta\text{-Li}_{0.69}\text{UO}_3$

2θ	d (obs)	d (calc)	I	h k l
22.299	3.983	4.110	100	1 0 0
30.476	2.931	2.906	29	1 1 0
49.562	1.838	1.838	13	2 1 0

Cubic

$$a = 4.110(14)$$

Appendix A.7 X-Ray Diffraction Pattern for $\delta\text{-Mg}_{0.03}\text{UO}_3$

2θ	d (obs)	d (calc)	I	h k l
21.380	4.152	4.154	100	1 0 0
30.365	2.941	2.937	69	1 1 0
43.484	2.079	2.077	33	2 0 0
49.134	1.853	1.858	49	2 1 0
53.963	1.698	1.698	37	2 1 1

Cubic $a = 4.154(4)$ Appendix A.8 X-Ray Diffraction Pattern for $\delta\text{-Zn}_{0.02}\text{UO}_3$

2θ	d (obs)	d (calc)	I	h k l
21.316	4.165	4.131	100	1 0 0
30.369	2.941	2.921	45	1 1 0
43.718	2.069	2.067	18	2 0 0
49.362	1.845	1.848	27	2 1 0

Cubic $a = 4.131(6)$ Appendix A.9 X-Ray Diffraction Pattern for $\text{UO}_{2.90}$

2θ	d (obs)	d (calc)	I	h k l
21.315	4.165	4.171	76	0 0 1
25.956	3.430	3.433	100	1 0 0
33.813	2.649	2.651	57	1 0 1
43.432	2.082	2.086	14	0 0 2
45.772	1.981	1.982	16	1 1 0
51.089	1.786	1.782	23	1 0 2
53.142	1.722	1.717	8	2 0 0
58.213	1.583	1.587	8	2 0 1

Hexagonal

 $a = 3.964(5)$ $b = 3.964(5)$ $c = 4.172(9)$ Appendix A.10 X-Ray Diffraction Pattern for $\text{Mg}_{0.07}\text{UO}_{2.90}$

2θ	d (obs)	d (calc)	I	h k l
21.333	4.161	4.163	77	0 0 1
25.992	3.425	3.451	100	1 0 0
33.850	2.646	2.657	60	1 0 1
43.469	2.080	2.081	14	0 0 2
45.831	1.978	1.993	12	1 1 0
51.176	1.783	1.782	23	1 0 2
52.803	1.732	1.726	2	2 0 0

Hexagonal

 $a = 3.985(9)$ $b = 3.985(9)$ $c = 4.163(13)$

Appendix A.11 X-Ray Diffraction Pattern for $\text{Zn}_{0.19}\text{UO}_{2.90}$

2θ	d (obs)	d (calc)	I	h k l
21.333	4.161	4.170	100	0 0 1
26.353	3.379	3.369	99	1 0 0
34.090	2.628	2.620	70	1 0 1
43.507	2.078	2.085	16	0 0 2
46.560	1.949	1.945	19	1 1 0
51.386	1.777	1.773	33	1 0 2
51.992	1.757	1.763	21	1 1 1
65.575	1.422	1.422	14	1 1 2

Hexagonal

a = 3.890(6) b = 3.890(6) c = 4.170(8)

Appendix A.12 X-Ray Diffraction Pattern for $\text{Li}_{0.42}\text{UO}_{2.90}$

2θ	d (obs)	d (calc)	I	h k l
21.232	4.181	4.169	80	0 0 1
25.966	3.428	3.423	100	1 0 0
33.839	2.647	2.646	61	1 0 1
43.265	2.089	2.084	16	0 0 2
45.788	1.980	1.977	16	1 1 0
51.111	1.786	1.780	34	1 0 2
53.513	1.711	1.712	5	2 0 0

Hexagonal

a = 3.953(7) b = 3.953(7) c = 4.169(8)

Appendix A.13 X-Ray Diffraction Pattern for $\text{Na}_{0.35}\text{UO}_{2.95}$

2θ	d (obs)	d (calc)	I	h k l
21.348	4.159	4.160	100	0 0 1
26.110	3.410	3.419	85	1 0 0
33.915	2.641	2.641	54	1 0 1
43.356	2.085	2.080	17	0 0 2
46.332	1.958	1.974	9	1 1 0
51.454	1.774	1.777	24	1 0 2
53.307	1.717	1.710	6	2 0 0

Hexagonal

$$a = 3.948(11) \quad b = 3.948(11) \quad c = 4.160(15)$$

Second phase

20.885	4.250	4.234	100	0 0 1
25.227	3.527	3.473	44	1 0 0
33.571	2.667	2.685	90	1 0 1
42.646	2.118	2.117	16	0 0 2

Hexagonal

$$a = 4.010(38) \quad b = 4.010(38) \quad c = 4.233(17)$$

Appendix A.14 X-Ray Diffraction Pattern for $\alpha\text{-U}_3\text{O}_8$

2θ	d (obs)	d (calc)	I	h k l
21.411	4.146	4.138	92	0 0 1
25.953	3.430	3.425	100	1 3 0
26.498	3.361	3.355	48	2 0 0
33.890	2.643	2.639	74	1 3 1
34.307	2.612	2.606	36	2 0 1
45.477	1.993	1.992	11	0 6 0
46.492	1.952	1.950	27	3 3 0
50.799	1.796	1.795	15	0 6 1
51.535	1.772	1.771	40	1 3 2
51.746	1.765	1.761	47	2 0 2
53.431	1.713	1.713	15	2 6 0
54.712	1.676	1.677	9	4 0 0
58.256	1.582	1.582	18	2 6 1
59.394	1.555	1.555	9	4 0 1
64.992	1.434	1.434	14	0 6 2
65.778	1.418	1.418	18	3 3 2
67.893	1.379	1.379	5	0 0 3

Orthorhombic

$$a = 6.710(3) \quad b = 11.950(6) \quad c = 4.138(2)$$

Appendix A.15 X-Ray Diffraction Pattern for $\alpha\text{-Li}_{0.85}\text{U}_3\text{O}_8$

2θ	d (obs)	d (calc)	I	h k l
21.226	4.182	4.193	98	0 0 1
25.790	3.452	3.441	52	1 3 0
26.164	3.403	3.394	100	2 0 0
33.610	2.664	2.660	41	1 3 1
33.929	2.640	2.638	89	2 0 1
43.211	2.092	2.097	20	0 0 2
45.702	1.983	1.996	25	0 6 0
46.450	1.953	1.968	12	3 3 0
50.922	1.792	1.790	37	1 3 2
51.199	1.783	1.784	48	2 0 2
53.062	1.724	1.720	4	2 6 0
53.901	1.700	1.697	11	4 0 0
57.770	1.595	1.592	11	2 6 1
66.875	1.398	1.398	4	0 0 3

Orthorhombic

 $a = 6.788(14)$ $b = 11.974(23)$ $c = 4.193(5)$ Appendix A.16 X-Ray Diffraction Pattern for $\alpha\text{-Na}_{0.31}\text{U}_3\text{O}_8$

2θ	d (obs)	d (calc)	I	h k l
21.412	4.146	4.150	100	0 0 1
25.982	3.426	3.430	98	1 3 0
26.512	3.359	3.360	29	2 0 0
33.909	2.641	2.644	64	1 3 1
34.343	2.609	2.611	22	2 0 1
43.615	2.073	2.075	18	0 0 2
45.493	1.992	1.994	6	0 6 0
46.463	1.953	1.953	11	3 3 0
50.776	1.797	1.797	10	0 6 1
51.435	1.775	1.775	30	1 3 2
51.705	1.766	1.765	30	2 0 2
53.362	1.715	1.715	6	2 6 0
54.590	1.680	1.680	2	4 0 0
58.111	1.586	1.585	5	2 6 1
59.297	1.557	1.557	3	4 0 1

Orthorhombic

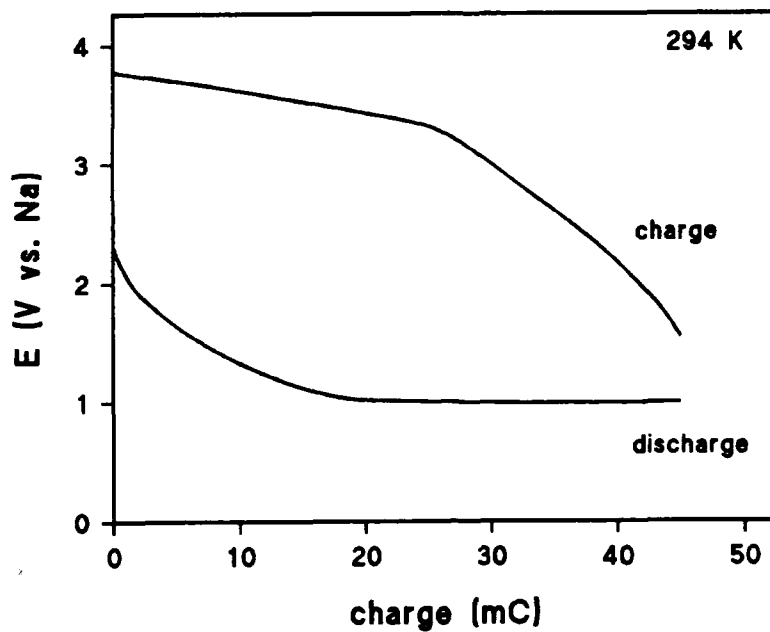
 $a = 6.720(2)$ $b = 11.965(4)$ $c = 4.150(2)$

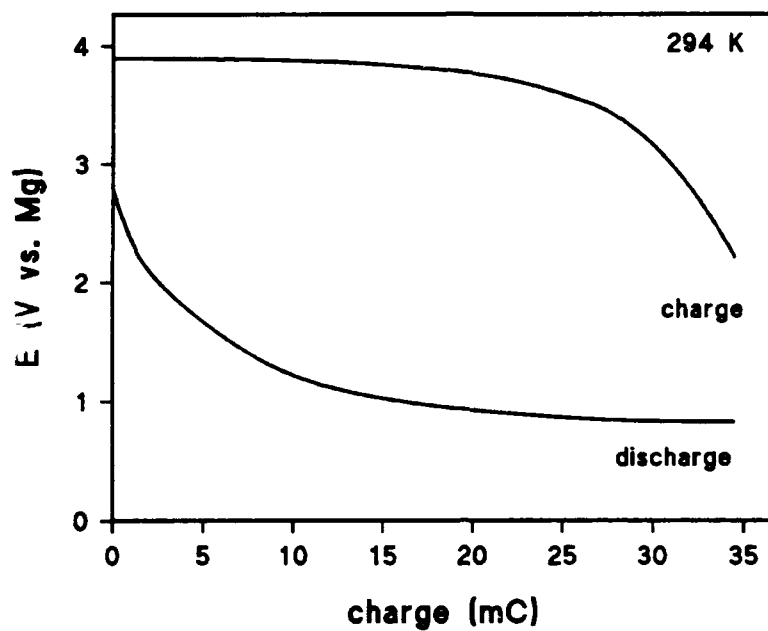
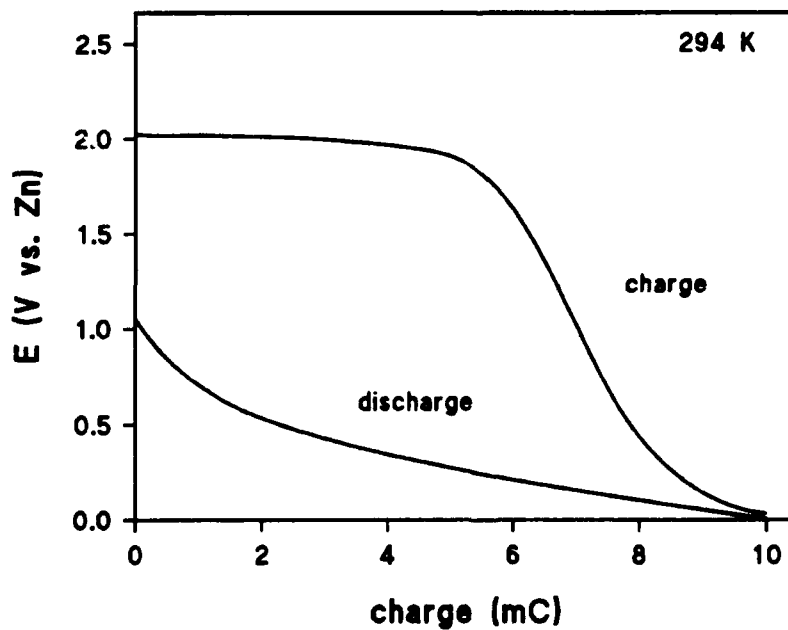
Appendix A.17 X-Ray Diffraction Pattern for UTiO_5

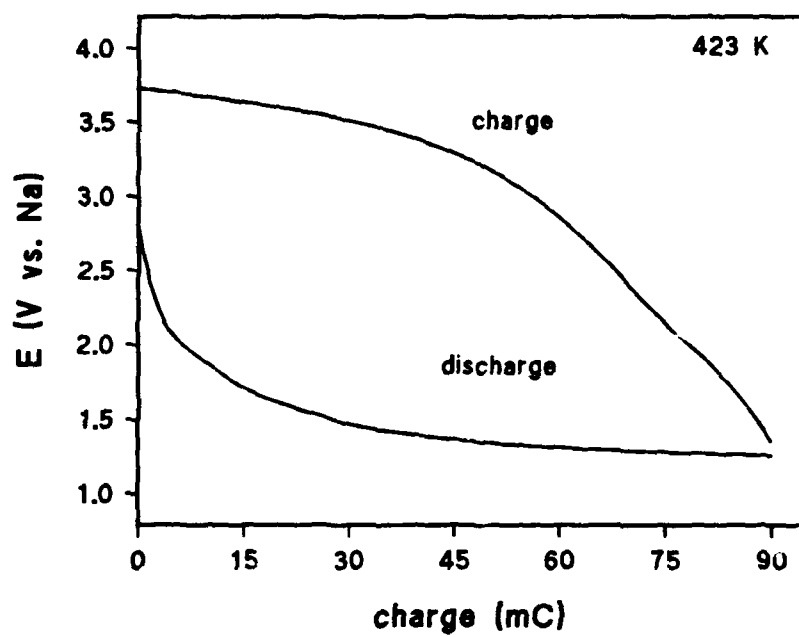
2θ	d (obs)	d (calc)	I	h k l
18.003	4.923	4.931	72	1 0 2
22.627	3.926	3.907	47	0 0 4
26.609	3.347	3.351	29	0 1 4
27.927	3.192	3.186	100	1 2 0
36.274	2.474	2.469	51	1 2 4
36.495	2.460	2.465	47	2 0 4
39.280	2.292	2.291	18	2 2 2
46.398	1.955	1.953	6	0 0 8
49.311	1.846	1.847	16	0 4 0
51.690	1.767	1.768	5	1 4 0
55.097	1.665	1.665	29	0 4 4
57.739	1.595	1.595	9	1 4 4
62.924	1.476	1.475	15	2 4 4

Orthorhombic

 $a = 6.356(17)$ $b = 7.364(10)$ $c = 15.628(32)$

APPENDIX B ELECTROCHEMICAL WINDOWS OF ELECTROLYTES**Appendix B.1 0.4 M NaClO₄ in Propylene Carbonate on Graphite at 25 μ A**

Appendix B.2 0.5 M $\text{Mg}(\text{ClO}_4)_2$ in DMF on Graphite at 25 μA Appendix B.3 0.2 M Zinc Triflate in Propylene Carbonate/DMSO on Graphite at 25 μA 

Appendix B.4 0.1 M NaClO_4 in DMSO_2 on Graphite at $25\ \mu\text{A}$ 

APPENDIX C WAVEFUNCTIONS FOR f^1 IN A CYLINDRICAL FIELD

Appendix C.1 Wavefunctions for f^1 After Perturbation by a Cylindrical Field

$$\begin{aligned} \phi_1 &= |-2, 1/2\rangle & \phi_2 &= |2, -1/2\rangle & \phi_3 &= |-3, 1/2\rangle & \phi_4 &= |3, -1/2\rangle & \phi_5 &= |-2, -1/2\rangle & \phi_6 &= |2, 1/2\rangle \\ \phi_7 &= |-3, -1/2\rangle & \phi_8 &= |3, 1/2\rangle & \phi_9 &= |-1, 1/2\rangle & \phi_{10} &= |1, -1/2\rangle & \phi_{11} &= |-1, -1/2\rangle & \phi_{12} &= |1, 1/2\rangle \\ \phi_{13} &= |0, -1/2\rangle & \phi_{14} &= |0, 1/2\rangle \end{aligned}$$

Appendix C.2 Wavefunctions and Their Energies for f^1 After Perturbation by a Cylindrical Field and Spin-Orbit Coupling

State	Wavefunction	Energy
$\Delta_{3/2u}$	$\Psi_1 = (1+b^2)^{-1/2}(\phi_1 + b'\phi_{11})$ $\Psi_2 = (1+b^2)^{-1/2}(\phi_2 + b'\phi_{12})$	$\lambda(-1+(5/2)^{1/2}b')$
$\Phi_{5/2u}$	$\Psi_3 = (1+a^2)^{-1/2}(\phi_5 - a'\phi_3)$ $\Psi_4 = (1+a^2)^{-1/2}(\phi_6 - a'\phi_4)$	$\lambda(1-(3/2)^{1/2}a')$
$\Delta_{5/2u}$	$\Psi_5 = (1+a^2)^{-1/2}(\phi_5 - a'\phi_3)$ $\Psi_6 = (1+a^2)^{-1/2}(\phi_6 - a'\phi_4)$	$\lambda(1-(3/2)^{1/2}a')$
$\Phi_{7/2u}$	$\Psi_7 = \phi_7$ $\Psi_8 = \phi_8$	$\lambda(x+3/2)$
$\Pi_{1/2u}$	$\Psi_9 = (1+c^2)^{-1/2}(\phi_9 - c'\phi_{13})$ $\Psi_{10} = (1+c^2)^{-1/2}(\phi_{10} - c'\phi_{14})$	$\lambda(y-(3)^{1/2}c'-1/2)$
$\Pi_{3/2u}$	$\Psi_{11} = (1+b^2)^{-1/2}(\phi_1 + b'\phi_{11})$ $\Psi_{12} = (1+b^2)^{-1/2}(\phi_2 + b'\phi_{12})$	$\lambda(-1+(5/2)^{1/2}b')$
$\Sigma_{1/2u}$	$\Psi_{13} = (1+c^2)^{-1/2}(\phi_9 - c'\phi_{13})$ $\Psi_{14} = (1+c^2)^{-1/2}(\phi_{10} - c'\phi_{14})$	$\lambda(y-(3)^{1/2}c'-1/2)$

$$x = \Delta_1/\lambda \quad y = \Delta_2/\lambda \quad z = \Delta_3/\lambda \quad a' = -1/a \quad b' = -1/b \quad c' = -1/c$$

$$a = [-x+2.5+(x^2-5x+12.25)^{1/2}]/(6)^{1/2} \quad b = [y+1.5+(y^2+3y+12.25)^{1/2}]/(10)^{1/2}$$

$$c = [y-z-0.5+(y^2+z^2-2yz+z-y+12.25)^{1/2}]/(12)^{1/2}$$

Appendix C.3 First- and Second-Order Zeeman Coefficients in the z-Direction

Energy	$W_z^{(1)}/\mu_B$	$W_z^{(2)}/\mu_B$
E_1, E_2	$\pm(2b'^2+1)/(b'^2+1)$	$-[(2.5)^{1/2}\lambda(1+b^2)(1+b'^2)(b-b')^{-1}]^{-1}$
E_3, E_4	$\pm(2a^2+3)/(a^2+1)$	$-[(1.5)^{1/2}\lambda(1+a^2)(1+a'^2)(a-a')^{-1}]^{-1}$
E_5, E_6	$\pm(2a'^2+3)/(a'^2+1)$	$[(1.5)^{1/2}\lambda(1+a^2)(1+a'^2)(a-a')^{-1}]^{-1}$
E_7, E_8	± 4	0
E_9, E_{10}	$\pm c^2/(c^2+1)$	$-[(3)^{1/2}\lambda(1+c^2)(1+c'^2)(c-c')^{-1}]^{-1}$
E_{11}, E_{12}	$\pm(2b^2+1)/(b^2+1)$	$[(2.5)^{1/2}\lambda(1+b^2)(1+b'^2)(b-b')^{-1}]^{-1}$
E_{13}, E_{14}	$\pm c'^2/(c'^2+1)$	$[(3)^{1/2}\lambda(1+c^2)(1+c'^2)(c-c')^{-1}]^{-1}$
